© Copyright 2021

Elizabeth R. Canarie

Fundamentals and Applications of Biological EPR Spectroscopy

Elizabeth R. Canarie

A dissertation
submitted in partial fulfillment of the
requirements for the degree of

Doctor of Philosophy

University of Washington

2021

Reading Committee:

Stefan Stoll, Chair

Sarah Keller

Joshua Vaughan

Jesse Zalatan

Program Authorized to Offer Degree:

Chemistry

University of Washington

Abstract

Fundamentals and Applications of Biological EPR Spectroscopy

Elizabeth R. Canarie

Chair of the Supervisory Committee:
Associate Professor Stefan Stoll
Chemistry

This thesis details robust experimental investigations of sample conditions for EPR spectroscopy. This work investigates two areas of sample conditions. First, a robust experimental investigation of the effect of sample matrix deuteration on relaxation behavior is presented. This work serves to guide experimental practitioners to choose optimal sample conditions for EPR measurement. Second, an investigation of the effects of different spin labels on intra-protein distance measurements in double electron electron resonance (DEER) spectroscopy is detailed. The distance distribution $P(r)$ obtained via DEER includes the flexibility of the spin label in addition to the flexibility of the protein. This work provides a direct comparison of commonly used spin labels in DEER experiments on the same site pairs to isolate spin label effects on distribution broadening.

TABLE OF CONTENTS

ACKNOWLEDGMENTS

None of the work presented in this thesis would have been possible without my incredible support network. Getting a PhD can be an incredibly isolating experience, and it is uniquely to finish the degree during a global pandemic, but I never felt too alone thanks to a wonderful community.

First, thank you to Professor Stefan Stoll for always pushing me to do and to be my best. I consider myself truly lucky to have been able to spend the past five years being his mentee. The lessons he has taught me go far beyond magnetic resonance and I know that I am a better person for having worked with him. I hope I can one day be as good of a mentor as Stefan is.

Thank you to my parents, Pam and Dave, and my siblings: Joe, Anthony, Jeremy, and Regina, for a lifetime of support. I am so blessed by their enthusiastic attempts to understand my science, for all the pep talks they've given me, all the practice talks they've listened to, and paper editing that they have done for me. None of my academic success would have been possible without their tireless love and support.

I am very thankful to my committee: Professor Sarah Keller, Professor Munira Khalil, Professor Josh Vaughan, Professor Jesse Zalatan, and Professor Ning Zheng, for their insights and guidance along the way. I am also thankful to Ning for his mentorship during my time in the molecular biophysics training grant program and while working with his incredible postdoc Dr. Hui Wang to discover a previously unseen FeS cluster (**Chapter 4**). That has been my favorite project during my time in grad school.

I owe so much to the entire Stoll Patrol for being the best group I could have ever asked for. Dr. Ellen Hayes' mentorship helped me navigate my PhD, and her friendship has helped me get through it. Thank you to Dr. Eric Evans for helping me put out so many fires along the way. I was nearly ready to give up on the work in **Chapter 3** until Dr. Maxx Tessmer joined the Stoll Patrol and helped me get over the hurdles I was having with mutagenesis and protein purification. I also must thank my former undergraduate student, Elizabeth Sather, for her enthusiasm and dedication on a project that was in a rut. Sarah Sweger has become my sister. To the rest of the Stoll Patrol, past and present, Dr. Thomas Edwards, Dr. Donald Mannikko, Dr. Jeremy Lenher, Dr. Claudia Tait, Dr. Stephan Pribitzer, Sam Jahn, Shutian Lu, Rachelle Stowell, Luis Fábregas Ibáñez, Jörg Fischer, and Dr. Maria Giulia Dal Farra, you have all been the best groupmates I could have ever asked for.

I am so thankful to all of my friends, but I want to highlight a few people. Sarah Pristash and Chantelle Leveille have been my rocks since day one of grad school and Ashley Dostie's love has brightened so many days. Dr. Rachel Gebhart was my magnet–mountain woman. Magnetic resonance is a niche field, and having someone I could hike and discuss the latest magnet failure with was a delight. Mike Mouhanna was an incredible roommate for the first three years of my PhD.

The Department of Chemistry is run by an incredible staff, who are truly dedicated to running and improving the UW Chemistry Department and without whom we would all be lost. Particularly, I owe the success of many experiments to Dr. Adrienne Roehrich for sharing many liters of liquid helium with me. Diana Knight's thoughtfulness, kindness, and support over the past five years has made my experience at UW markedly better. Also, thank you to Loch Hickok, a fellow basement dweller, for his unrelenting humor, the many doughnuts he gave me, and for removing that metal splinter from my finger.

Thank you to Big Time Brewery and to Bean and Bagel for supplying the carbs necessary

to fuel my science.

I would be remiss to not thank my undergraduate mentors, Professor Jim Allen and Dr. Tien Le Olson for giving me the rare opportunity to do EPR as an undergraduate. That experience led me to Stefan's group and taught me that I could be an interdisciplinary researcher. Also from my time at Arizona State, I need to thank Professor George Wolf. His dedication, kindness, and enthusiasm for his undergraduate quantum class is why I pursued a PhD in physical chemistry.

And finally, I owe the world to Nicholas Davis. He has been by my side through three chemistry degrees and all the life that happened during them. He has made me a better scientific communicator and a more patient human. His impressive knowledge of EPR experiments and instrumentation demonstrates how much he has supported me. Nothing I can write will ever be enough to say how thankful I am for his partnership. So instead, I'll just promise him that I'm done with school.

DEDICATION

In memory of my grandmothers, Kathryn and Grace.

Chapter 1

EPR APPLICATIONS IN STRUCTURAL BIOLOGY

1.1 EPR Overview

Electron paramagnetic resonance (EPR) spectroscopy is a useful technique for the study of a variety of chemical and biological systems, which has been gaining popularity in recent years. Biological applications of EPR include redox state monitoring, structural determination, local environment coordination, amongst many other applications. While similar in principle to nuclear magnetic resonance (NMR) spectroscopy, EPR is not as commonly taught in undergraduate chemistry programs as NMR is. Given that EPR is sensitive only to paramagnetic species, it often fills a gap left by other biophysical techniques. The recent advent of affordable benchtop EPR spectrometers is making this technique accessible to those who have not traditionally had the opportunity to perform EPR spectroscopy.

As EPR is selective only to paramagnetic systems—that is, systems with unpaired electron spins—it can fill unique gaps in research on hugely complicated systems. Particularly, EPR applications in structural biophysics can illuminate a significant amount of information about a system. Fortunately, the advent of benchtop EPR spectrometers has made the technique more accessible for a wider variety of practitioners, with applications ranging from protein structure determination, local coordination of metallic centers in inorganic compounds, electrochemical studies, radiation dosimetry, food shelf stability, and non-destructive study of ancient artifacts like mummies.[1]

The goal of this chapter is to provide those new to EPR with a location to look up succinct

definitions of the vocabulary accompanying EPR spectroscopy and a thorough amalgamation of important literature to understand the topics discussed in depth. The following sections will outline the basic principles of paramagnetism, fundamental interactions experienced by paramagnetic centers, EPR instrumentation, and some basics of dipolar EPR spectroscopy (pulse EPR).

1.2 Fundamental EPR Vocabulary and the Spin Hamiltonian

The goal of this section is to provide accessible, robust definitions of common EPR vocabulary. It would be a discredit to the reader to not mention the many wonderfully thorough textbooks on EPR spectroscopy, such as Schweiger-Jeschke,[2] Weil-Bolton,[3] Eaton-Eaton,[4] and Goldfarb-Stoll.[5] Additionally, the EPR primer by Chechik, Carter, and Murphy is well-suited for magnetic resonance novices.[6]

To understand what systems are possible to probe with EPR, we must begin with a discussion of what paramagnetism is. The presence (or generation) of paramagnetic species is a necessary precondition for any EPR experiment.

1.2.1 Basics of paramagnetism

The work in this thesis focuses on paramagnetic systems. Generally, paramagnetic systems are ones in which the system weakly interacts with an external magnetic field, as well as local magnetic fields within the system itself—that is, EPR probes systems with unpaired electron spins.

Paramagnetism arises from the electron's angular momentum (**Figure 1.1**). The spin of a charged particle (electron) generates a current, and this current gives rise to a magnetic moment, defined by:

$$\boldsymbol{\mu} = -\mu_{\mathrm{B}} g_{\mathrm{e}} \boldsymbol{S} \tag{1.1}$$

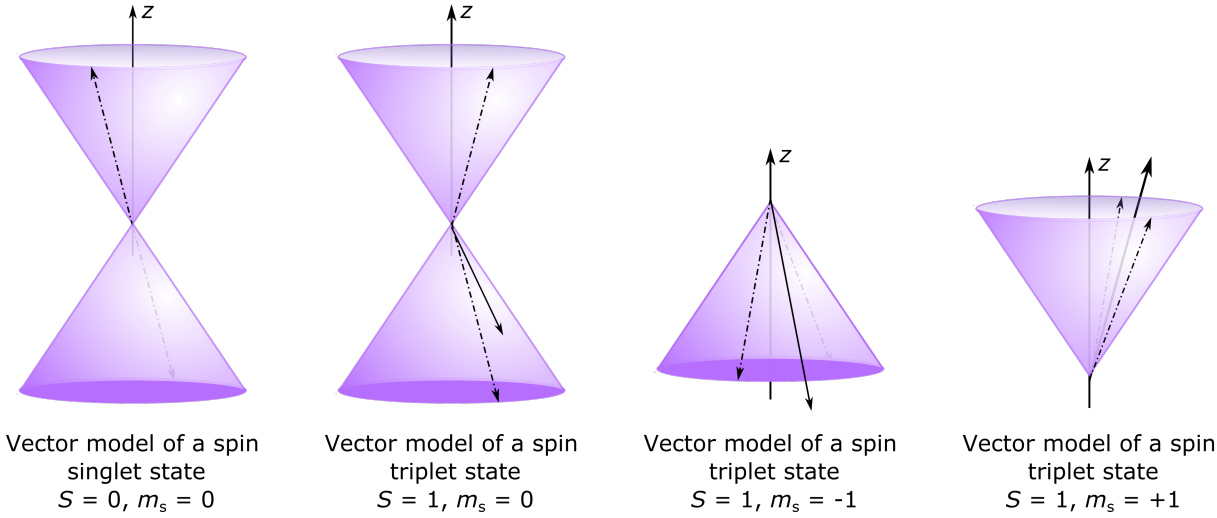

Figure 1.1: A vector representation of angular momentum. The left panel shows a spin singlet $S = 0$. Since the spin angular momentum vectors cancel (dashed lines), there is no net angular momentum. The other three panels show two electron spins giving different spin triplet states $S = 1$. The total angular momentum is shown in solid black.

where μ_B is the Bohr magneton, g_e is the g-value of a free election and $\boldsymbol{s}$ is the spin angular momentum. In **Figure 1.1**, the magnetic moment of the spin state is shown in a solid black line. In the case of an even number of electrons, it is common for the spin magnetic moment of the system (shown as a solid black line in the figure) to be canceled out by an antiparallel magnetic moment. This is shown with of the spin singlet state in **Figure 1.1** where the magnetic moments of the two electrons are shown as dashed lines—that is to say, there is no net magnetic moment due to the cancellation of angular momentum. In this case, the system is called diamagnetic. In the case when the total magnetic moment is not canceled out (as in the case of the spin triplet state shown in **Figure 1.1**), the system is called paramagnetic.

There are a plethora of systems that contain paramagnetic centers.[7] Some systems of particular signifance in EPR are metalloproteins or metalloenzymes, proton-coupled electron transport, and even within the foods we eat. Commonly paramagnetic systems can be probed

with electrochemistry,[8] magnetic circular dichorism spectroscopy,[9] SQUID magnetometry,[10] Mössbauer spectroscopy,[11] and electron paramagnetic resonance (EPR) spectroscopy. EPR spectroscopy is a highly useful and versatile technique for probing paramagnetic systems as it is insensitive to any non-magnetic interactions.[4,6]

A discussion of Zeeman splitting is central to the general concept of any EPR experiment (**Figure 1.2**).[4,12] Perhaps the most fundamental EPR experiment is the continuous-wave (CW) experiment. In the absence of an external magnetic field (assuming no zero-field splitting), α and β electrons are degenerate. The convention of α and β in this chapter is spin up and spin down, that is $m_S = +1/2$ and $m_S = -1/2$, respectively. In CW EPR experiments, a constant microwave perturbation is applied as the magnetic field is swept. At some magnetic field value, the amplitude of the Zeeman splitting is proportional to the microwave frequency by:

$$\Delta E = h\nu = g\mu_{\mathrm{B}}B_0 \tag{1.2}$$

where ΔE is the amplitude of the Zeeman splitting between the α and β states, h is Planck's constant, ν is the applied microwave frequency, g is the g-value of the paramagnetic center being probed (discussed in depth in the next section), μ_{B} is the Bohr magneton, and B_0 is the applied magnetic field. This can be written in terms of the electron–Zeeman interaction Hamiltonian:

$$\hat{H}_{\mathrm{EZ}} = \mu_{\mathrm{B}}\mathbf{B}_0 g\hat{\mathbf{S}} \tag{1.3}$$

where $\hat{\mathbf{S}}$ is the electron spin angular momentum operator in atomic units of $\hbar$.

Thus, at a specific value of B_0, the direction of the electron's magnetic moment is inverted by absorption of the photon. For most CW EPR experiments, loss in power due to absorption is recorded. The signal is displayed as the derivative of absorption due to the use of lock-in amplifiers, discussed in **Section 1.3**.

The Zeeman interaction also arises from magnetic nuclei—that is, those with non-zero spin

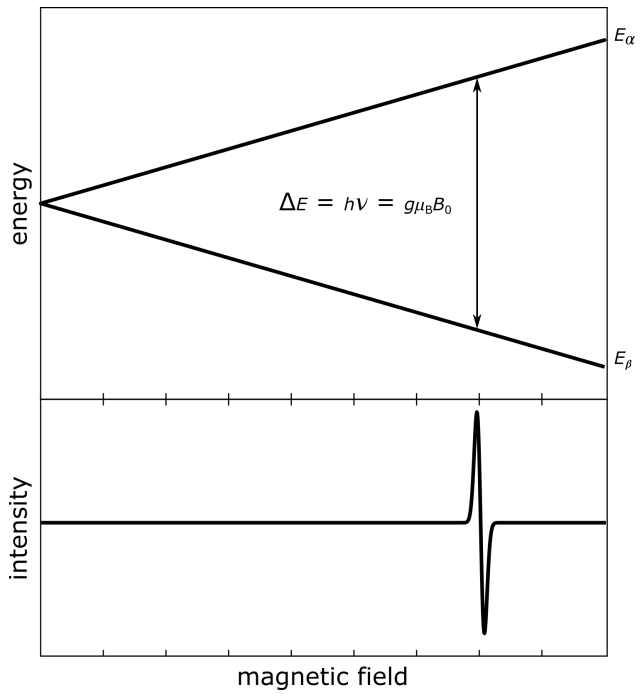

Figure 1.2: A diagram of Zeeman splitting. Top, the energy level separation between α and β magnetic moments, spin down and spin up, respectively. Bottom, the first derivative CW EPR spectrum shown for the resonant transition.

angular momentum—and is defined similarly to $\hat{H}_{\mathrm{EZ}}$:

$$\hat{H}_{\mathrm{NZ}} = -\mu_{\mathrm{N}}\mathbf{B}_0 g_{\mathrm{N}}\hat{\mathbf{I}} \tag{1.4}$$

where g_{N} is the nuclear g-value, μ_{N} is the nuclear Bohr magneton, and $\hat{I}$ is the nuclear spin operator. Unlike electron g-values, g_{N} can be a positive or negative number.[13] Compared to the electron-Zeeman interaction, the nuclear-Zeeman interaction is much smaller and is typically negligible in EPR experiments.

1.2.2 g-values

A g-value can be thought of as an electronic "fingerprint" of a paramagnetic system. Similar local electronic environments will yield similar g-values. Organic radicals generally have g-values close to 2.0023, the g-value of a free electron, g_{e}.[14] Many metal paramagnetic centers have g-values much higher or lower than that of a free electron.

The practitioner's ability to measure precise g-values can help identify the local environment of the paramagnetic system. Since anisotropy exists (**Figure 1.3**), the g-value is described by three principal g-values: g_x, g_y, and g_z.[15] These are chosen to be along the principal axes of the g tensor. Systems in which $g_x = g_y = g_z$ are called isotropic. Isotropic systems are characterized by a CW EPR spectrum that has only one feature. In the case of $g_x = g_y \neq g_z$, the system is called axial. Axial centers are characterized by the presence of two features in the CW EPR spectrum. Finally, in the event that $g_x \neq g_y \neq g_z$, the system is called rhombic. Rhombic paramagnetic centers show three features in their CW spectra. The relationship between the orientation of the paramagnetic center relative to the external magnetic field and its g-values can help elucidate information about its local electronic environment.

For example, from the average g-value of the system alone, it is possible to differentiate between an iron-sulfur cluster that is coordinated with two Cys residues and two His residues (Rieske type, $g_{\mathrm{avg}} = 1.965$) and one that is coordinated with four Cys residues (ferredoxin type, $g_{\mathrm{avg}} \approx 1.88 - 1.91$).[16–19] Determination of local coordination with EPR is helpful

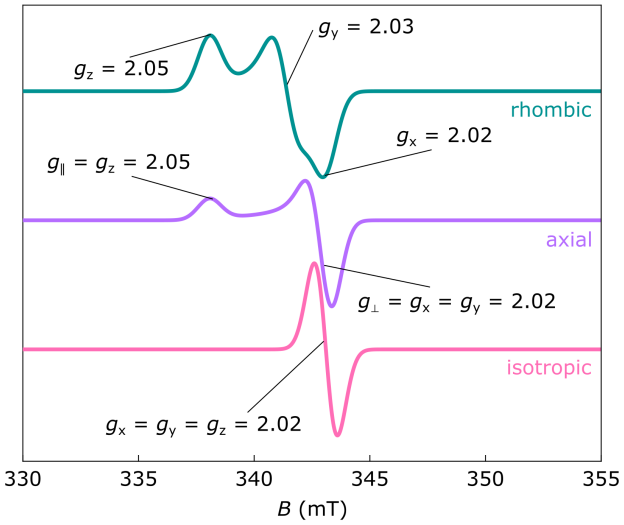

Figure 1.3: The effect of g anisotropy on CW EPR spectra of a simulated $S = 1/2$ system at 9.7 GHz. Top, a rhombic spectrum is shown in teal. Middle, an axial spectrum is shown in purple. Bottom, an isotropic spectrum is shown in pink.

for systems that are difficult to crystallize. Additionally, as opposed to crystal studies, EPR is either done in liquid solution at room temperature or frozen solution at cryogenic temperatures. This is preferable to rigid crystal structures as it is closer to the native protein state. It is also possible to determine spin density of the paramagnetic center by combining advanced EPR techniques with molecular dynamics simulations.[20] **Chapter 4** discusses EPR applied to iron-sulfur clusters in more depth.

1.2.3 Orientation selection

Another consequence of anisotropy is the ability to selectively probe EPR transitions based on the relative orientation of the paramagnetic center. This is most straightforwardly understood in single-crystal CW EPR studies. Upon initial measurement of the sample a given orientation, a device called a goniometer can be used to rotate the sample incremental from 0 to 360°. The goniometer records the offset from the initial measurement angle. It is highly

useful to probe the single crystal along the principal axis of the g tensor, in order to simplify spectral analysis.

This concept of orientation selection is also relevant in pulse EPR techniques. Generally, microwave pulses applied to probe the system have a bandwidth that is narrower than the spectrum. This means only certain portions of the spectrum will be recorded given a specific pulse sequence and magnetic field. By selectively probing along the principal g axes—the z direction is conventionally designated for the direction along the external magnetic field—the experimentalist can selectively probe the transitions along a specific axis, illuminating the local electronic environment along that axis.

1.2.4 Hyperfine coupling

Hyperfine coupling arises from: (i) the through-space dipolar interaction between an electron spin and nearby nuclear spins and (ii) the direct magnetic interaction between the electron and nucleus, known as the Fermi contact interaction. The strength of this interaction can provide key information for studying the structures of chemical environments,[21] as hyperfine coupling can be used to ascertain the ligand environment of a spin system.[22–26]

EPR probes the electron $\Delta m_S = \pm 1$ and nucleus $\Delta m_I = 0$ transitions. These transitions represent an additional splitting in the energy level diagram, and manifests as a splitting the EPR features into $2I + 1$ lines separated by the magnitude of the hyperfine interaction. That is to say, for $S = 1/2, I = 1/2$, there will be 2 peaks in the EPR spectrum; in the case of $S = 1/2, I = 1$ there will 3 peaks in the EPR spectrum. As S and I take higher values, the number of EPR lines grows out of hand quickly, as in the case of a benzene radical.[6]

The hyperfine Hamiltonian is expressed as:

$$\hat{H}_{\mathrm{HF}} = a_{\mathrm{iso}} \hat{\mathbf{S}} \hat{\mathbf{I}} \tag{1.5}$$

where a_{iso} is the isotropic hyperfine interaction for the given nucleus. This description of the hyperfine interaction is simplified for the case of an isotropic hyperfine interaction.

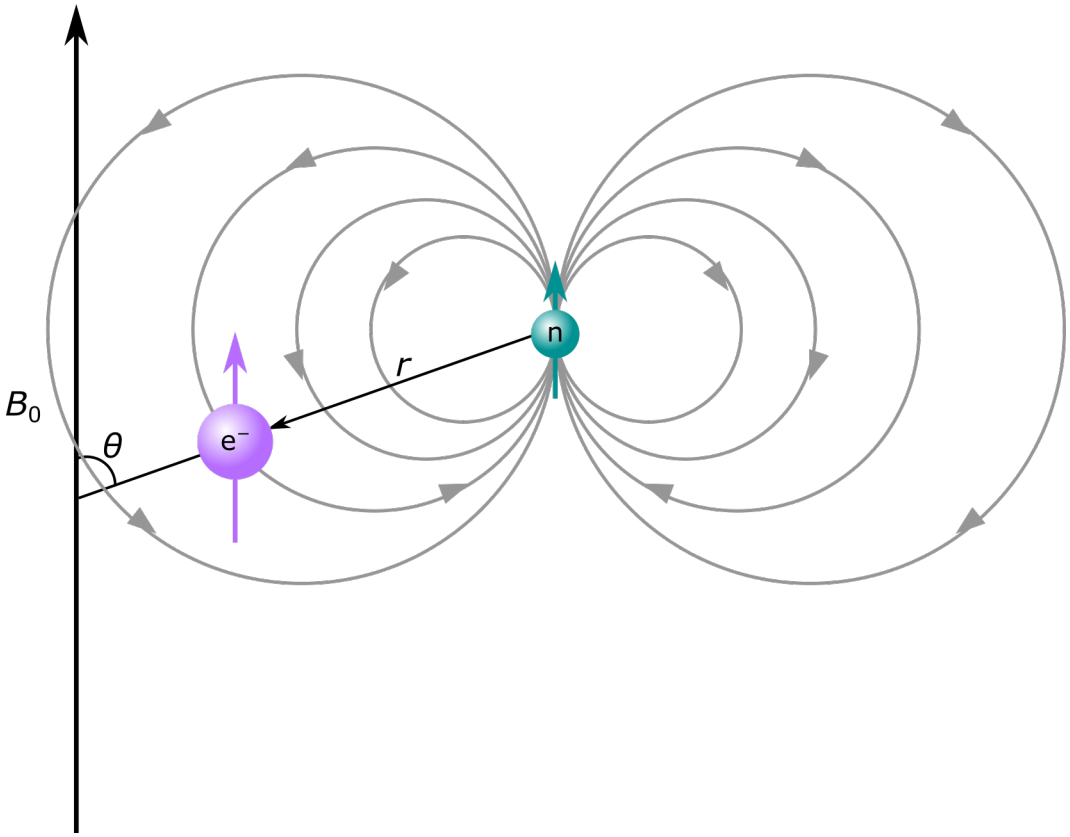

Figure 1.4: Hyperfine coupling between an electron (purple) and a nucleus (teal) in an external magnetic field. The nucleus's magnetic field is indicated in gray. The strength of the nucleus's magnetic field felt at the electron is, like many in magnetic resonance, proportional to $1/r^3$. This makes it possible to extract a proton's distance from the electron with EPR experiments.

Most chemical systems, however, have anisotropic hyperfine couplings, and as such, other techniques must be used to extract hyperfine information from the system of interest. The pulse EPR techniques necessary to study aniostropic hyperfine couplings fall under the category of hyperfine EPR spectroscopy, which will be discussed later in this chapter.

1.2.5 Nuclear quadrupole interaction

The nuclear quadrupole interaction (NQI) arises from a non-spherical nuclear charge distribution for nuclear spin $I > 1/2$ (**Figure 1.5**). The electric quadrupole moment Q quantifies the deviation of the charge distribution from spherical symmetry. There are three types of the charge distribution Q: if it is spherical, then $Q = 0$; if it elongated about the $z-$axis (e.g. in a football shape), then $Q > 0$; and if it is elongated about the $xy-$plane (e.g. in a hamburger shape), then $Q < 0$. The charge distribution is always cylindrical. A nucleus with a non-spherically-shaped charge interacts with a local inhomogeneous electric field (i.e. the electric field gradient is non-zero). As such, the nuclear quadrupole interaction can be thought of as a torquing force when not aligned along the axis aligned with the local electric field gradient direction—that is, when the elongated axis is at some angle from the lowest-energy state. The highest-energy state occurs when the elongated axis of Q is aligned perpendicularly to the lowest-energy state.

In the principal axes system of the electric field gradient (EFG) tensor, the Hamiltonian for NQI is defined as:

$$\hat{H}_{\mathrm{NQI}} = \frac{e^2qQ}{4I(2I-1)}[(3\hat{I}_z^2 - \hat{\mathbf{I}}^2) + \eta(\hat{I}_x^2 + \hat{I}_y^2)] \tag{1.6}$$

where $\frac{e^2qQ}{h}$ is the quadrupole coupling constant in MHz (the inclusion of Planck's constant puts this into frequency units) and η is the asymmetry parameter, defined as $\eta = \frac{V_{xx} - V_{yy}}{V_{zz}}$, where V_{xx} and V_{yy} are the principal components of the EFG along the x- and y-axes, respectively. This asymmetry parameter can be understood as the deviation in the xy plane from the spherical case. The value of e^2q depends upon electronic coupling to the EFG as well as contributions of charged nuclei.

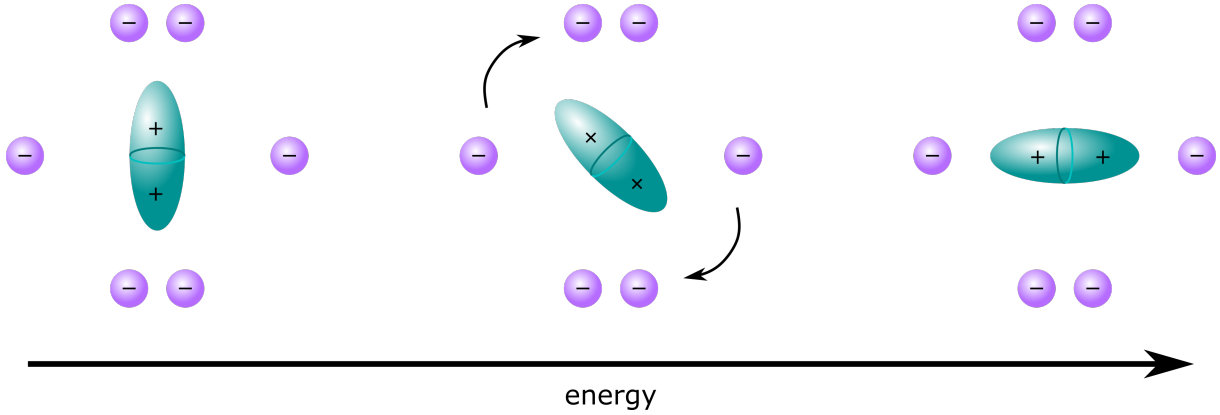

Figure 1.5: Nuclear quadrupole interaction between an electron and a nucleus with a non-spherical charge distribution (a non-zero electric quadrupole moment). Lowest energy when aligned with the largest negative charge, highest energy when aligned perpendicular to the axis of the largest negative charge.

1.2.6 Relaxation

The ability to perform pulse EPR experiments hinges on refocusing of electron spins upon detection. The time frame over which electron spins can be refocused is directly related to the time frame over which the probed state returns to equilibrium. This phenomenon is known in magnetic resonance as relaxation and plays an important role in all magnetic resonance experiments. A thorough explanation of the significance of relaxation can be found in Eaton and Eaton 2000.[27] There are two fundamentally different types of relaxation, longitudinal and transverse.

Longitudinal relaxation

Spin-lattice relaxation is a longitudinal relaxation process called T_1. This relaxation process describes the time it takes for the magnetic moment along the direction of the applied magnetic field, conventionally the z-axis, to return to equilibrium. The value of T_1 can be measured using an echo-detected (**Subsection 1.4.3**) inversion recovery experiment in

which a preparatory π pulse is used to knock the magnetic moment of the electron spins into the $-z$ direction. After some time T, a pulse sequence of $\pi/2 - \tau - \pi-$echo is applied (**Figure 2.3**). The measured echo amplitude is recorded as a function of the delay T between the preparation π pulse and the detection sequence. The recorded echo amplitude reaches maximum and levels off, indicating that the populations of the two states involved have reached equilibrium, as the highest number of spin packets are recorded at the maximum echo amplitude.

Spectral diffusion

Spectral diffusion arises from the stochastic flips of coupled nuclei and electrons causing changes in an electron's resonance frequency during the time it takes to perform the pulse sequence. This results in incomplete rephasing of electron spins, which manifests as lower inversion recovery and a decreased phase memory time. This phenomenon encompasses many different types of relaxation.

Instantaneous diffusion

Instantaneous diffusion is a special type of spectral diffusion that arises from spin flips introduced by microwave pertubations. When there is sufficiently large spin concentration, one must consider the effects of instantaneous diffusion on relaxation. The effect arises from coupling of two spins, A and B. For a given A spin, the coupling to nearby B spins varies based on the distance of the two spins. Thus when B spins are flipped by a pulse, the A spin experiences different dipolar couplings from the B spins. This causes the distribution of the precession frequencies of the A spins to widen. This moves some excited A spins and manifests as an echo of lower amplitude.

Phase memory time

The phase memory time T_{M} in EPR is akin to the T_2 in NMR. As opposed to NMR, in which T_2 measures just transverse relaxation, T_{M} encompasses a variety of relaxation mechanisms that cause dephasing of electron spin packets, including nuclear spin diffusion, instantaneous diffusion, and spectral diffusion. It is possible to limit the types of relaxation mechanisms experienced by the sample—and thereby slow down the system's relaxation—by lowering the temperature, decreasing spin concentration, decreasing the level of matrix protonation, degassing, introduction of glassing agent, amongst many other techniques.

The phase memory time describes the timescale over which electron spins remain coherent in the *xy*-plane. There are a few methods for measuring a sample's T_{M}, but the most straightforward is the Hahn echo decay experiment. In such an experiment, the two pulse Hahn echo pulse sequence $\pi/2 - \tau - \pi - \tau -$ echo is applied to the system, and the echo amplitude is recorded as a function of the sequence length 2τ. Generally, the phase memory time is extracted by fitting a stretched exponential of the form $V(2\tau) = V_0 \cdot \exp[-(2\tau/T_{\mathrm{M}})^x]$ to the echo decay such that T_M is equal to the point in time when the echo has decayed to 1/e of its amplitude at V_0. Here, x is the stretching factor and typically has a value of 1.5–3.[28]

Some of the major contributors to decoherence include nuclear-spin-driven electron-spin-decoherence, methyl rotations, and instantaneous diffusion. Nuclear-spin-driven electron-spin-decoherence will be addressed in depth in **Chapter 2**. Briefly, it is a decoherence mechanism resulting from the coherent flip-flop of nuclei interacting with the unpaired electron spin. Methyl rotations and librational motions of the molecule can also contribute to dephasing of the electron spin packets resulting in time-dependent fluctuations in the local field experienced at the electron.

1.2.7 The Spin Hamiltonian

Combining the interactions discussed above, we can get the total spin Hamiltonian:

$$\hat{H} = \hat{H}_{\mathrm{EZ}} + \hat{H}_{\mathrm{NZ}} + \hat{H}_{\mathrm{HF}} + \hat{H}_{\mathrm{NQI}} \tag{1.7}$$

It is worth nothing that for systems of $S = 1/2$ at typical magnetic fields (0.3 T or larger), $\hat{H}_{\mathrm{EZ}}$ dominates the Hamiltonian. As such, for many systems of $S = 1/2$, the full system can be modeled simply by the electron Zeeman interaction.

1.3 Instrumental Components

To the uninitiated, a daunting aspect of mastering EPR spectroscopy is familiarizing oneself with the instrumental setup. The intent of this section is to familiarize the reader with the individual instrument components involved in EPR spectroscopy, and to understand the relationships amongst various components. For a more in-depth discussion of instrumentation, see Reijerse and Savitsky 2017.[29]

Besides the magnet itself (which, for most EPR applications, is an iron-core electromagnet controlled via a Hall probe), the most important aspect of any EPR setup is the microwave bridge. The bridge is the source of the microwave radiation in both CW and pulse dipolar EPR spectroscopy. There are several frequency bands at which EPR is performed: 3 GHz (S-band), 9.5 GHz (X-band), 34 GHz (Q-band), 95 GHz (W-band), and 130 GHz (D-band). The major internal features of the bridge are the microwave source, the signal arm, the reference arm, and the detector.

Figure 1.6 shows a block diagram of a typical CW EPR spectrometer. In CW spectrometer setups, the microwaves are produced at the source and split into two paths: the reference arm and the signal arm. The microwaves in the signal arm go through a circulator or a directional coupler[30] and travel in a waveguide down to the resonator, which houses the sample between the magnet's poles. The coupling of the waveguide to the resonator is controlled by the iris screw. This a screw that is raised or lowered to reach ideal coupling between the resonator

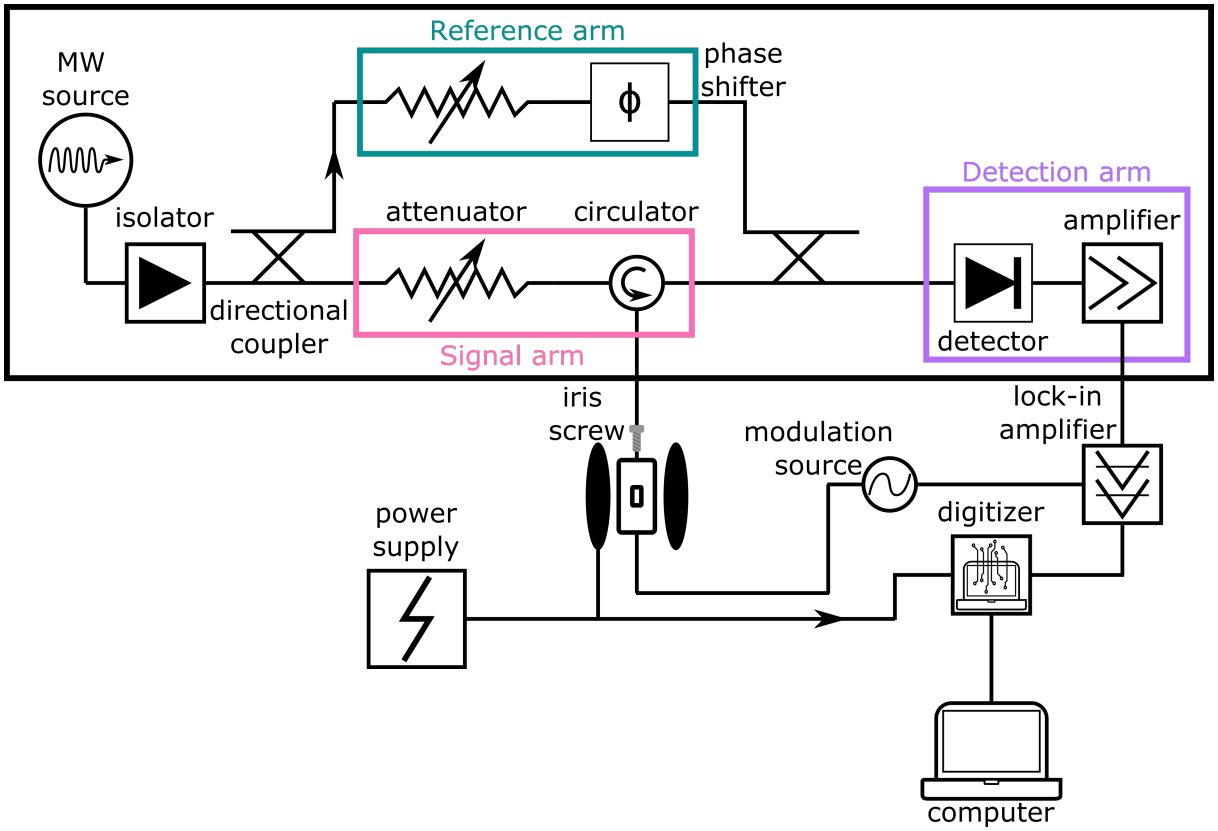

Figure 1.6: Block diagram of a typical CW EPR spectrometer. The three main arms of the spectrometer, the signal, reference, and detection arms are highlighted in pink, teal, and purple, respectively.

and waveguide. The resonators typically used in CW EPR spectroscopy maximize the B_1 field at the sample active volume, which subsequently minimizes the E_1 field at the same volume. The coupling between the waveguide and resonator is adjusted with an iris screw to either be critically coupled (in the case of CW) or overcoupled (as is desired in most pulse dipolar EPR experiments). When the resonator is critically coupled, the iris screw is adjusted such that no power at the frequency resonant with the resonator cavity is reflected backwards. If this condition is met, no microwave power will be reflected from the resonator up the waveguide absent an EPR transition. In the case of pulse dipolar EPR experiments, the resonator is overcoupled to broaden the frequency bandwidth of the resonator because a broader frequency range is required to excite the full spectrum.

Absorption in the sample changes the coupling between resonator and waveguide such that some microwave power is reflected up the waveguide and is combined with the power from the reference arm. The microwaves along the reference arm go through a phase shifter to ensure they are in phase with the reflected power from the signal arm. The two paths rejoin for detection at the detector before being amplified, digitized, and sent to the acquisition computer.

While the CW EPR experiment is an absorption, the spectrum is usually shown as a first derivative. This is a result of the use of a lock-in amplifier, which aids in the detection of signal from noisy sources. The lock-in amplifier is used in conjunction with field modulation to improve the signal extracted in the EPR experiment. It is not employed in pulse EPR.

Moving from CW spectrometers to pulse spectrometers, the console becomes much more intricate. Pulse EPR requires the generation of microwave pulses guided by the console's connection to the waveform generator. It is becoming increasingly common for the microwave pulses to be generated by an arbitrary waveform generator (AWG). The benefit of the AWG is that shaped pulses have more uniform excitation bandwidths than rectangular pulses do. These pulses are powered by an additional amplifier, which is either a high-power traveling wave tube (TWT) amplifier or a medium-power solid-state amplifier.

1.4 EPR Experiments for Structural Biology

1.4.1 CW EPR

CW EPR is a highly useful technique for a large swath of biological studies.[4,6,31] Many significant biological processes involve metal clusters in metalloenzymes, whose local metal coordination and redox state can be determined through CW EPR. Electron transfer chain processes can be studied via CW EPR, as well as a host of redox reactions. EPR is somewhat unique in that it is very selective and cannot detect anything besides paramagnetic species. This means very specific information about local environments can be determined. For example, Fe−S clusters have such specific g-values that it is possible to determine cluster composition (e.g. 2Fe−2S or 4Fe−4S), local coordination (e.g. Rieske or ferrodoxin), and redox state (for example, a $[2Fe{-}2S]^2+$ has spin $S = 0$ and is thus EPR-silent, while a $[2Fe{-}2S]^+$ has spin $S = 1/2$ or $9/2$ and is EPR-active) from CW EPR.[16–19] Researchers interested in exploring metal loading efficiency can use the second integral of the CW EPR spectrum to perform spin quantification.[4]

Additionally, the specificity of detection allows for CW EPR measurements to be conducted in-cell, given protein over-expression.[32] EPR on rotationally mobile spin labels can provide insight into local structural order or disorder, particularly within cell membranes or on proteins before and after a binding event.[33] This can be used to monitor a conformational change or binding event. CW EPR can also be used to estimate distances between two paramagnetic centers in proteins.[34]

Many systems can be investigated at room temperature with CW EPR, but transition metals often require cryogenic temperatures to reach a polarization level that can be probed, and more importantly, lowering temperatures extends coherence, as metals have very short T_1 and T_M values at room temperature.

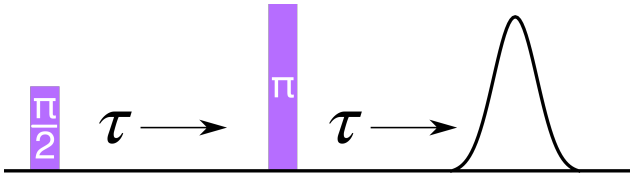

Figure 1.7: The Hahn echo pulse sequence is the foundation of many other pulse EPR experiments. In this pulse sequence, a $\pi/2$ pulse is applied, knocking spins from alignment with the external magnetic field into the xy plane. After some time τ, a π pulse is applied, causing an inversion of the spins in the xy plane. The echo is collected at time τ after the π pulse.

1.4.2 Pulse EPR experiments

Due to the selectively of EPR to paramagnetic systems, it can provide incredibly illuminating information about the system. For example, sparse distance measurements from pulse EPR can be used in conjunction with computational methods to model protein structures to obtain structures that are difficult to elucidate by other methods.

Fundamental Pulse EPR Experiments

The Hahn echo is one of the cornerstone experiments of pulse EPR, and it is one of the more straightforward ways to describe what is measured in pulse EPR. The Hahn echo pulse sequence $\pi/2 - \tau - \pi - \tau -$echo is below (**Figure 2.3**).

Upon application of an external magnetic field on a paramagnetic sample, the magnetic moments of the spins are aligned with the external magnetic field, which is conventionally designated the z direction. The spins are knocked into the xy plane by the application of the $\pi/2$ pulse. Since the spin packets all exist in slightly different local microenvironments, they precess at different frequencies. During the interpulse delay τ, the precessing spins will spread out based on their precession frequency, from fastest to slowest. The π pulse will cause the fastest spin packets to exchange places with the slowest spin packets. During the

next delay τ, the high- and medium-frequency precession spins catch up with the slower low-frequency precession spins. This phenomenon is called refocusing, and is the point at which the EPR signal is detected in what is called the echo.

When the integrated Hahn echo is recorded at various magnetic field values, we call this the echo-detected field sweep (EDFS). Unlike CW EPR experiments, the EDFS is recorded as an absorption.

Another experiment that utilizes the Hahn echo pulse sequence is the Hahn echo decay, from which the phase memory time T_{M} can be extracted (**Subsection 1.2.6**). In this experiment, the integrated echo is recorded for increasingly large values of τ. This means the echo amplitude is recorded as a function of 2τ.

1.4.3 Advanced Pulse Dipolar EPR Experiments

There are numerous pulse sequences that go beyond the Hahn echo, although they all utilize detection of the refocused spins at the echo. The remainder of this section will discuss experiments that are of significance for structural biology and biophyics.

Inversion recovery experiments are used to determine the spin lattice relation time T_1. In these experiments, the magnetic moment along the z axis is monitored by varying the delay time T in the pulse sequence $\pi - T - \pi/2 - \tau - \pi - \tau -$ echo. This informs the researcher how long the spins stay excited before they return to the ground state (i.e. realign with the external magnetic field). This is important information for selecting overall pulse sequence lengths.

In addition to knowing the relaxation behavior of a paramagnetic system, it is important for researchers to know the ideal pulse lengths to achieve the desired pulse flip angles. To do this, a nutation experiment (also called a Rabi experiment) is used. An inversion pulse is applied and after a delay the sequence $\pi/2 - \tau - \pi - \tau -$ echo is applied to the sample. The inversion pulse is varied in length. The echo signal oscillates; this Rabi oscillation reaches a

minimum when the spins have been inverted 180°.

Often, structural biologists and biophysicists turn to EPR to answer structural questions, such as conformational change upon a binding event, in systems that are not well-suited to other structural characterization techniques. Perhaps the most well known amongst the numerous pulse dipolar EPR methods for structural characterization is double electron–electron resonance (DEER) spectroscopy. In this experiment, the time-domain dipolar coupling between two paramagnetic centers on a protein or polypeptide is probed and, through numerical methods, a full-ensemble probability distribution can be extracted. The underlying principles behind this experiment can be understood through an analogy using bar magnets. If two bar magnets are held close together, they will experience a strong attractive or repulsive force. If the bar magnets are far apart, the attraction or repulsion will be weak. In the DEER experiment, the attraction or repulsion experienced by one paramagnetic center (bar magnet) upon a 180° inversion of the other paramagnetic center is measured. Typically the 4-pulse sequence: $\pi/2 - \tau_1 - \pi - \tau_1 + T - \pi_{\text{pump}} - \tau_2 - T - \pi - \tau_2 -$echo is used. In this sequence, the pump pulse is applied at a different frequency than the other three observer pulses. A more complete explanation of the DEER experiment can be found in **Chapter 3**.

One technique to elucidate hyperfine coupling information is electron spin echo envelope modulation (ESEEM). There are two common ESEEM pulse sequences, the two- and three-pulse ESEEM experiments.[35] When performing hyperfine spectroscopy there are three hyperfine coupling regimes to consider: the weak, the intermediate, and the strong. The weak coupling regime occurs when the magnitude of the hyperfine is less than two times the magnitude of the Larmor frequency, that is $|A| < 2|\nu_{\text{Larmor}}|$. Upon Fourier transformation of the time domain hyperfine spectroscopy data, resonances will be centered around ν_{Larmor} of the nucleus and split by $|A|$. The intermediate coupling regime occurs when the magnitude of hyperfine coupling is approximately equal to twice the magnitude of the Larmor frequency, $|A| \approx 2|\nu_{\text{Larmor}}|$. Like many cases of intermediate regimes, the intermediate hyperfine coupling regieme is difficult to study. Finally, the strong (hyperfine) coupling regime occurs

when $|A| > 2|\nu_{\text{Larmor}}|$. Peaks will appear in the frequency domain with resonances centered around $|A|/2$ and split by $2|A|$.

In two-pulse ESEEM, the time incrementation occurs with the spins in the xy plane, thus the length of trace recorded is T_{M} dependent.

In three-pulse ESEEM, the time incrementation occurs with the spins in the $-x$ direction, which means the length of the trace you can record is T_1 dependant. The general goal of the experiment is to determine the hyperfine coupling of magnetic nuclei to the paramagnetic center. The pulse sequence is $\pi/2 - \tau - \pi/2 - T - \pi/2 - \tau -$ echo. The first two $\pi/2$ pulses are called the preparation pulses, in which electron coherence is transferred to nuclear coherence. The evolution time T is varied and the third $\pi/2$ pulse prepares the electron spins echo detection by transferring the nuclear coherence that has evolved during T back to electron coherence. A major limitation of three-pulse ESEEM is blindspots, that is τ dependence on the three-pulse ESEEM spectrum that can obscure features at certain frequencies. Additionally, there is often too much broadening from non-preserved nuclear coherence to assign nuclei specifically.

Four-pulse ESEEM improves experimental resolution, although it also results in blindspots. This experiment is typically done in two dimensions and is known as hyperfine sublevel correlation (HYSCORE) spectroscopy. HYSCORE utilizes the conversion from electron coherence to nuclear coherence, evolution, and back-conversion from nuclear coherence to electron coherence that is common to many ESEEM experiments. The difference from three-pulse ESEEM is that T is split into t_1 and t_2 by a mixing π pulse. The nuclei evolve after the preparation pulses, and then nuclear coherence is transferred to nuclear coherence by the mixing pulse, followed by the second evolution t_2 and the detection $\pi/2$ pulse seen in three-pulse ESEEM. HYSCORE is a two-dimensional experiment as t_1 and t_2 are varied independently. This aids in improving resolution, although τ dependent blindspots are still seen in the two-dimensional HYSCORE spectrum.

These are just a select few of the numerous EPR experiments that may be of use to for structural biology applications. Goldfarb-Stoll[5] is a very useful resource for more in-depth discussions of all the pulse EPR experiments discussed above.

1.5 Summary

EPR spectroscopy is highly useful for myriad applications to paramagnetic systems. Its use in structural biophysics, quantum information processing, electrochemistry, and other areas, in addition to its selectivity to paramagnetic signals, make EPR an important spectroscopic technique. Methodology studies are of great importance to drive the field forward. The work detailed in the following chapters focuses on how experimental and sample conditions affect measurement of EPR. **Chapter 2** investigates the decoherence behavior of a variety of organic radicals in frozen solution with varied sample matrix composition. **Chapter 3** presents a rigorous experimental investigation of spin label contributions contributions to the $P(r)$ obtained in the DEER experiment. **Chapter 4** briefly touches on an applied EPR project that determined the coordination of a novel iron-sulfur cluster involved in iron homeostasis.

Chapter 2

ELECTRON SPIN DECOHERENCE BEHAVIOR IN FROZEN SOLUTIONS

This chapter describes an investigation of the effect of the sample matrix on dipolar EPR spectroscopy, done in collaboration with Samuel M. Jahn, another graduate student in the Stoll group. Some of this work has been published.[36] This study is based upon the fact that the distance resolution of the DEER experiment is limited to the length of the experimental time trace, which is governed by the phase memory time T_M of the paramagnetic center of interest. The T_M of a molecular spin system is akin to the T_2, or spin–spin relaxation time, the time for the spin to return to equilibrium in the plane perpendicular to the applied magnetic field. The main difference between T_M and T_2 is that T_M also encompasses the relaxation from magnetic field inhomogeneities.[37]

Long T_M values are sought after in pulsed dipolar spectroscopy. A long T_M value means a longer distance can be measured in a protein.[38] The significance of decoherence behavior extends beyond measuring coarse-grain protein structure. Additionally, there are some systems, such as spin labeled proteins in a cell membrane, that suffer from extremely short phase memory times. Extending the time over which the spin labels are coherent will extend the limit of in-cell EPR measurements. An *in silico* prediction for T_M values before synthesizing molecular spin qubits guide site selection for spin labeling proteins for course grain structure determination with EPR.

This chapter presents our recent work on an experimentally validated quantitative prediction method for decoherence behavior of small molecular spin centers in solution.[36] This work is foundational to the ultimate goal of *in silico* prediction of decoherence behavior of spin labels

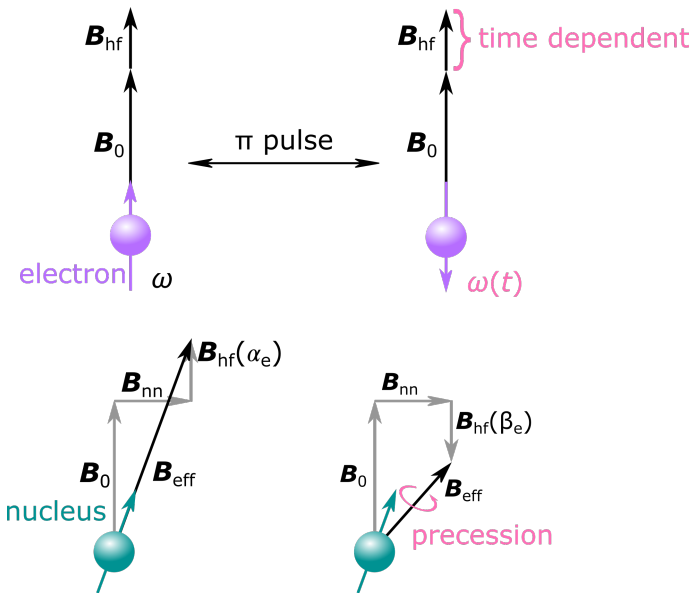

Figure 2.1: Vector model of nuclear spin driven electron spin decoherence. Before application of the π pulse, the hyperfine field B_{hf} is aligned parallel to the external magnetic field B_0, and the nuclear field B_{nn} is at some direction from the external field. The π pulse inverts the magnetic moment of the spin (from α to β or vice versa), and as such causes a change in the hyperfine field B_{hf} such that it is aligned antiparallel to the external field.

on a protein. Optimal *in silico* selection of sites for spin labeling will reduce experimental troubleshooting in the event that the rate of decoherence is too fast to measure the distance between the two spin labels.

2.1 Nuclear-spin-driven electron spin decoherence

At sufficiently low temperatures and electron spin concentrations, electron decoherence is driven by nearby nuclear spins.[39,40] This mechanism is historically called nuclear spin diffusion, and has been described in a semi-classical manner as arising from stochastic, energy-conserving flip-flops of pairs of nuclei coupled to an electron. These flip-flops cause spectral

diffusion of resonance frequencies of the electron spins, leading to decoherence.[41–43] The issue with this semi-classical picture is that it is not predictive and gives no insight into the physical origins of the assumed flip-flop rate.

A potentially more descriptive understanding of the effect described in the previous paragraph, which will be called nuclear-spin-driven electron spin decoherence in this work, is shown in **Figure 2.1** Before application of the π pulse, the hyperfine field at the nucleus is along the direction of the applied magnetic field. Upon the application of the π pulse, the hyperfine field is anti-parallel to the applied magnetic field. This results in a tilt of the local magnetic field and causes the nucleus to precess, thus creating a time dependent magnetic field on the electron with components for each nuclear Larmor frequency. The phase accumulation before the π pulse is incomplete, which reduces the intensity of the refocused spins at the time of the echo.

The overarching goal of this project is to optimally select spin labeling sites for structural measurements. The work described in this chapter gives experimental validation of a first-principles-based model for *in silico* prediction of T_M for molecular spin qubits that utilizes the couple cluster expansion method. This method builds on the single-crystal method for T_M prediction from Witzel and coworkers and extends it into glassy solutions.[44] It has previously been applied in the crystalline solid state to systems such as copper(II) β-diketonate complexes.[45]

Our first-principles based description of electron dephasing results in a simple stretched exponential of the form

$$V(2\tau) = V_0 \cdot \exp[-(2\tau/T_M)^x] \tag{2.1}$$

with a stretching factor x between 2 and 3. In **Equation 2.1**, τ is the inter-pulse spacing, x is the stretching factor mentioned above, and T_M is the phase memory time of the electron. A stretching factor above two has been proposed to be indicative of nuclear spin diffusion mechanisms, while a stretching factor below two is attributed to nuclear motion mechanisms—such as molecular rotation or tumbling.[45]

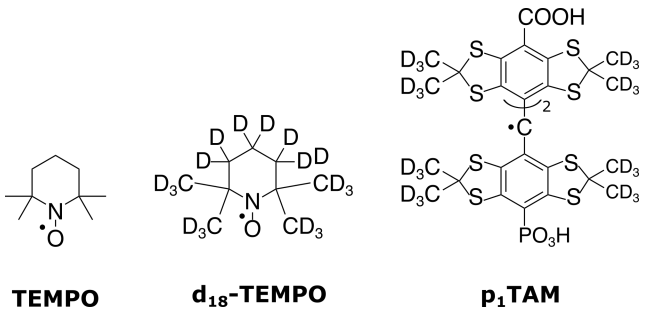

Figure 2.2: The organic radicals used in this study. Left to right: TEMPO, d_{18}-TEMPO, p_1TAM.

2.2 Methods

Three organic radicals were used to investigate the effects of sample matrix composition on phase memory times of electron spins in dilute, frozen solutions.

2.2.1 Samples

2,2,6,6-tetramethylpiperidine-1-oxyl (TEMPO) was obtained from Sigma-Aldrich; 2,2,6,6,-tetramethylpiperidine-d_{18}-1-oxyl (d_{18}-TEMPO) from CDN Isotopes; and the trityl radical p_1TAM was gifted to us by Dr. Valery V. Khramtsov and Dr. Benoit Driesschaert from West Virginia University. Its synthesis was previously described (**Figure 2.2**).[46] Glycerol was used as a cryprotectant for all samples. Glycerol was purchased from Fisher Scientific, d_3-glycerol from Sigma Aldrich, and d_5- and d_8-glycerol were purchased from CDN Isotopes.

For the temperature series measurements, the concentrations of TEMPO, d_{18}-TEMPO, and p_1TAM were approximately 200 μM, 100 μM, and 10 μM, respectively. These concentrations were chosen to minimize decoherence effects from instantaneous diffusion (ID),[47] which is described by an exponential decay with decay time constant t_{ID} given by:[48]

$$V(2\tau) = \exp[-2\tau/T_{\mathrm{ID}}] \tag{2.2}$$

with the concentration c (in spins/m^3) and the excitation efficiency η. Estimating $\eta \approx 0.25$, based off the bandwidth of the pulses, for TEMPO at Q-band gives t_{ID} of 80 μs for 100 μM and 40 μs for 200 μM. Estimating $\eta \approx 1$ for p_1TAM, gives t_{ID} of 200 μs for 10μM. These are all significantly longer than the experimentally observed timescale for complete dephasing of electron spin ($4 - 5$ μs).

For the deuteration investigation, only d_{18}-TEMPO was used at a concentration of 5 μM for a t_{ID} of approximately 1900 μs. The glycerol concentration series was conducted with TEMPO in mixtures of TEMPO, H_2O, and glycerol and the percent glycerol (w:w) varied from 10% to 70%.

Samples for all other measurements were made with a water:glycerol (deuterated or not) ratio of 1:1 (w:w), as this proved to be a sufficient concentration of cryoprotectant to prevent aggregation effects from contributing to decoherence on the timescales of the nuclear-spin-driven electron spin decoherence.

Q-band samples were prepared by transferring 30-50 μL of sample by syringe into 1.50 mm O.D. 1.10 mm I.D. quartz tubes (Sutter Instrument). For the X-band measurement shown in the SI, ca. 100 μL of sample was transfered by syringe into a 4 mm O.D. 3 mm I.D. quartz tube (Wilmad-LabGlass). The samples were snap frozen in liquid nitrogen over approximately 10 seconds while gently shaking the submerged tubed in the nitrogen. The samples above 40% glycerol were visually good optical glasses.

Measurement Conditions

The Q-band experiments (ca. 33.8 GHz, 1.2 T) were preformed on a Bruker Elexsys E580 spectrometer equipped with a Bruker D2 dielectric resonator. The microwave power was amplified with a 300 W TWT amplifier (Applied Systems Engineering) or with a 10 W solid state amplifier (many thanks to the Lorigan lab at Miami University Ohio for the loan). The X-band experiment on d_{18}-TEMPO was performed on the same spectrometer equipped with a Bruker MD4 dielectric resonator and a 1 kW TWT amplifier (Applied Systems Engineering).

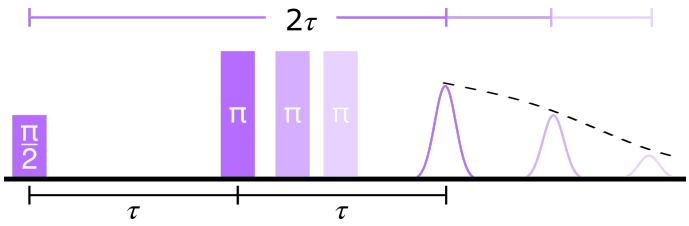

Figure 2.3: The Hahn echo pulse sequence is perhaps the most straightforward way to measure decoherence behavior. To do so, the pulse sequence $\pi/2 - \tau - \pi - \tau -$ echo is used. The interpulse delay τ is incremented, and the echo amplitude is measured as a function of 2τ.

The magnetic fields of the measurements were determined by taking the field value that corresponded to the peak of the echo detected field sweep (EDFS). If there was a large out-of-phase component at the maximum of the EDFS, the field was selected to minimize the out-of-phase signal while staying sufficiently close to the maximum of the EDFS. Optimal pulse lengths were selected from the first minimum of the Rabi oscillation. At Q-band, the $\pi/2$ and π pulse lengths for d_{18}-TEMPO, TEMPO, and p_1TAM were: 10/20 ns, 26/52 ns, and 14/28 ns, respectively. The variations in optimal pulse length arise due to slight differences in sample tube placement and geometry, sample filling, and resonator coupling and profile. For the X-band measurement on d_{18}-TEMPO, $\pi/2$ and π pulses of 14/24 ns were used. The shot repetition times were not determined by inversion recovery experiments due the long T_1 values of the samples at 20 K. The timescale necessary to perform the inversion recovery experiment at 20 K leads to issues of TWT gating. Instead, the shot repetition times were sample and temperature dependent, determined by increasing the value of the shot repetition time until there was no longer any change in recorded echo intensity, to avoid T_1 saturation. For the experiments at 20 K, typical shot repetition times were on the order of 700 ms to 1 s for the p_1TAM and TEMPO samples, and approximately 120 ms for the 5 μM d_{18}-TEMPO.

The Hahn echo decay experiment was performed using the pulse sequence $\pi/2-\tau-\pi-\tau-$echo by varying τ. The minimum value of τ for d_{18}-TEMPO and p_1TAM was 250 ns and 200 ns for TEMPO. At X-band, the minimum τ value was 400 ns. The maximum value of τ was chosen to be sufficiently long such that 2τ was sufficient to capture the complete decay of echo intensity.

2.2.2 Temperature series

To validate the couple cluster expansion model for electron dephasing, we used two nitroxides and a trityl radical: h_{18}-TEMPO, d_{18}-TEMPO, and p_1TAM in H_2O and glycerol and D_2O and d_8-gylcerol. We selected 50% (w:w) of glycerol:H_2O or d_8-glycerol:D_2O to prevent aggregation (**Figure 2.5**). The concentrations of the samples were chosen to minimize the effects of instantaneous diffusion: 200 μM for h_{18}-TEMPO in H_2O, 100 μM for d_{18}-TEMPO in H_2O, 10 μM for h_{18}-TEMPO in D_2O, 10 μM for d_{18}-TEMPO in D_2O, and unknown concentrations for p_1TAM due to solubility issues. We determined T_M values by performing Hahn echo decay experiments utilizing a $\pi/2-\tau-\pi-$ echo pulse sequence (**Figure 2.3**), where typical $\pi/2$ and π values were 10 and 20 ns, respectively. Measurements were taken at Q-band (ca. 33.8 GHz), and temperature dependence from 20-60 K was investigated.

2.2.3 Deuteration series

The effect of bulk matrix deuteration was studied by measuring samples that were mixture of 5 μM d_{18}-TEMPO in 1:1 (w:w) H_2O : glycerol and D_2O : d_8-glycerol. All measurements were conducted at 20 K. The experiments were performed in the same manner as described above, although with two separate echo decay experiments performed and stitched together in order to measure the ESEEM oscillations at short times in the deuterated samples. The first experiment was performed with a step size of 10 ns out to approximately 11 μs. The second experiment was performed with a step size of 624 ns out to approximately 250 μs.

2.2.4 Structure-based simulations

The structure-based quantum simulations were performed by Samuel Jahn. For a more detailed description of the simulations, see Canarie, Jahn, Stoll 2020.[36] First, a molecular dynamics (MD) simulation was generated for each molecule of interest solvated in water. The structures of the molecules used in this study were geometry optimized following Oganesyan.[49] Density functional theory was performed using ORCA 4.01[15] with the B3LYP functional and the SV(P) basis set. After calculating the optimized geometry, atomic charges were calculated with CHELPG (charges from electrostatic potentials using a grid-based method). These charges were substituted into a CHARMM-GUI generated topology file.

To perform the MD calculations, GROMACS with the CHARMM36[50] and the particle mesh Ewald method for long-range electrostatics was employed. The energy of the water molecules around the water was minimized to generate the initial MD structure. As pure water and 1:1 (w:w) water:glycerol have approximately the same density at room temperature: 110.8 mol/L and 111.4 mol/L,[51] respectively. The molecules were solvated exclusively with water. The effect of snap freezing the sample was accounted for by propagating the structure at 300 K for 25 ns, followed by propagation at 100 K.[52]

The spin Hamiltonian used contained the electron Zeeman interaction; the sum over all nuclear spins of the nuclear Zeeman interaction, the hyperfine coupling, the quadrupole couplings; and the terms that couple different nuclear spins. All hyperfine couplings, except ^{14}N, were calculated using the point-dipole approximation. The experimentally determined hyperfine values for ^{14}N were $[-13.9, -13.9, 122.3]$ MHz[53] and the quadrupole coupling tensor $e^2qQ/h = 3.5$ MHz and $\eta = 0.68$ were used.[54]

Explicit time propagation via integration of the Liouville–von Neumann equation was employed to simulated the Hahn echo decay. A home-written (S. Jahn) implementation of the ensemble cluster correlation expansion (CCE) method was used.[55,56] Previous work

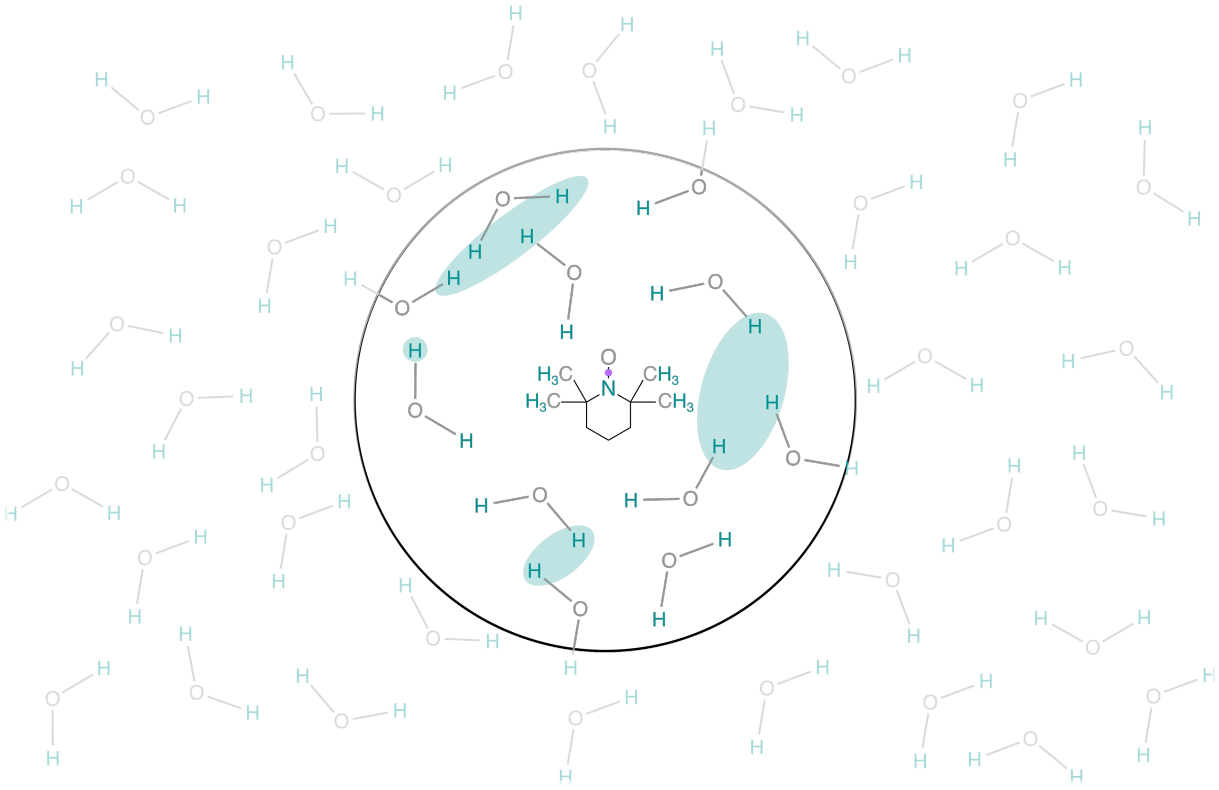

Figure 2.4: Illustration of coupled cluster expansion. The nuclei included in the simulation are limited to a sphere around the electron (drawn as a circle). The nuclei are then broken down into clusters of various sizes (teal areas), the signals from individual clusters are simulated and combined in a product to produce the overall simulated signal.

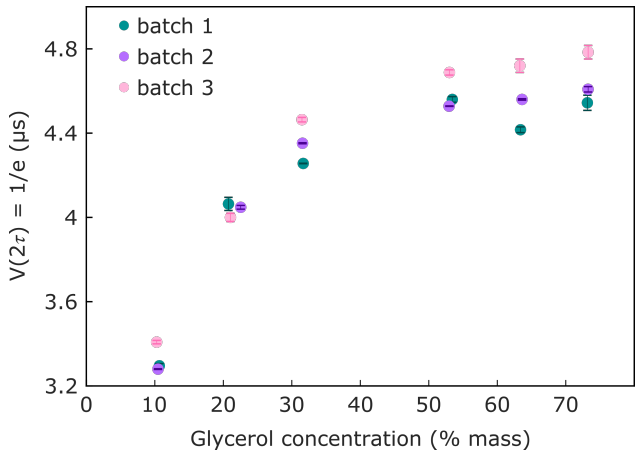

Figure 2.5: Investigation of aggregation behavior. The (w:w) percentage of glycerol is on the horizontal axis. The vertical axis is the phase memory time T_M. This demonstrates that at least 40% (w:w) glycerol is needed to prevent aggregation from negatively impacting T_M.

employing the CCE method has been done to successfully predict decoherence behavior of paramagnetic defects and centers in crystals,[45,57] however, it had not been used on systems in solutions before this work. Briefly, this method breaks down a highly complex system of nuclei coupled to an electron spin by truncating the system to only include nuclei within radius R of the electron and clustering coupled nuclei within a distance of r_0 of each other (**Figure 2.4**). The contributions from each cluster of nuclei is taken and summed together to make the total signal. The full description of the theory may be found elsewhere.[58]

2.3 Results

2.3.1 Glycerol series

The investigation of glycerol concentration's (w:w) influence on phase memory time demonstrates that 40-50% glycerol is necessary to prevent aggregation from contributing to electron spin dephasing (**Figure 2.5**).The missing data points at 40% (w:w) glycerol in **Figure 2.5** are worth noting. It was not possible to measure a 40% (w:w) sample of glycerol because cap-

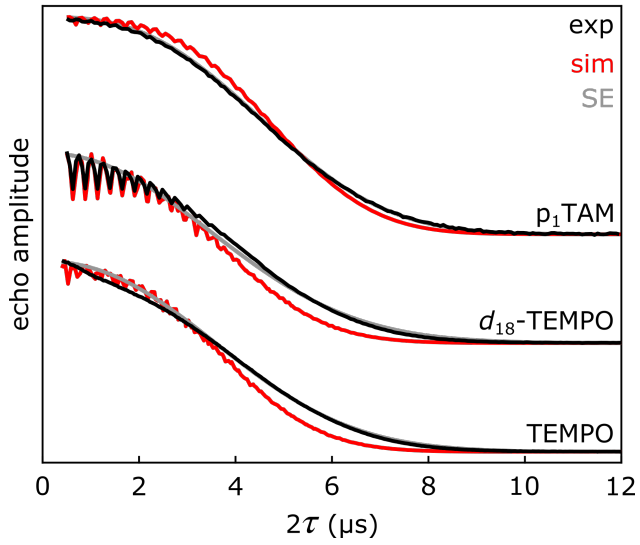

Figure 2.6: Experimental (black), simulated (red), and stretched exponential (SE) fits (gray) decoherence behavior of the molecules used in this study. Experiments were performed at at Q-band and a temperature of 20 K From top to bottom: p_1TAM, d_{18}-TEMPO, TEMPO. The experiments were performed in 1:1 (w:w) H_2O:glycerol.

illaries containing these samples exploded under freezing conditions, upon storage at −80°C, or while loading the samples into the spectrometer. While there is no compelling evidence for the presence of a glass transition point in 40% glycerol solutions,[51] there is also no thorough investigation of glycerol–water mixture glass transitions at cryogenic temperatures to my knowledge. This is a potentially interesting question for understanding the interaction of cryoprotectant concentration, glass quality, and prevention of aggregation at cryogenic temperatures.

2.3.2 Temperature series

To eliminate the interference of a relaxation mechanism other than nuclear-spin-driven electron spin decoherence, Hahn echo decays were measured on the three samples at 20 K (**Figure 2.6**). In all cases, the coherence decays occur on a similar timescale and coherence

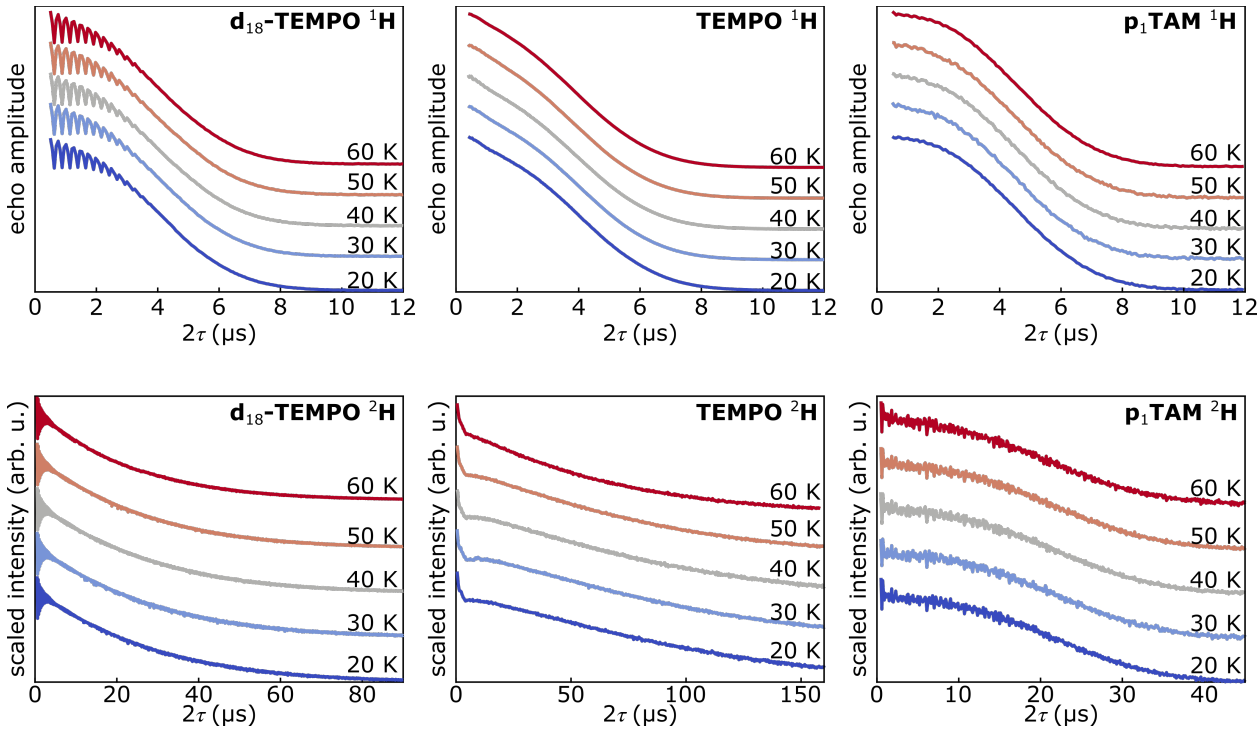

Figure 2.7: Temperature series of echo decays in matricies of 1:1 (w:w) H_2O and glycerol (top) and D_2O (bottom). The d_{18}-TEMPO measurements are in the left column. The TEMPO measurements are in the center column. The p_1TAM measurements are shown in the right column.

is completely lost within 12 μs. These decays can be fit well by a phenomenological fit using a stretched exponential (shown in gray) of the form shown in Equation 2.1. In this equation T_M is the phase memory time and x is a stretching exponent. This stretched exponential form is predicted by the semi-classical description of nuclear spin diffusion that uses stochastic nuclear flip-flops to describe the loss of electron spin coherence.[41,42]

A temperature series from 20 K to 60 K was taken in steps of 10 K for the three organic radicals investigated. The high-temperature limit was based on the temperature below which methyl rotation is no longer considered a major contributor to electron spin dephasing (**Figure 2.7**).[39,40] There is effectively no temperature dependence upon the decoherence

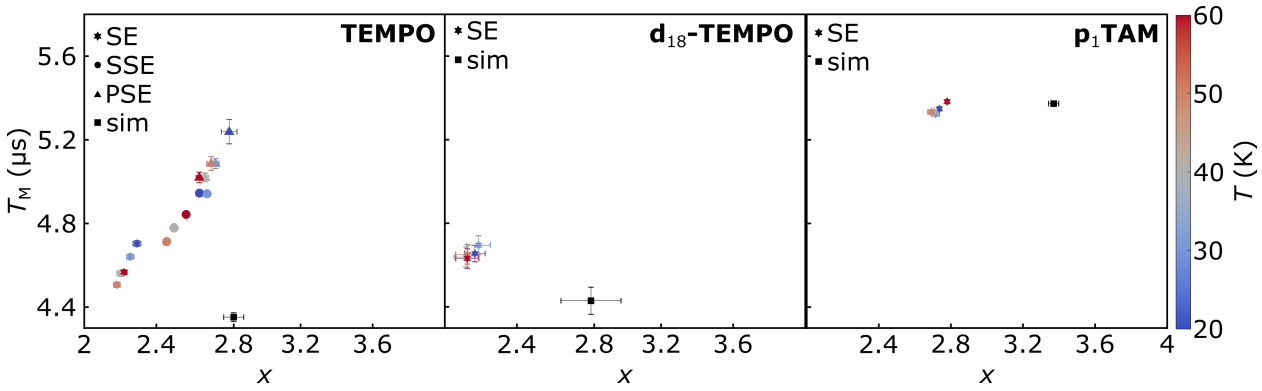

Figure 2.8: x vs. T_{M} plot for the fits of the protonated matrix samples. The stretched exponential is shown in stars, the sum of stretched exponentials are circles, and the product of stretched exponentials are triangles. The color corresponds to the experimental temperature where blue is 20 K and red is 60 K. The simulated parameters were extracted from fitting a stretched exponential to the simulation and are shown in black.

behavior over the range of temperatures investigated, which is consistent with previous experimental results.[39]

The h_{18}-TEMPO data did not produce a simple single stretched exponential, even though instantaneous diffusion is negligible at 200 µM for protonated samples. We checked for instantaneous diffusion by using softer (that is lower flip-angle) pulses, but the fits still yielded a two-component shape for the echo decay experiment. We decided to take a phenomenological approach and fit the data with a sum (SSE) and a product (PSE) of stretched exponentials:

$$V_{\mathrm{SSE}}(2\tau) = V_{0,\mathrm{NSD}} \cdot \exp\{-(2\tau/T_{\mathrm{M}})^{x_{\mathrm{NSD}}}\} + V_{0,\mathrm{other}} \cdot \exp\{-(2\tau/T_{\mathrm{M}})^{x_{\mathrm{other}}}\} \tag{2.3}$$

$$V_{\mathrm{PSE}}(2\tau) = V_{0} \cdot \exp\{-(2\tau/T_{\mathrm{M}})^{x_{\mathrm{NSD}}}\} \cdot \exp\{-((2\tau)/T_{\mathrm{M}})^{x_{\mathrm{other}}}\} \tag{2.4}$$

Both of these approaches to fitting the experimental decays attempt to account for the presence of two different decay mechanisms. There is literature precedence for using a SSE

to fit Hahn echo decays.[59] This approach assumes that different electron spins relax via different mechanisms. The PSE approach is appropriate in the event that electron spins decohere by two independent, yet simultaneous, mechanisms.

Figure 2.8 shows the temperature dependence of the fitting values of the phase memory time T_M and stretching exponent x extracted from using a SE (stars), SSE (circles), and PSE (triangles) of the experimental traces. The fitting values of a SE to the simulation are also shown in black. As the experimental TEMPO data needed a second component to properly reproduce the experimental echo decay shape, the stretching exponents and phase memory times of the nuclear-spin-driven decoherence fits were used (i.e. the fit values that were closer to the simulation's fit values were chosen), as a function of temperature. There is little to no temperature dependence on the behavior of these systems. Neither the stretching factors nor the phase memory times vary significantly over the temperatures investigated. While there are small variations observed in the TEMPO fit values, these likely arise from the dynamics of the methyl groups.

To further test the theory, we extended the measurements to d_{18}-TEMPO in 1:1 (w:w) D_2O:d_8-glycerol. Unfortunately, because we were aiming for internal consistency across experiments, we initially chose to perform the d_{18}-TEMPO in D_2O measurement with a concentration of 200 μM. This choice was unfortunate because instantaneous diffusion is a much stronger effect in deuterated matrices than it is in protonated matrices. We were able to fit the experimental data with a SSE and a PSE, although both components of the SSE were more consistent across the temperature range studied than they were for the PSE. The second component of the SSE fit matched instantaneous diffusion and accounted for approximately 80% of the experimental amplitude. Excitingly, however, the SSE parameters matched the simulated parameters well. This indicates that it is possible to calculate instantaneous diffusion's contribution to electron dephasing and sum it with NSD's contribution to simulate the full echo decay.

We performed an additional validation of the theory using a trityl radical, p_1TAM (**Figure**

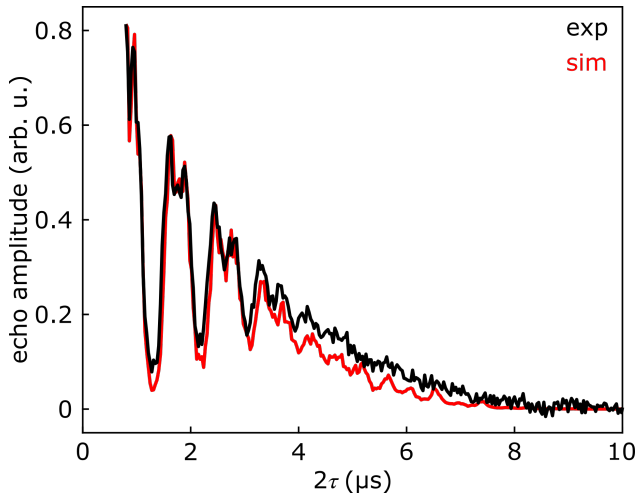

Figure 2.9: Experimental (black) X-band echo decay of 10 μM d_{18}-TEMPO in 1:1 (w:w) H_2O:glycerol and the corresponding MD/CCE model simulation (red). Decays were scaled to the same amplitude at $2\tau = 400$ns.

2.2).[46,60] This structure was of interest, as the methyl groups have more spatial separation from the radical than they do in the TEMPO. The concentrations of the p_1TAM samples were unknown due to solubility issues. Again, we found a nearly perfect stretched exponential for p_1TAM in 1:1 (w:w) H_2O:glycerol. Unfortunately, we again saw a two-component system, and again, one component could be explained by instantaneous diffusion and the other matched the simulation.

2.3.3 X-band echo decays

To validate the efficacy of the simulation method used on the Q-band samples at other frequencies, a sample of 10 μM d_{18}-TEMPO in 1:1 (w:w) H_2O:glycerol at X-band (ca. 9.6 GHz). The good match between the experimental echo decay and the simulation (**Figure 2.9**) demonstrates that the model accurately predicts decoherence behavior at multiple magnetic field strengths.

2.3.4 Deuteration series

As many biological EPR studies are done in a deuterated matrix, we investigated the effect of sample matrix conditions on the decoherence behavior of organic radicals, bulk matrix deuteration was investigated. The samples were mixtures of 5 μM d_{18}-TEMPO in (1:1) H_2O:glycerol and D_2O:d_8-glycerol that ranged from 0% to 100% bulk detueration. These samples will be referred to as the bulk samples for the remainder of this chapter. As is evident in **Figure 2.10**, there is not a large effect of bulk matrix deuteration on phase memory time before approximately 90% bulk deuteration is reached. There is a sharp uptick in the phase memory time by small changes in bulk matrix deuteration above 95% bulk deuteration.

As most biological samples are protonated in a deuterated matrix, an investigation of the deuteration of exchangeable and non-exchangeable hydrons was performed. These samples were 5 μM d_{18}-TEMPO in mixtures of either D_2O, d_5-glycerol, and d_8-glycerol (exchangeables) or D_2O, d_3-glycerol, and d_8-glycerol (nonexchangeables). The simulations predict that deuteration of the exchangeables will increase the phase memory time relative to the bulk samples and that deuteration of the nonexchangeables will decrease the phase memory time relative to the bulk samples, even at the same overall bulk matrix deuteration. This trend is observed experimentally, although to a lesser extent than is predicted by the simulations (**Figure 2.10**). The differences between the exchangeable and nonexchangeable data make sense as nuclear-spin-driven electron spin decoherence arises from pairs of coupled nuclei. The hydrons that are deuterated in the exchangeable samples are closer in proximity, and thus have a stronger coupling, than those in the nonexchangeable samples.

2.3.5 Doubly labeled proteins

Figure 2.11 shows the extracted phase memory times of three different sets of site pairs on maltose binding protein (MBP) in a 1:1 (w:w) deuterated buffer and d_8-glycerol matrix. The site pairs are D41X/S238X, S211X/T345X, and S238X/T345X, where X indicates the spin label side chains: R1, R7, V1, M1, and I1 (**Figure** 3.1. Details about the samples

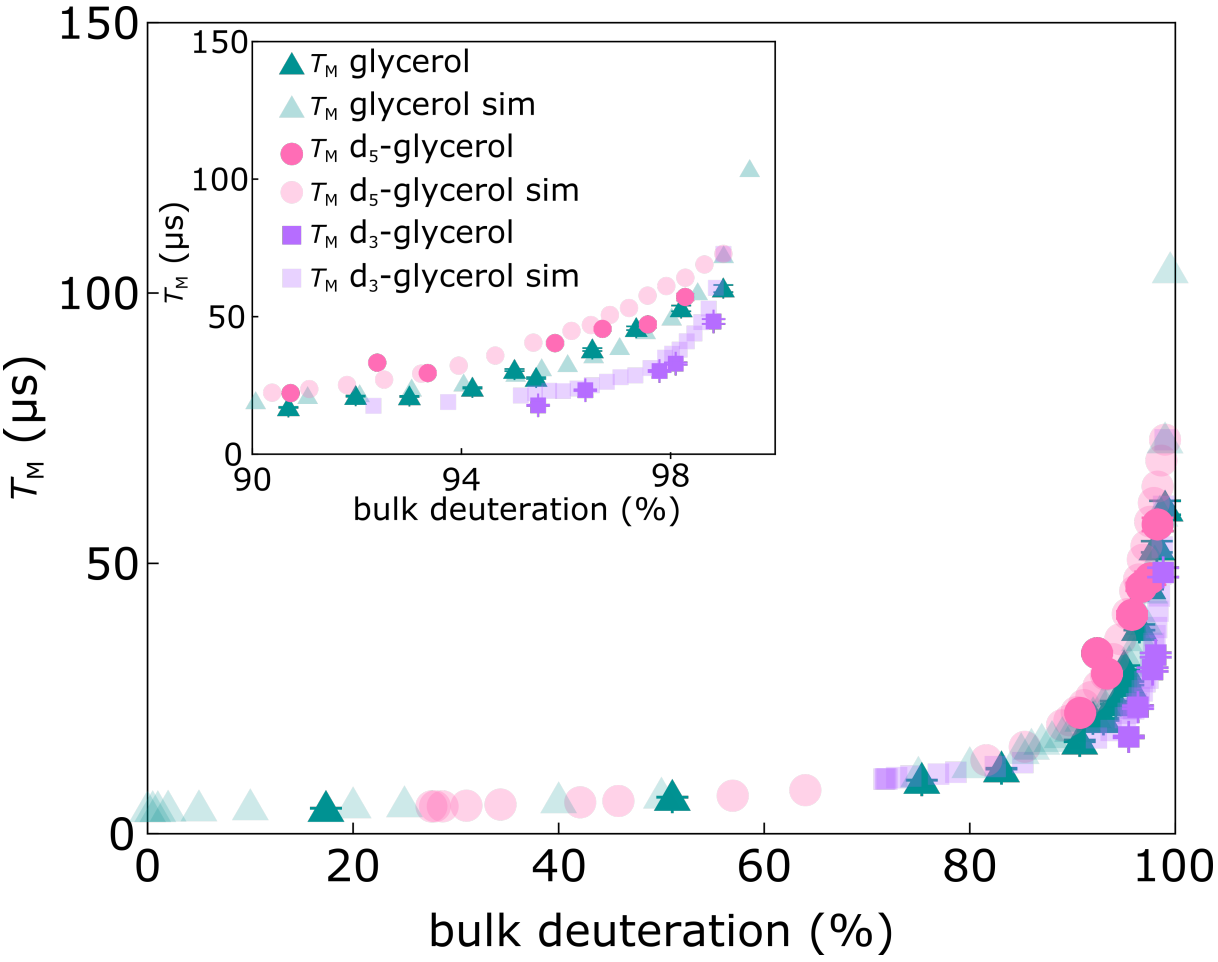

Figure 2.10: Deuteration series. The full range of bulk deuteration for the exchangeable hydron samples (circles), the bulk deuteration samples (triangles), and the nonexchangeable hydron samples (squares). Inset, a zoom-in looking at the phase memory times for samples with 90-100% bulk deuteration. The vertical axes ranges of the main figure and inset are the same. The horizontal axis of the inset is also bulk detueration (%).

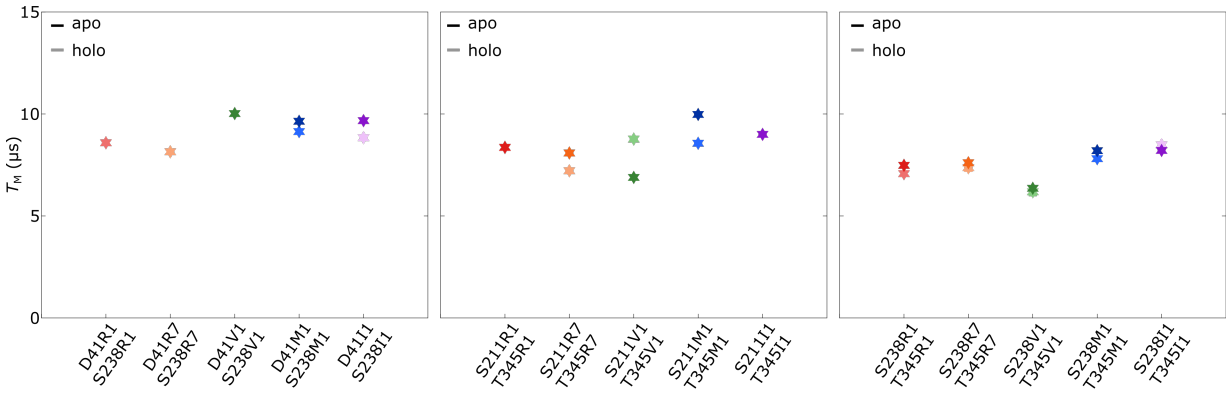

Figure 2.11: Comparison of T_M values with different spin labels at the same site pairs on maltose binding protein. R1 is shown in red, R7 is shown in orange, V1 is shown in green, M1 is shown in blue, and I1 is shown in purple. The darker colors are the apo T_M values and the lighter colors are the holo T_M values. The protein concentration was ca. 50 µM in a 1:1 (w:w) buffer of deuterated DEER buffer (see Appendix 5) and d_8-glycerol.

are discussed in **Chapter 3**. These experiments were chosen to demonstrate that at 50 K, there are not significant differences in the phase memory time amongst the five spin labels, although generally the M1 and I1 sidechains demonstrate slightly longer (on the order of hundreds of nanoseconds to a few microseconds) phase memory times than the R1 and R7 sidechains, which can be attributed to the added distance from the proton-dense protein sidechain of the proxyl spin labels relative to the methanesulfonothioate spin labels. The lack of large variance in phase memory time is consistent with the deuteration matrix predictions. One might expect the different steric hindrances of the spin labels to contribute to the local micro-environment and contribute differently to the electron spin relaxation. As we have seen above, however, unless the bulk system is more than about 90% deuterated, the contribution of the local environment to phase memory time is negligible (**Figure 2.11**).

2.4 Conclusions

This chapter presented both experimental and theoretical investigations into nuclear-spin-driven electron spin decoherence. First, a quantum calculation method that begins with a simple molecular structure was used to quantitatively predict phase memory times of organic radicals in solution. In combination with the experimentally validated simulations, the ability to examine decoherence effects due to individual nuclei greatly enhances insight into the structural origins of nuclear-spin-driven electron spin decoherence. As mentioned, this decoherence mechanism has traditionally been described semi-classically by a stochastic process of nuclear flip-flops involving pairs of surrounding nuclei, with an *ad hoc* flip-rate constant. Within the quantum model presented herein, however, electron spin decoherence is the result of a coherent, deterministic evolution of a large ensemble of nuclear spins coupled to each other and to the electron spin.

Next, this predictive work was extended to phase memory times of an organic radical in matrices of varying deuteration concentrations. The quantitative models, in concert with the experimental validation, provide strong evidence for the importance of matrix deuteration. Furthermore, it is possible to separate out the contributions of exchangeable versus non-exchangeable deuterons in glycerol. We find that deuteration on d_5-glycerol has more impact in increasing phase memory time than deuteration on d_3-glycerol does.

The findings that greater than 90% bulk deuteration has the most effect on phase memory time is consistent with what is seen experimentally in a doubly labeled protein sample (**Figure 2.11**). The work outlined in this chapter represents a significant step towards quantitative *in silico* phase memory time predictions.

Chapter 3

BACKING OUT THE BACKBONE: SPIN LABEL CONTRIBUTIONS TO DOUBLE ELECTRON–ELECTRON RESONANCE SPECTROSCOPY

The project presented in this chapter describes a multi-spin label approach to obtain more precise backbone information from the DEER experiment. This work provides a direct comparison of commonly used spin labels. The dataset provided in this chapter will be used for robust validation of *in silico* spin labeling softwares.

3.1 DEER Spectroscopy

From muscle contraction to photosynthesis, protein motion governs life. Understanding protein motion and conformational change is a hugely important and broad area of research. Double electron–electron resonance (DEER) spectroscopy[42,61,62] is one technique for observing conformational change of proteins in native-like environments on a coarse-grain level to sub-ångstrom resolution. Using DEER, it is possible to measure long-range distances (20–80 Å) by measuring the through-space dipolar coupling of two stable radicals on the protein, usually obtained by attaching stable radicals, or spin labels, via site-directed spin labeling (SDSL).[63]

While there are many techniques for probing protein structure and conformational change, DEER is uniquely situated to provide information for systems where other techniques have limited efficacy. DEER is a distinct complement to other structural techniques as it provides a full probability distribution of distances, $P(r)$, which captures the entire conformational landscape of a protein in frozen solution and overall flexibility of the protein structure.[64,65]

The full ensemble $P(r)$ obtained via DEER is particularly advantageous in studying large, flexible proteins and integral membrane proteins, where mapping conformational motion involves probing very small changes, which can have a large effect on system function.[66]

The DEER experiment requires the presence of two (or more) radical centers.[42,61,62] As most proteins lack a native paramagnetic center, the radicals are usually added to the system via site-directed spin labeling (SDSL).[67–69] Nitroxide radical centered spin labels are most commonly used in DEER (**Figure 3.1**) and are attached to a Cys residue at the site of interest on the protein. The spin label binds to the protein backbone via a disulfide bond (R1, R7, V1) or a thioether bond (I1, M1). Before binding to the backbone, the spin labels are called: S-(1-oxyl2,2,5,5-tetramethyl-2,5-dihydro-1H-pyrrol-3-yl)methyl methanesulfonothioate (MTSL); 4-bromo-(1-oxy-2,2,5,5-tetramethylpyrroline-3-methyl) methanethiosulfonate (BrMTSL); bis-(2,2,5,5-tetramethyl-3-imidazoline-1-oxyl-4-il)disulfide (IDSL);[60,70] 3-(2-iodoacetamido)-2,2,5,5-tetramethyl-1-pyrrolidinyloxy (IAP);[71] and 3-maleimido-2,2,5,5-tetramethyl-1-pyrrolidinyloxy (MAP).[72] The most commonly used spin label is MTSL (sometimes called MTSSL).[73] There has also been much effort focused on synthesizing metal-centered spin labels, particularly with Gd and Cu,[74–76] as well as on labels for *in vivo* studies.[46]

As is evident in **Figure 3.1**, commonly used spin labels have several rotatable bonds. The extracted distance is not the desired backbone $C_\beta - C_\beta$ distance, but the nitroxide–nitroxide distance. This is a combination of the protein's flexibility as well as the flexibility of the spin label. Therefore, for structural biologists to extract reliable backbone information from DEER experiments, they must include both protein and spin label dynamics in their structural models. While much work has been done on investigating the contributions of spin labels to the shape of the $P(r)$ extracted from the DEER experiment, it has primarily been *in silicio* work modeling possible spin label rotamers with crystal structures.[77–81]

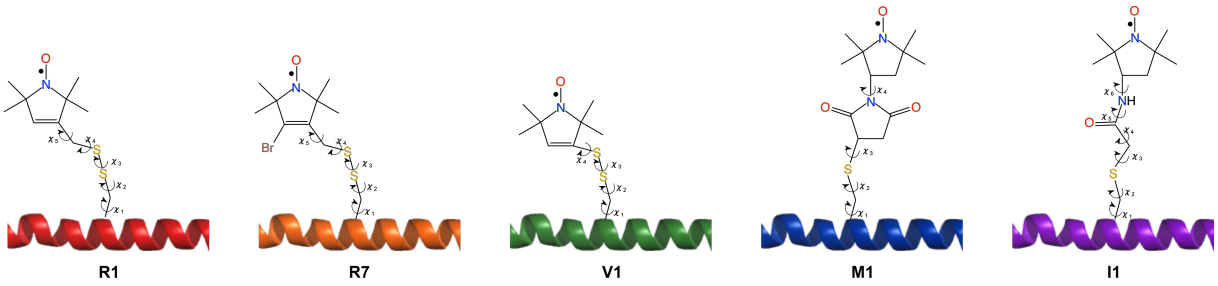

Figure 3.1: Nitroxide spin labels used in this thesis work bound to a fraction of an α helix (PBDID: 1KQL). From left to right R1 (MTSL), R7 (Br-MTSL), V1 (IDSL), M1 (MAP), I1 (IAP).

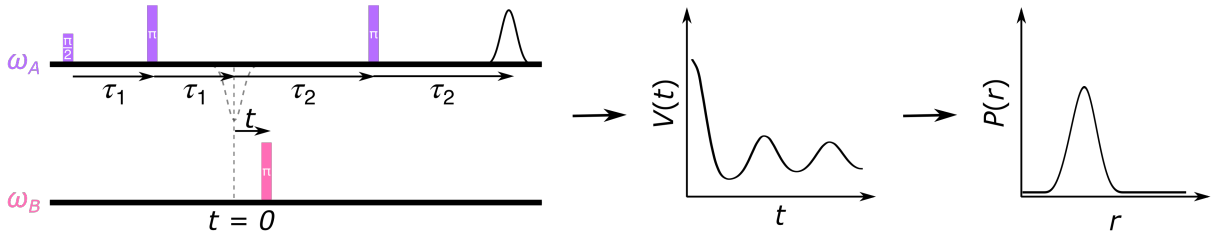

Figure 3.2: The DEER experiment. Left, the four-pulse DEER sequence, with a pulse sequence of $\pi/2 - \tau_1 - \pi - \tau_1 + \tau_2 -$ echo at the observer frequency ω_{A} (purple) and a pump π pulse with frequency ω_{B} (pink) applied at time $\tau_1 + t$ after the first π observer pulse is applied. Center, the time domain oscillatory DEER signal. Right, the extracted $P(r)$ from the DEER simulation.

3.1.1 Origins of the DEER Signal

The DEER $P(r)$ arises from the through-space dipolar coupling of two stable radical centers that have been attached to the chosen protein sites.[42,67] The strength of this interaction is proportional to $1/r^3$, and is probed by placing the spin labeled protein in an external magnetic field, B_0, and applying microwave pulses at an observer frequency, ω_A, and a pump frequency, ω_B. The change in the local magnetic field experienced by the observer spins upon a change of the magnetic moment of the pump spins is recorded by varying the time at which the pump pulse is applied and recording the integrated echo intensity. This produces an oscillatory time-domain signal with information about the full ensemble of distances encoded into the oscillations. As the process by which the conversion must be done is ill-posed mathematically, the time domain signal must be converted to the distance domain by numerical methods. This is most commonly done by utilizing Tikhonov regularization,[82,83] although this is still a major field of study.[84,85]

While there are several different pulse sequences used in DEER, the most common is the four-pulse DEER sequence (**Figure 3.2**).[86,87] The magnetic moments of the spins are initially aligned with the external magnetic field (conventionally the z-direction). Upon the application of a $\pi/2$ pulse at the observer frequency, ω_A, the magnetic moments of the spins are knocked down into the xy-plane. They precess in the xy-plane for a time τ_1, at which, a π pulse at ω_A is applied causing an inversion of the the magnetic moment vectors in the xy-plane. Due to the inversion in the xy-plane, those with the highest precession frequency will catch up to those with the lowest precession frequency at time τ_1. Then at time $\tau_1 + t$, the pump π pulse is applied at the pump frequency ω_B. This inversion of the pump magnetic moment vectors causes a change in the precession frequency of the observer spins. The observer magnetic moments precess for time $\tau_2 - t$ after the pump pulse, at which point the final refocusing π pulse is applied at ω_A. After time τ_2 the echo amplitude is integrated over its full width at half maximum (FWHM) of the echo and is recorded.[88]

The change in the local magnetic field experienced by the observer spins is tied to the

magnitude of the through-space dipolar coupling and is measured as the integrated spin echo as a function of the time at which the pump pulse is applied.[2] Since there are, however, many spin labeled proteins near each other, the experimental time-domain signal, $V(t)$, is a product of the intramolecular distances, in this work called the foreground signal $V_{\text{intra}}(t)$, and the intermolecular distances, which is referred herein as the background signal $V_{\text{inter}}(t)$:[42,87,89]

$$V(t) = V_0 \cdot V_{\text{intra}}(t) \cdot V_{\text{inter}}(t) \tag{3.1}$$

where V_0 is the unmodulated echo intensity. The background signal takes the form of a rather simple stretched exponential decay function

$$V_{\text{inter}} = \exp(-k|t|^{\ D/3}) \tag{3.2}$$

in which D is the dimensionality of the system, which for the cases outlined in this work, will always be 3; k is a decay rate with units of μs^{-1} (provided $D = 3$); and t is the time at which the pump pulse is applied after the first observer π pulse. Understanding and isolating the background is an active field of research.[82–84,90] There is also new evidence for an additional phase factor in DEER experiments for systems with significant spin polarization,[91] but those cases are outside the scope of this work.

The foreground signal is rather more complicated than the background signal and arises from the efficiency of the pump pulse, λ, and the intramolecular dipolar modulation function, $S(t)$:

$$V_{\text{intra}} = (1 - \lambda) + \lambda \cdot S(t) \tag{3.3}$$

Since λ describes the efficiency of the pump pulse at flipping the pump spins, it must take a value such that $0 \leq \lambda \leq 1$. For A–B spin pairs with $S = 1/2$ in a glass or powder, the intramolecular dipolar modulation function is described by the integral of the dipolar kernel, which is dependent on the intramolecular spin distance r and the timing of the pump pulse t, and the probability distribution $P(r)$:

$$S(t) = \int_0^\infty \mathrm{d}r \cdot K(t,r) \cdot P(r) \tag{3.4}$$

The dipolar kernel $K(t,r)$ relates the distance distribution to the evolution of dipolar coupling for all spins:

$$K(t,r) = \int_0^{\pi/2} \mathrm{d}\theta \cdot \cos[(1 - 3 \cdot \cos^2\theta) \cdot \omega_\perp(r) \cdot t] \tag{3.5}$$

The angle between the external magnetic field and the inter-spin distance vector r is θ. The perpendicular dipolar angular frequency $\omega_\perp(r)$ is given by:

$$\omega_\perp = \frac{\mu_0}{4\pi} \cdot \frac{\mu_\mathrm{B}^2}{\hbar} \cdot \frac{g_\mathrm{A} g_\mathrm{B}}{r^3} \tag{3.6}$$

There are a few important takeaways from **Equation 3.6**. First, $\omega_\perp$ is described by the g-factors of the A and B spins and it is proportional to $1/r^3$. Second, it is the $1/r^3$ dependence that makes it possible to measure longer distances with DEER than with other techniques like nuclear Overhauser effect NMR and Förster resonance energy transfer (FRET), where the distance dependence is proportional to $1/r^6$,[92,93] thus the signal decays faster than it does in DEER. Third, the frequency of the oscillation is proportional to the inverse cube of the distance between the A and B spins, $g_\mathrm{A}, g_\mathrm{B}$; for a large distance r the frequency of $\omega_\perp$ will be relatively slow, and for a small distance r the frequency of $\omega_\perp$ will be fast.

Equation 3.5 includes the cosine and sine Fresnel integrals $C(z)$ and $S(z)$, such that **Equation 3.5** simplifies to:

$$K(t,r) = \frac{C(z)}{z} \cdot \cos(\omega_\perp t) + \frac{S(z)}{z} \cdot \sin(\omega_\perp t) \tag{3.7}$$

where $z = \sqrt{6\omega_\perp t/\pi}$.

From a practical standpoint, it is possible to estimate the inter-spin distance simply by the frequency of the oscillations in the time domain DEER experiment. Consider an example where two spin labels are attached to a protein, the pump spin (B spin) has a $\omega_\mathrm{B} = 34.565$ GHz while the probe spin (A spin) has a $\omega_\mathrm{A} = 34.500$ GHz. After the application of the π

pump pulse, there is a resulting 2 MHz shift in ω_B of the probe spin making $\omega_B = 34.502$ GHz. From the relationship outlined in **Equation 3.6** and substituting in numerical values for the physical constants, we are able to get

$$r = \sqrt[3]{\frac{52}{\omega_\perp}\frac{1}{2\pi}} \tag{3.8}$$

where r is the inter-spin distance in nm, and $\omega_\perp$ is in units of MHz. Plugging in the 2 MHz shift in $\omega_\perp$ for this example corresponds to a 2.96 nm inter-spin distance.

Now, returning to the discussion from above.

Since the experiment is discretized in the time domain, the discretized form of **Equation 3.4** is

$$\boldsymbol{S} = \boldsymbol{K}\boldsymbol{P} \tag{3.9}$$

where $\boldsymbol{K}$ is an $n \times m$ matrix and $\boldsymbol{S}$ and $\boldsymbol{P}$ are both vectors of dimension $n \times 1$ and $m \times 1$, respectively. Unfortunately, solving the inverse of **Equation 3.9** for $\boldsymbol{P}$ is ill-posed numerically and requires the employment of a numerical regularization method. There has been much work on finding the best solution to this ill-posed problem. Tikhonov regularization is most commonly utilized and the details about the selection of the regularization parameter in Tikhonov have been explored.[64,82–85,94]

3.1.2 Experimental Considerations for the DEER Experiment

This subsection will outline some of the major experimental considerations for performing DEER. A more complete discussion of experimental considerations can be found in the forthcoming DEER white paper.

The first, and perhaps most important, consideration for performing DEER is the protein of interest itself. As the most common spin labels bind to the protein backbone through disulfide or thioether bonds, the presence of a large number of solvent-exposed Cys residues will cause difficulties in spin labeling sites of interest. If there are a large number of solvent-exposed Cys residues, this hurdle can be overcome by replacing the native solvent-exposed

Cys residues with Ser or Ala residues.[69] Another way around dealing with solvent-exposed Cys residues is to use non-canonical amino acids with spin labels, such as TOAC.[95–97]

Following protein selection is site pair selection. For most DEER experiments, the accessible distance measurement range is approximately 15-60 Å.[98] The current record for longest recorded distance by DEER is 160 Å,[99] although this was done on a protein expressed in fully deuterated media, which is a financial barrier for most labs. Thus, the distance distributions of the site pairs of interest should be predicted to fall within the range of 15-60 Å.

In addition to the distance between site pairs, the local environment of sites of interest must be taken into account. If a residue is quite buried and not solvent-exposed, it may not have a high labeling efficiency and may require an extended labeling protocol with a higher molar excess of spin label. Even if it is successfully labeled, it is possible that the bulkiness of the spin label could cause structural perturbations to the protein. To avoid this, an *in silico* spin labeling program such as MMM,[100] ProEPR,[101] or MtsslWizard[78] should be used to model the attachment of the rotamer to a crystal (or cryo-EM or Rosetta-generated) protein structure.[102]

The use of deuterated buffers is highly important for extending the phase memory time T_M, and subsequently maximum measurement distance, of a DEER sample. For a complete description of T_M, see **Subsection 1.2.6** and **Chapter 2**. As seen in the work in this chapter, the difference in phase memory time of a spin label analogue in a matrix that is 1:1 (w:w) water:glycerol will increase approximately 20-fold going from natural-abundance matrix deuteration to use of a perdeuterated matrix.[58]

When performing the experiment, temperature selection is another significant factor to consider. For nitroxide DEER, 50 K is usually an optimal temperature.[98] Higher temperatures shorten T_M and thereby the sensitivity. Lower temperature increase T_1 and thereby the saturation, leading to slower experiments.The advent of cryogen-free cooling systems used with pulse EPR spectrometers makes this temperature more sustainable than using liquid

helium.[103] For those limited to liquid nitrogen, 80–100 K will be sufficiently cool to be able to perform the DEER experiment. The relaxation rate, however, will increase significantly above 80 K due to methyl rotations,[39] which decreases the maximum measurable distance. The temperature will also limit the spin lattice relaxation time T_1 (see **Subsection 1.2.6**) as well as the phase memory time T_M. The length of τ_2 is limited by the phase memory time, thus long phase memory times are critical for measuring long distances.

A final important consideration in the DEER experiment is pulse selection. Historically, rectangular pulses have been most commonly used in DEER, but the advent of arbitrary waveform generators (AWGs) has led to routine pulse shaping. This is because the excitation bandwidth of a shaped pulse is more uniform than that of a rectangular pulse.[104,105] The DEER experiments in this chapter are all performed with Gaussian observer pulses and sech/tanh pump pulses. Gaussian observer pulses have a sharper excitation profile compared to that of rectangular pulses and are shown to increase signal fidelity compared to rectangular pulses, as they reduce the spectral overlap between observer and pump pulse excitation windows.[106]

3.2 Methods

This thesis work fills a gap in the research attempting to model spin label rotamers *in silico* by using various common spin labels (**Figure 3.1**) attached to differing sites on maltose binding protein (MBP) (**Figure 3.3**), with the goal of disentangling protein flexibility from side chain flexibility using a multi-spin label approach. A cartoon representation of the concept of this multi-spin label approach with V1 and R1 is shown in **Figure 3.4**. The general concept is to perform the DEER experiment multiple times using different spin labels on the same site pairs. Since spin labels have different numbers of rotatable bonds and experience different levels of steric hindrance, the extracted distance distributions will be different. Upon combining the experimental results with rotamer modeling software, it should be possible to extract a more precise $C_\beta - C_\beta$ distance. We hypothesized that the

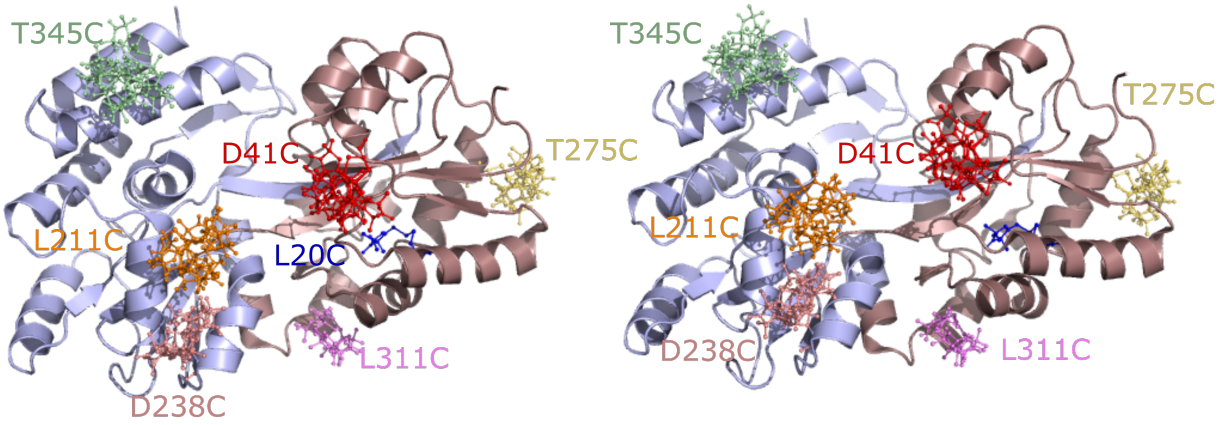

Figure 3.3: Maltose binding protein (MBP) was selected as a benchmark protein due to its stability, ease of growth, lack of native Cys residues, and lack of intermediate states between apo and holo. Left, apo MBP (PDB ID: 1OMP). Right, MBP with bound maltose (PDB ID: 1ANF). Rotamers of R1 are shown for the sites of mutation investigated.

multi-spin label approach would result in simple cases like those outlined in **Figure 3.4**. In the first case, the spin labels preferentially point towards each other. Since I1 has a longer side chain than R1 does, the distance obtained by the I1 measurement is shorter than that of the R1 measurement. In the case where the spin label side chains are pointed parallel to each other, the R1 and I1 peaks will occur at the same distance r. In the event that the spin labels are pointed away from each other, the distance extracted from the R1 experiment will produce a peak at a shorter distance than would be found in the I1 sample. Unfortunately, this picture is too simplistic, and the outcome of the experiments was not quite this straightforward (see **Subsection 3.3.2** and **Appendix 6**).

MBP was chosen as a benchmark protein for this study for several reasons. First, it is known to have two clearly defined conformations. The apo state is open and, upon binding of maltodextrins, the protein closes in a clam-shell or Pac-Man-type fashion, causing a hinge-and-twist motion between the N- and C-terminal domains. These states have been studied

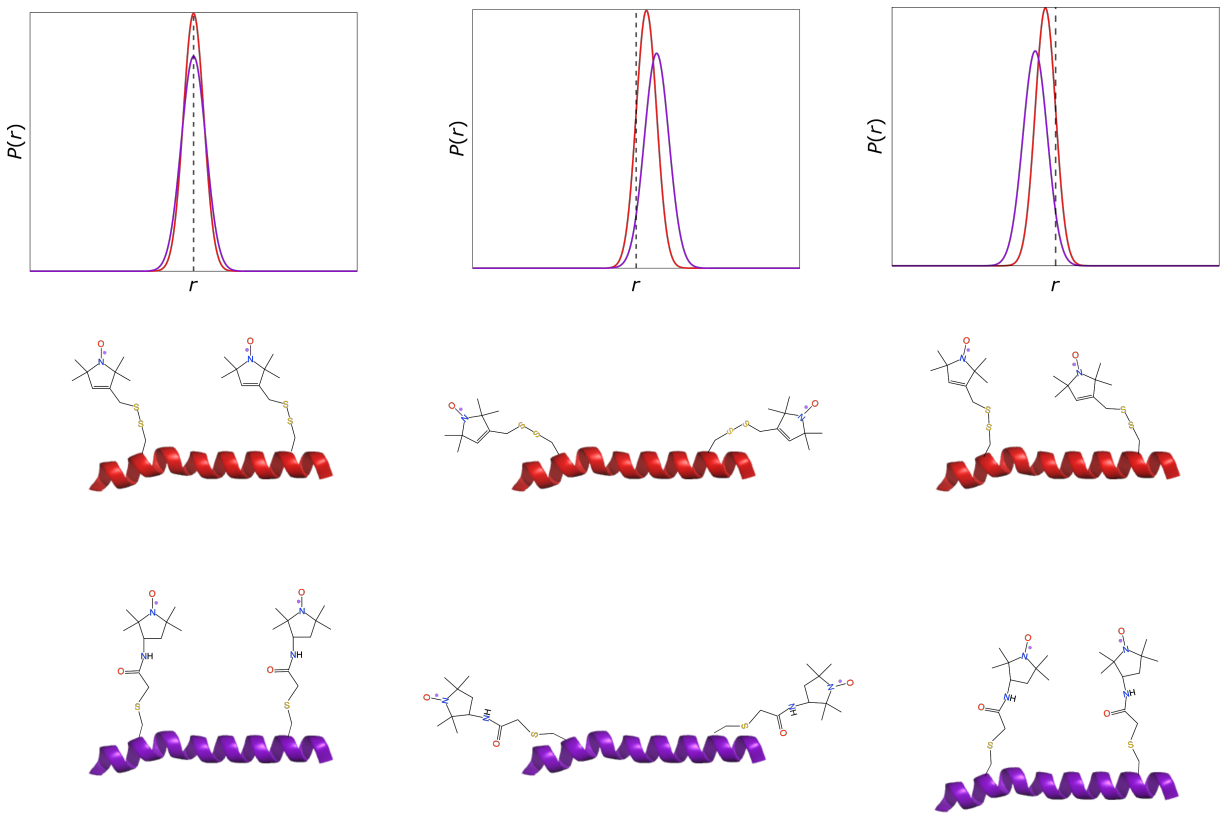

Figure 3.4: Simplified representation of garnering more backbone information by a multi-label strategy, using simulations of the R1 and I1 sidechains. Left, the parallel case: the maxima are located at the same distance, it is probable that the rotamer clouds are perpendicular relative to the C_β. Middle, the long case: the maximum of the R1 distribution occurs at a shorter distance than that of the I1 distribution, indicating the labels are likely pointed away from each other. Right, the short case: the I1 sidechain produces a maximum at a shorter distance than the R1 sidechain does, suggesting the spin labels are pointed in towards each other.

extensively, and a plethora of structures determined by different methods exist.[107–116] Having this type of robust structural characterization is important to act as a benchmark for our experimental results. Second, there are no native Cys residues in MBP. This is significant as the common nitroxide spin labels are attached to the protein backbone via disulfide bonds (R1, R7, V1) or a thioether bond (I1, M1). Thus, we are able to minimize functional and structural perturbations by having only to mutate in Cys resides at the sites of interest, rather than also having to remove native Cys residues. Finally, the ease of expression of MBP makes it an excellent protein for generating a large number of samples.

In order to select sites for mutagenesis, the crystal structures of apo and holo (maltose bound) MBP,[110] PDB IDs 1OMP and 1ANF, respectively, were used in the spin label rotamer simulation software MMM.[100] All residues on both structures of MBP were tested for labeling using MMM and all site pairs were selected that show distances in the range of 15–60 Å apart in both crystal structures and were not involved in ligand binding. From these results a set of 15 site pairs (**Figure 3.5**) were selected to encompass a variety of different distances, change in distance between apo and holo, and secondary structure.

To perform mutagenesis, WT MBP DNA in the pETM-11 vector was used. The general method for site-directed mutagenesis used in this work was based on the method outline by Liu and Naismith.[117] The forward and reverse primers were designed to overlap on their 5' ends with a melting temperature of approximately 45 °C. The 3' non-overlapping regions were designed to have a melting temperature that was 5–10 °C warmer than that of the overlapping regions. Primers were purchased from Integrated DNA Technologies. The PCR was carried out using a HF Phusion polymerase kit (New England Biolabs) with a modified hot start approach. In this method, all reagents except the polymerase are added to the tube and are heated at 95 °C for 5 minutes before the addition of the polymerase.

The PCR product was checked for amplification with agarose gel electrophoresis, and upon successful amplification was transformed into Turbo *E. coli* cells (New England Biolabs) in a 2 mL Eppendorf tube to ensure sufficent aeration. After mixing the PCR product into

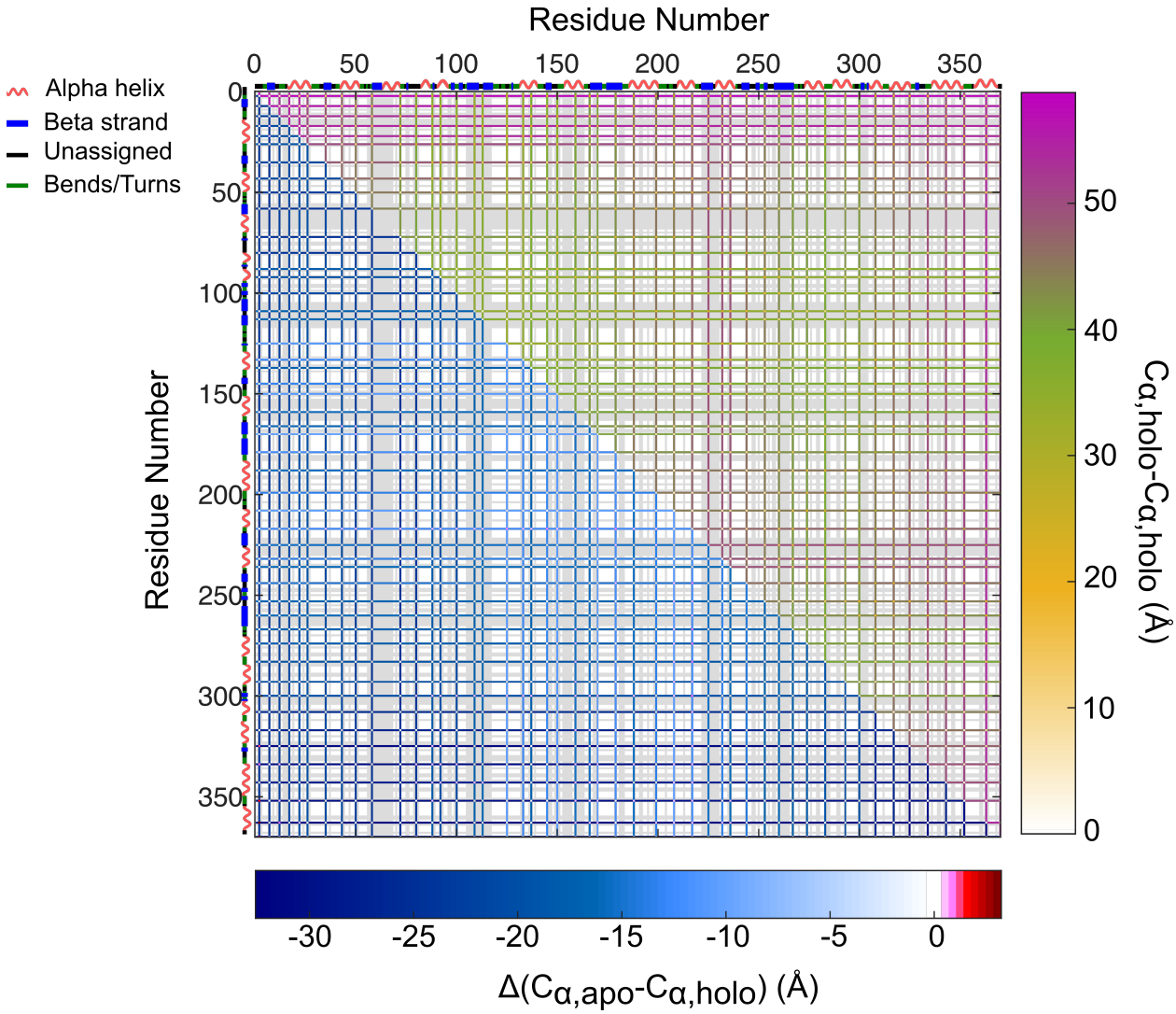

Figure 3.5: Conformational change grid. The top and left axes show residue number. The markings along the left and top axes show the local secondary structure, with alpha helices indicated as red squiggles, beta sheets are shown in blue lines, bends/turns in green, and unassigned features in black. Gray indicates site-pairs that are unsuitable for DEER. The bottom half of the plot shows the distance change of the C_α between apo and holo states, with dark blue indicating getting closer together and dark red indicating getting further apart. The top half of the plot shows the holo C_α−C_α distance between residues.

the Turbo cells, the two were incubated on ice for 30 minutes and then heat shocked in a water bath for 30 seconds at 42 °C. The cells were left to rest on ice for 5 minutes before the addition of 200 μL of Super Optimal broth with Catabolite repression (SOC) outgrowth media. The cell outgrowth was performed for 1-2 hours at 37 °C, shaking at 250 rpm. The incubation was then applied to a Lysogeny broth (LB) kanamycin plate and left overnight for colony growth at 37 °C in the incubator.

The protein was purified according to a standard protocol for His-tagged proteins[118] and purity was confirmed via sodium dodecyl sulfate–polyacrylamide (SDS PAGE) electrophoresis. Specifically, purification was conducted using a Ni-NTA (nitrilotriacetic acid) affinity gravity column. Full details of the purification, including buffers, can be found in **Appendix 5**. To minimize intermolecular disulfide crosslinking, the elution was carried out in a large volume ($\geq$ 20 mL). Spin labels were added at 10 fold excess relative to the protein concentration. The incubation of spin label and protein was carried out overnight at 4 °C. The excess spin label was removed by repeated concentration and dilution steps in a spin concentrator (molecular weight cutoff 20 kDa). After 5 concentration-dilution steps, the protein was checked for unbound spin label using CW EPR spectroscopy. All CW experiments were conducted at X-band (ca. 9.7 GHz) on a Bruker EMX spectrometer equipped with a dielectric resonator at room temperature. If excess spin label was found on the CW spectrum, additional concentration-dilution steps were performed until the CW EPR spectrum showed minimal unbound spin label. Finally, the protein was exchanged into a deuterated buffer with 50% d_8-glycerol (%w) to prevent aggregation, transferred by syringe into a 1.1 mm ID (1.5 mm OD) quartz capillary tube (Wilmad Labglass), flash frozen in liquid nitrogen, and stored at -80 °C until measurement.

DEER measurements were performed at ca. 34 GHz and 50 K in a Bruker EleXsys E580 EPR spectrometer, in a MD2 resonator, equipped with a SpinJet AWG, a 390 W TWT (Applied Systems Engineering), and a cryogenfree cooling system (ColdEdge). DEER experiments were all performed with 60 ns Gaussian observer pulses (truncation parameter 0.1), with

power amplitudes corresponding to $\pi/2$ and π flip angles, and a 150 ns sech/tanh pump pulse. DEER data was analyzed using DeerLab 0.13.1.[84] Simulations were done using the crystal structures for apo (1OMP)[108] and holo (1ANF)[108] MBP, and the *in silico* spin labeling programs MMM,[100] MtsslWizard,[78] and ProEPR.[101]

3.3 Results

3.3.1 CW EPR

The CW experiments were performed as a check for unbound spin label on both apo and holo MBP (**Figure 3.6**). This is an important step in preparing DEER samples since a large amount of free spin label results in a steep contribution to the background.

A noticeable trend in this dataset across apo and holo protein is that V1 has a tendency to have unbound spin label. There has been previous literature demonstrating that the V1 side chain is susceptible to degradation to thiocystine (major product) and cysteine (minor product) at room temperature.[119] This is consistent with experimental V1 data collected on apo S238V1 L275V1 at room temperature upon labeling and after 17 hours at room temperature (**Figure 3.7**). The sharp, narrow peaks seen on the 17-hour sample arise from free spin label, which tumbles quickly enough to average out anisotropy in the system. This is not inherently a deal-breaker for the use of the V1 sidechain, but it is important to consider the unbound spin concentration before performing DEER. As the background decay rate is dependent on the concentration of paramagnetic centers, a large fraction of unbound spin will cause a steep background decay. Also, a large concentration of unbound spin label reduces the DEER modulation depth, and therefore the sensitivity, since there are fewer doubly-labeled proteins.

3.3.2 DEER Spectroscopy

Figure 3.8 shows the experimental DEER traces. The V1 sidechain tends to produce lower modulation depths than the other sidechains because of its tendency to fall off the protein

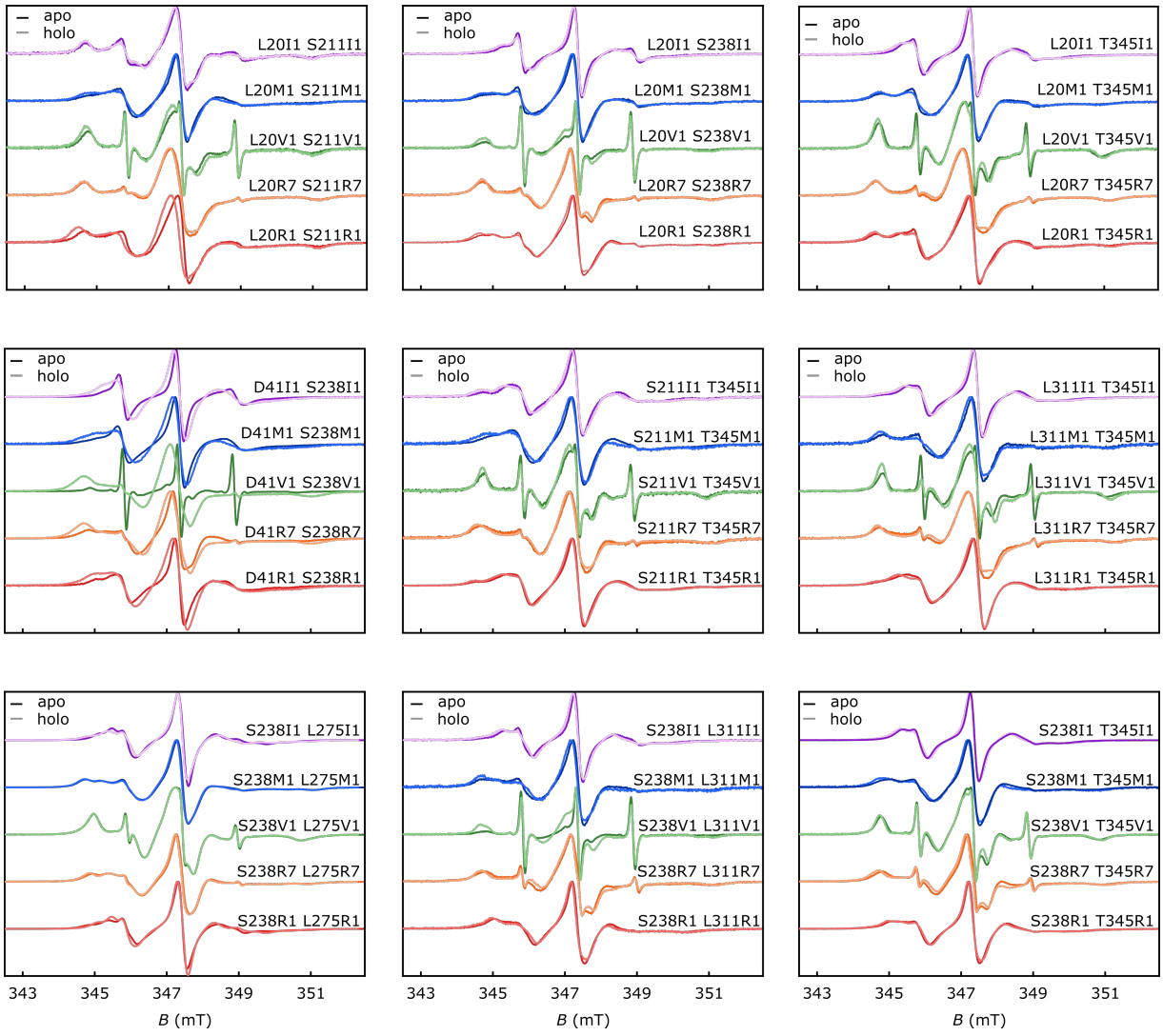

Figure 3.6: Room temperature CW EPR data of apo (dark) and holo (maltose bound) (light) MBP. R1 is shown in red, R7 is shown in orange, V1 is shown in green, M1 is shown in blue, I1 is shown in purple. The samples were on the order of 100 μM protein (200 μM spin).

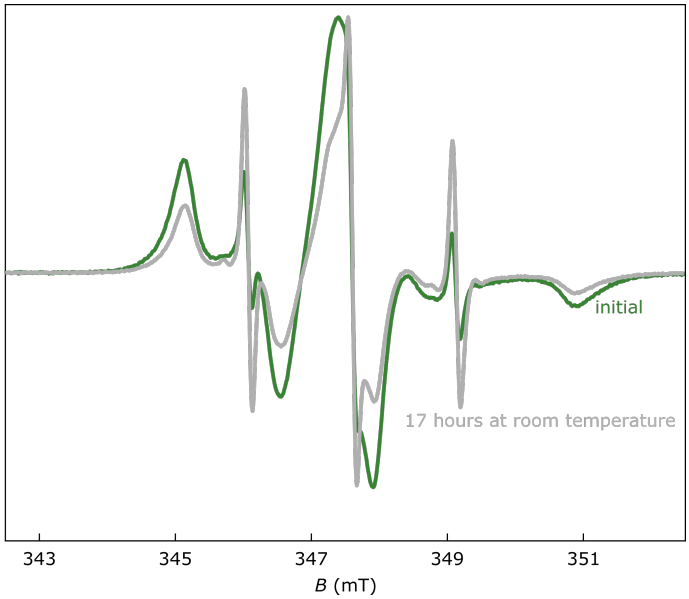

Figure 3.7: X-band CW spectra of holo S238V1 L275V1 immediately after labeling and purification (green) and the same sample after 17 hours at room temperature (gray).

backbone. There are instances, such as L20I1 S211I1, in which the I1 sidechains produce very shallow modulation depths. As L20C is a buried residue, the bulky size of the I1 sidechain will encounter difficulties with labeling. Thus, it is likely that there is very low labeling efficiency for L20I1.

Figure 3.10 shows the ProEPR simulations in black and the 95% confidence intervals for the experimental distance distributions and their background fits in the same colors as previous figures. There are a few notable trends. First, models of I1 and M1 sidechains consistently predict a narrower rotamer distribution than is seen experimentally. Additionally, there appears to be a consistent trend of the R1 model to predict a shorter distance than is experimentally observed. These trends are also shown in **Figure 3.10** with the holo experimental simulations shown in gray.

Unfortunately, there is not a clear trend as described in **Figure 3.4**. This is because rotamers

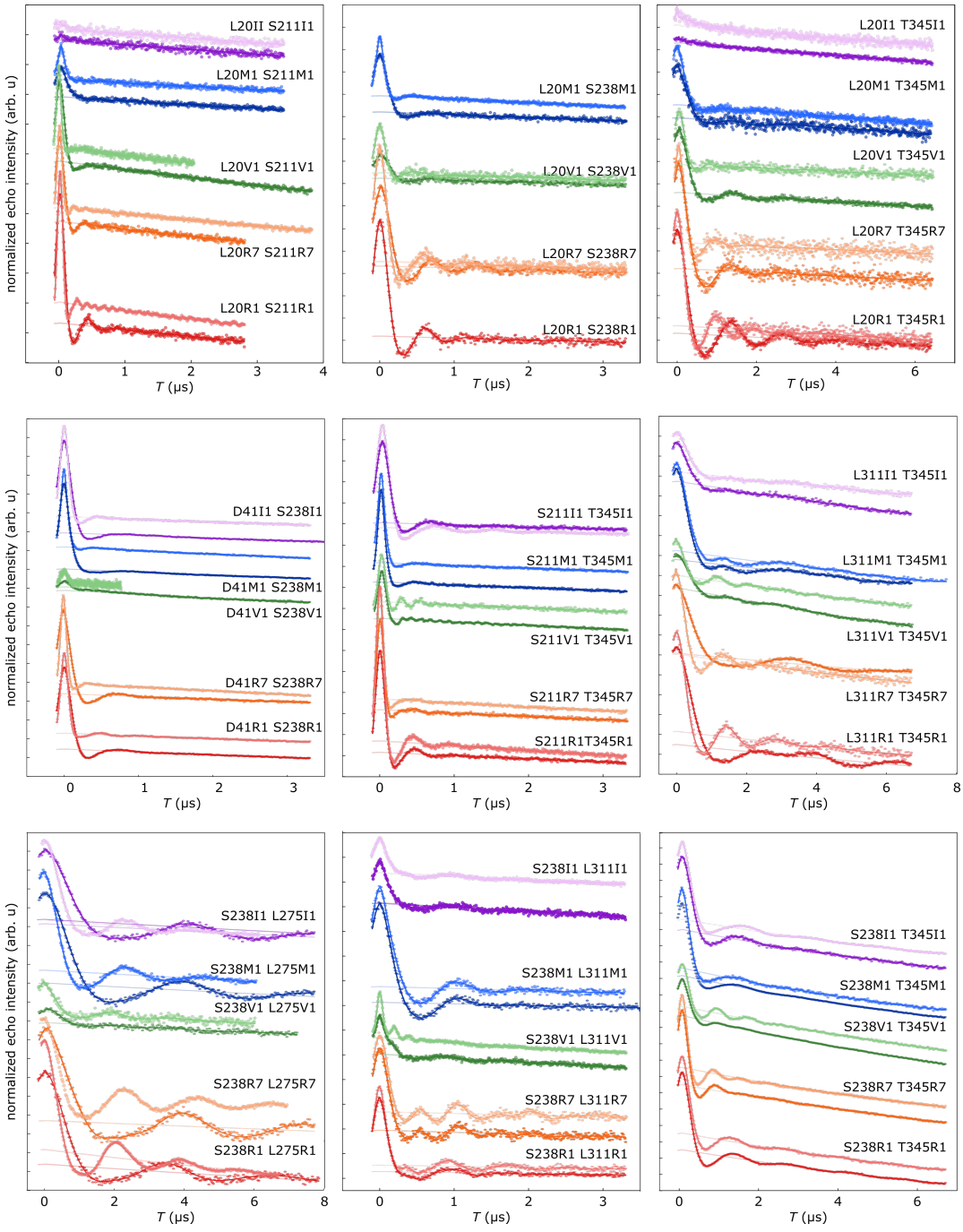

Figure 3.8: Experimental time traces (dots) with fits (opaque solid lines) and background fits (translucent solid lines) for the MBP site pairs used in this study. The R1 sidechain is shown in red, R7 in orange, V1 in green, M1 in blue, and I1 in purple.

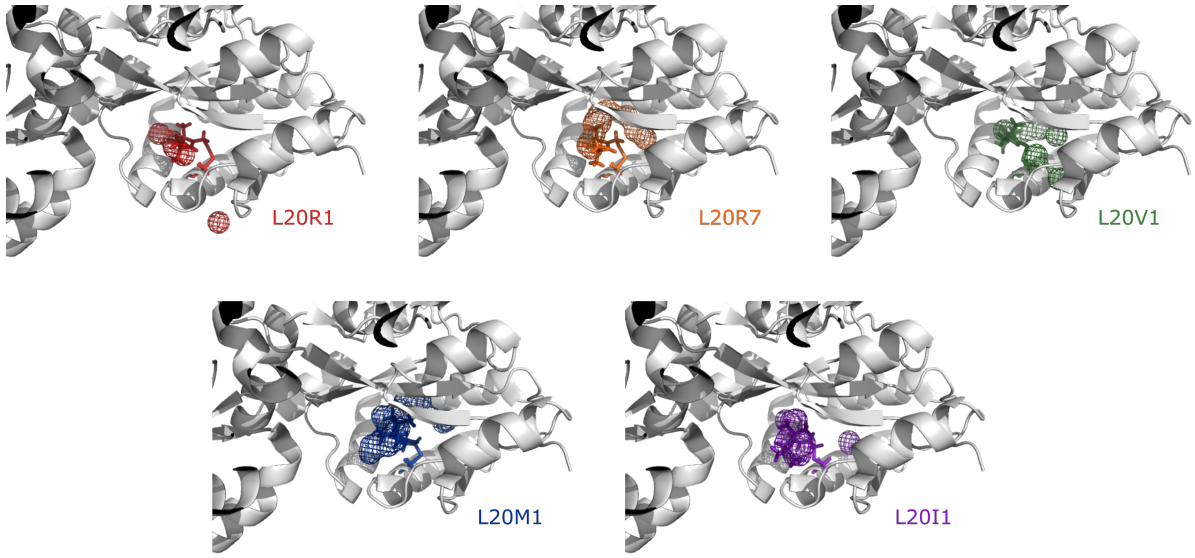

Figure 3.9: A 10 Å zoom-in on L20C apo MBP (PBD ID: 1OMP), with the spin label density of the five labels shown. This illustrates that the spin labels may exist in different conformational wells.

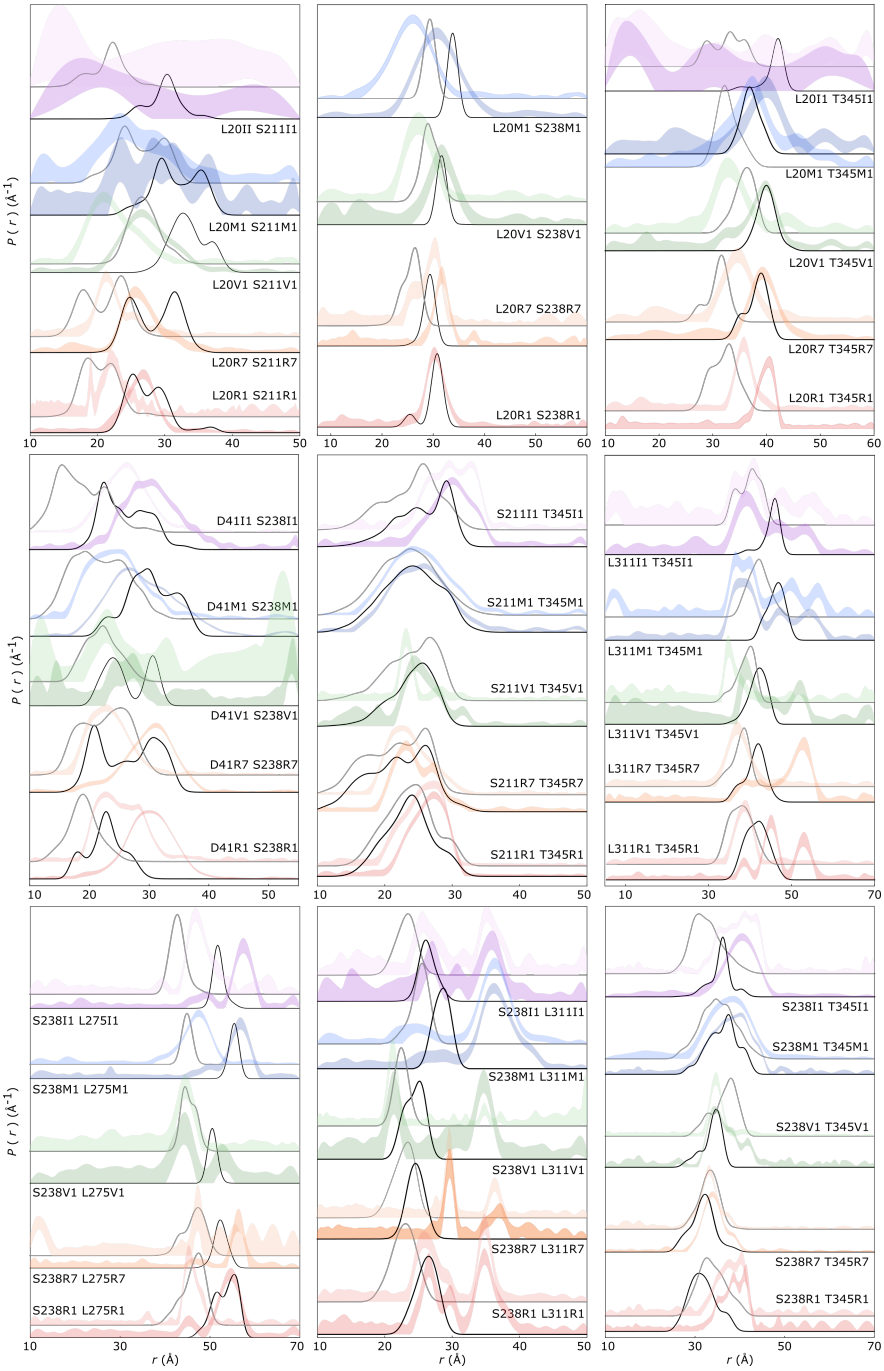

Figure 3.10: The 95% confidence intervals for the $P(r)$s of apo (dark) and maltose bound (light) MBP. R1 is shown in red, R7 is shown in orange, V1 is shown in green, M1 is shown in blue, I1 is shown in purple. The ProEPR simulations for apo and holo are shown in black and gray, respectively.

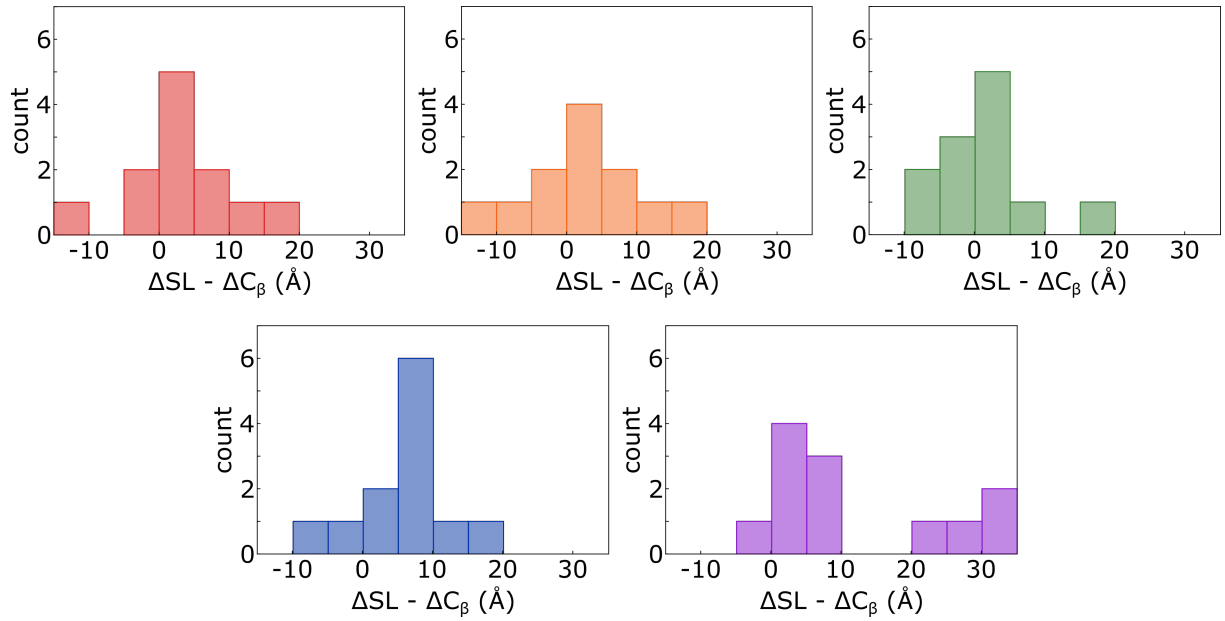

Figure 3.11: A plot of the experimental modes of the inter-spin label distance minus the C_β–C_β crystal structure distance. R1 is shown in red, R7 in orange, V1 in green, M1 in blue, and I1 in purple.

do not simply populate one conformational well. **Figure 3.9** shows an example of this with the L20C site on apo MBP. The full set of rotamer clouds can be found in **Appendix 6**. As is evident with the rotamer clouds, there are different populations oriented in different conformational wells. This makes it difficult to apply the simple approach described in **Section 3.2**.

Figure 3.11 shows the difference in modes of the inter-spin-label distances ΔSL and inter-C_β distances ΔC_β. This is a limited analysis given that the C_β distances are calculated based on the crystal structures of apo and maltose-bound MBP. It is notable, however, that the I1 sidechain tends to result in distance distributions longer than the C_β distance. Perhaps the diamond in the rough of the spin labels is the R7 sidechain, which produces similar results to the V1 sidechain, but is much easier to keep attached to the protein backbone. It

also demonstrates narrower FWHM values than the R1 sidechain does and has the ease of labeling that makes R1 so wildely used.

The various spin labels produce distance distributions of different widths. **Figure 3.12** shows the FWHM of the amplitude of the most prominent peak of the upper bound of the 95% confidence intervals as calculated by DeerLab.[94] Distributions that were not well described by a Gaussian-type FWHM analysis were excluded. This analysis does not include bimodality as a measure of FWHM—that is, in the case of samples with bimodal peaks, only the most prominent peak was used. The two proxyl labels produced the largest peak widths, which is unsurprising due to their bulkiness. The V1 side chain consistently produced the narrowest distributions, followed closely by the R7 sidechain. The R1 produced only slightly broader distributions than those of R7 and V1.

Using these trends, along with the sidechain lengths of the spin labels, it is possible to establish upper and lower bounds on the C_β distances.

Dr. Maxx Tessmer is working on the development of a software to estimate the beta-beta distance distribution from the spin-spin distribution using a neural-network model approach. The model will be trained on this dataset to investigate if this problem is solvable or if the variable space is simply too large to provide reasonable, non-computationally expensive analysis. This does not, however, preclude a multi-spin label approach being used to provide distance restraints in a protein folding software such as Rosetta.

3.4 Conclusions

This chapter details the work on the collection of a novel large DEER benchmark dataset on a conformationally flexible protein, that will consist of 90 DEER traces (9 site pairs, 5 labels, 2 states) upon completion. In addition to the DEER experiments, there are also corresponding relaxation experiments. This complete dataset contains a wealth of information and can be used as a large-scale an experimental validation test set. To my knowledge, no other dataset with this variety of spin labels and length of DEER traces exists. This dataset will aid

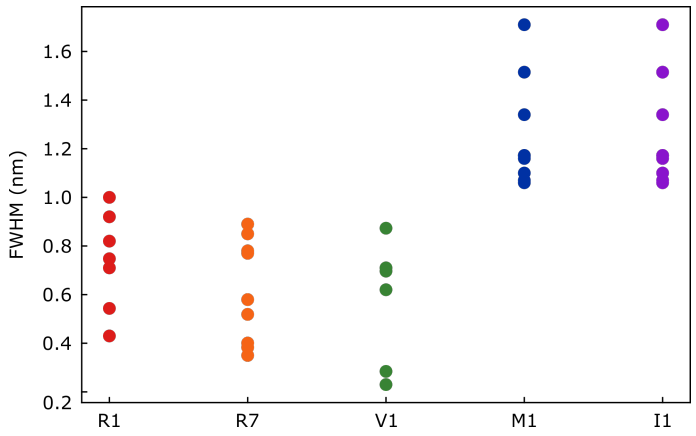

Figure 3.12: FWHM analysis of the experimentally obtained probability distributions. Only those distributions that could reasonably be fit by a single Gaussian were included in this analysis.

in developing and validating computational models that are able to back out $\beta - \beta$ from spin-spin using a variety of approaches. A software based on a neural network is currently under development.[101]

The added rigidity of the V1 sidechain relative to other side chains can produce substantially narrower distributions than the other spin labels used, but its tendency to fall off the protein is a trade-off with its rigidity.

Based on the experiences of collecting this robust dataset, I recommend using the R1, V1, and M1 sidechains for a multi-spin label protein structure determination. While the V1 sidechain is prone to falling off, with sufficiently long signal averaging, a rigid distribution can be obtained. Of the proxylsidechains, M1 consistently produced better experimental data than I1 did. The R7 sidechain produced a similar FWHM in the experimentally obtained probability distributions as that of the V1 sidechain. This demonstrates that the dominance of the R1 sidechain in the literature.

This dataset contains a wealth of information, and will be of great use in the *in silico* spin

labeling community.

Chapter 4

EPR INVESTIGATION OF A NOVEL [2Fe-2S]$^{+}$ CLUSTER

The work in this chapter was done in collaboration with Dr. Hui Wang of the Zheng lab at University of Washington. Some of these results are published.[120]

4.1 Background

Iron homeostasis is a critical function for mammalian life. Many of the most important biochemical pathways in nature are regulated by iron-sulfur-cluster-containing proteins.[121] As EPR is only sensitive to paramagnetic centers, it is a highly important technique for the characterization of FeS clusters in proteins. In fact, the specificity of local environment, including ligand coordination, spin density, and oxidation state, can be determined via EPR.[18]

Two key proteins involved in mammalian iron homeostasis are iron regulatory proteins 1 and 2, IRP1 and IRP2, respectively. They are cytoplasmic proteins that regulate iron storage at the post-transcriptional level.[122] In the case of low iron levels, IRP1 and IRP2 control iron metabolism genes by interacting with the iron-responsive elements (IREs) in their mRNA.[123,124]

While there is great sequence similarity between the two IRPs, the manner in which they bind to IREs are distinct. Upon binding to an IRE, IRP1 undergoes insertion of a [4Fe-4S] cluster and, as such, becomes a cytoplasmic aconitase.[125] IRP2 binds to IREs under conditions of limiting O_2 or Fe. Upon binding to an IRE, IRP2 undergoes a ubiquitin-dependent proteasomal degradation.[126–128]

The F-box leucine-rich-repeat protein 5 (FBXL5) is the substrate receptor of SKP1-CUL1-

Fbox. This complex specifically recognizes IRP2 and promotes its degradation under low O_2 or Fe.[129,130] FBXL5 is unique relative to other F-box proteins as it has a N-terminal hemerythrin-like domain. This heme-like domain has been been considered to be responsible for iron-controlled degradation of IRP2. The pathway for O_2-dependent degradation is unresolved.[131]

While the importance of FBXL5 in iron homeostasis has been established,[122,124,129,132] the mechanism for FBXL5 recognition of IRP2 is an open question. In this work,[120] we found a previously unknown [2Fe-2S] cluster in FBXL5 by combined biophysical, structural, and cellular methods. This chapter will only touch briefly on the non-EPR related findings. For a full description of all results, see Wang et al. 2020.[120]

4.2 Protein Expression and Fe Identification

Expression of the truncated substrate receptor FBXL5-SKP1 with the heme-like domain resulted in aggregation and weak interactions with IRP2. Thus, the N-terminal heme-like region was deleted and further sequence analysis was performed to optimize expression, and a leucine-rich repeat region predicted to be structurally disordered was deleted.

After this deletion, the purified protein was unexpectedly brown to the eye, suggesting it contained an iron-binding site. UV-vis spectroscopy showed peaks at 330 and 425 nm, which is consistent with a typical Fe-S cluster.[133]

4.3 CW EPR on FBXL5-SKP1

In order to gain more insight about this potential Fe-S cluster, CW EPR was performed. The FBXL5-SKP1 EPR samples were prepared from 300 μM FBXL5-SKP1 in 20 mM Tris pH 8.0, 150 mM NaCl, 5 mM dithiothreitol (DTT), and 20% (v/v) glycerol. The reduced EPR sample was prepared in an anaerobic box (McCoy) by the addition of 1.5 mM freshly prepared sodium dithionite. The oxidized sample was prepared aerobically by the addition of 1 mM $K_3Fe(CN)_6$. About 100 μL of solutions were transferred to 4 mm O.D. quartz tubes

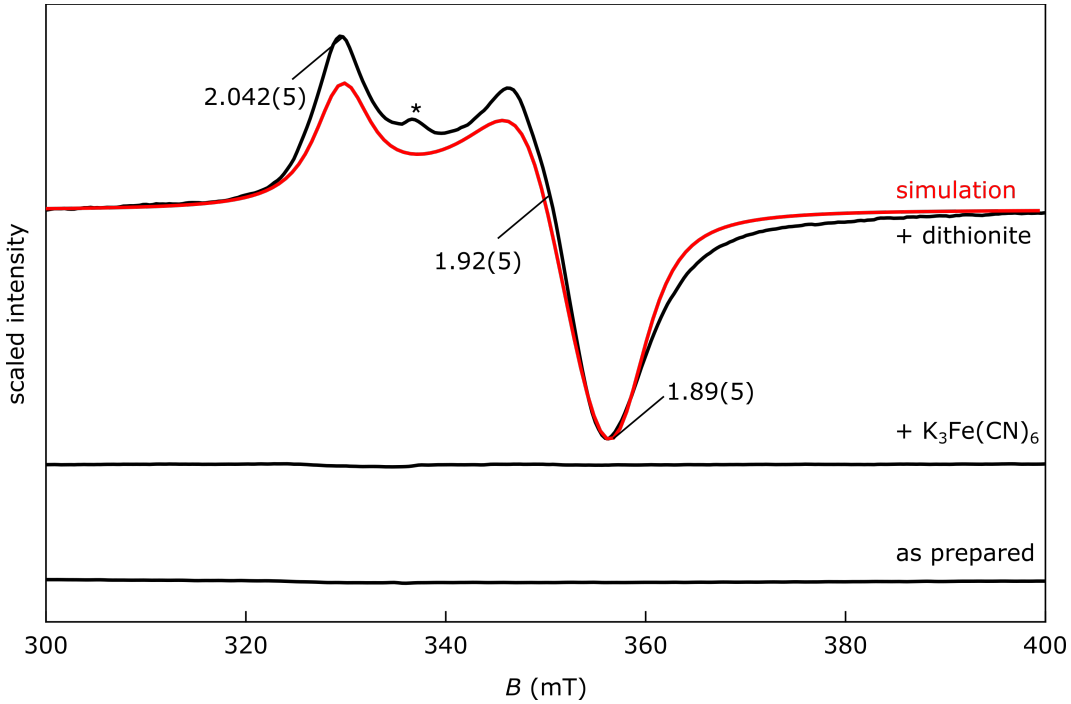

Figure 4.1: 9.425 GHz EPR spectra (black) of oxidized and reduced FBXL5 performed at 20 K, a modulation amplitude of 15 G, and a power of 32 mW. Simulation parameters (red): g-values 2.042, 1.92, and 1.89, g-strain widths 0.0001, 0.0006, and 0.0006; 1 mT Lorentzian FWHM line broadening. The asterisk indicates a small signal from an organic radical.

(Wilmad) and flash-frozen in liquid nitrogen. Atmosphere was removed by freeze-pump-thawing and the sample tubes were flame sealed. X-band EPR spectra were collected on a Bruker EMX spectrometer equipped with an SHQE resonator. The sample temperature was set to 20 K utilizing an Oxford ESR900 liquid-helium flow cryostat. The modulation amplitude was 15 G, microwave power was 32 mW, and the sweep rate was 4 mT s^{-1}. The magnetic-field axis was calibrated with a teslameter. The spectrum was simulated using EasySpin.[134]

Figure 4.1 shows 9.425 GHz EPR spectra of oxidized and reduced FBXL5-SKP1. The reduced sample shows a prominent EPR signal due to a spin-1/2 species with principal g-values of 2.042(5), 1.92(5), and 1.89(5) with an average g-value, g_{avg} of 1.96(5) in addition to a slight peak at $g \approx 4.3$. The g-values and their average, g_{avg}, are consistent with a four-cysteine coordinated ferredoxin-type $[2\text{Fe} - 2\text{S}]^{+}$ cluster.[7,18,135] The oxidized sample shows no EPR signal between 50 and 650 mT, consistent with the presence of an EPR-silent $[2\text{Fe} - 2\text{S}]^{2+}$ cluster. This coordination indicates that the four highly conserved cysteine residues involved are in the C-terminal loop region: Cys662, Cys676, Cys686, and Cys687.

4.3.1 CW EPR on FBXL5-SKP1-IRP2

The experimental spectrum shown in **Figure 4.2** is not typical of a $[2\text{Fe} - 2\text{S}]^{+}$ cluster. Two axial components were required to simulate the spectrum. Interestingly, the two components used in the simulation are a perfect match to cytosoclic aconitase treated with nitric oxide (component 1) and reduced cytosoclic aconitase treated with nitric oxide.[125]

As there was no external addition of NO to the samples, this is a highly peculiar result. DFT calculations on the geometry-optimized FeS cluster using unrestricted Kohn-Sham DFT with the BP86 functional and the def2-SVP basis were performed in ORCA 4.2.[136] There was no supporting evidence for a nitrogen-containing residue that would result in the spectral parameters observed experimentally. As the C-terminal loop region on FBXL5 is at the binding interface with IRP2 (**Figure 4.3**), it is possible that a residue on IRP2 ligating to

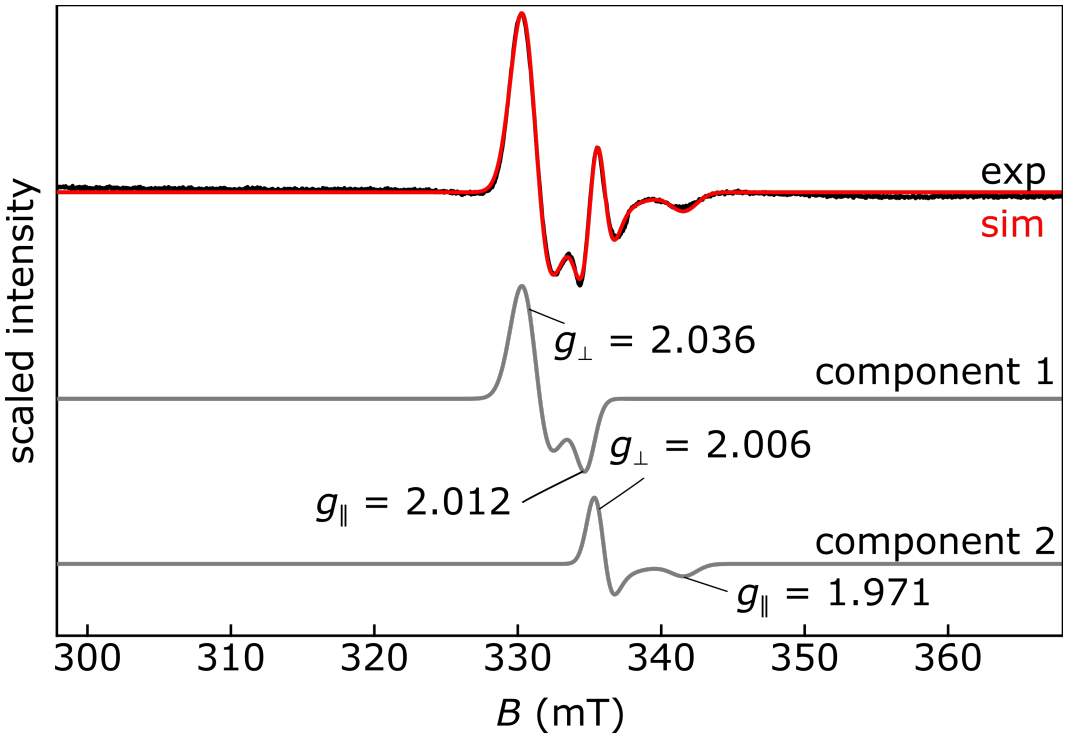

Figure 4.2: 9.443 GHz EPR spectrum of reduced FBXL5-SKP1-IRP2 (black) performed at 20 K, a modulation amplitude of 15 G, and a power of 32 mW. The simulation (red and gray) g-values were 2.036, 2.012 and 2.006, 1.971, for component 1 and 2, respectively. The broadening was included in the EasySpin parameter gStrain, which was [0.0138, 0.009] for component 1 and [0.0087, 0.0154] for component 2.

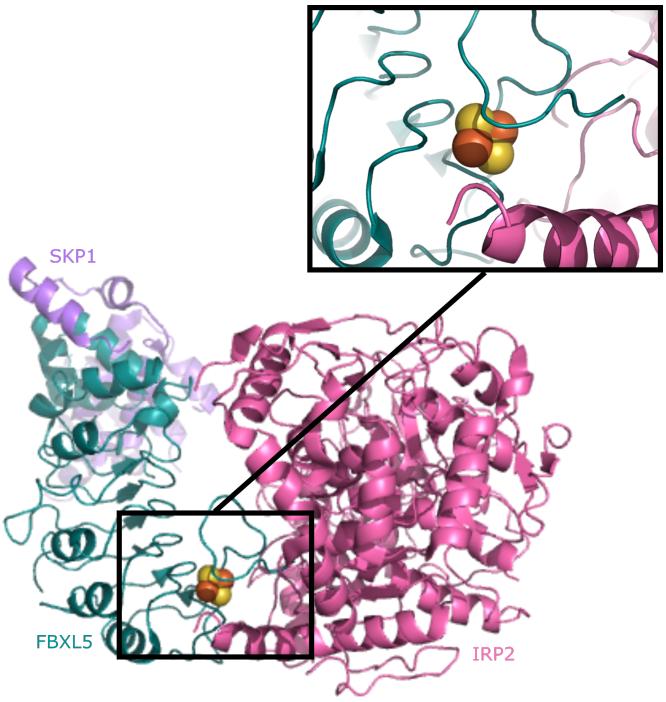

Figure 4.3: Cryo-EM structure of FBXL5-SKP1-IRP2, shown in teal, purple, and pink, respectively (PDB ID: 6VCD).[120] The $[2Fe-2S]$ cluster is shown as spheres, with iron in orange and sulfur in yellow. The zoom-in shows the 10 Åaround the cluster.

the FeS cluster and is responsible for the unusual spectrum observed.

4.4 Conclusion

While this work provided a information about a previously unknown iron regulatory pathway, there is still much work to be done on this project. At the time of writing this thesis, we are preparing to run a repeat experiment on a another freshly prepared sample to see if there is any presence of this unusual NO signal in a biological repeat. Additionally, X-band HYSCORE spectroscopy will be performed to investigate the possible origins of this unusual signal.

Chapter 5

MBP SAMPLE PREPARATION

Binding Buffer: 20 mM Tris-HCl, pH 7.5, 20 mM imidazole

Wash Buffer: 20 mM Tris-HCl pH 7.5, 150 mM NaCl, 30 mM imidazole

Elution Buffer: 20 mM Tris pH 7.5, 150 mM NaCl, 300 mM imidazole

Spin Labeling Buffer: 20 mM Tris-HCl pH 7.5, 150 mM NaCl

CW EPR Buffer: 20 mM Tris-HCl pH 7.5, 150 mM NaCl, 20% glycerol

DEER Buffer: 20 mM Tric-HCl pH 7.5, 140 mM NaCl, 50% (%w) d_8-glycerol in D_2O

Pelleted cells were resuspended in ca. 30 mL of Binding Buffer with DNAse, lysozyme, and PMSF. The cells were disrupted with sonication and then centrifuged at 4°. The supernatant was run through an Ni-NTA gravity column. Two wash steps were performed with ca. 30 mL of Wash Buffer. The protein was eluted using elution buffer. Protein concentration was determined using UV-vis.

Chapter 6

PROEPR ROTAMERS

Rotamer density clouds, shown as surface meshes were obtained by ProEPR using and were visualized using Pymol.

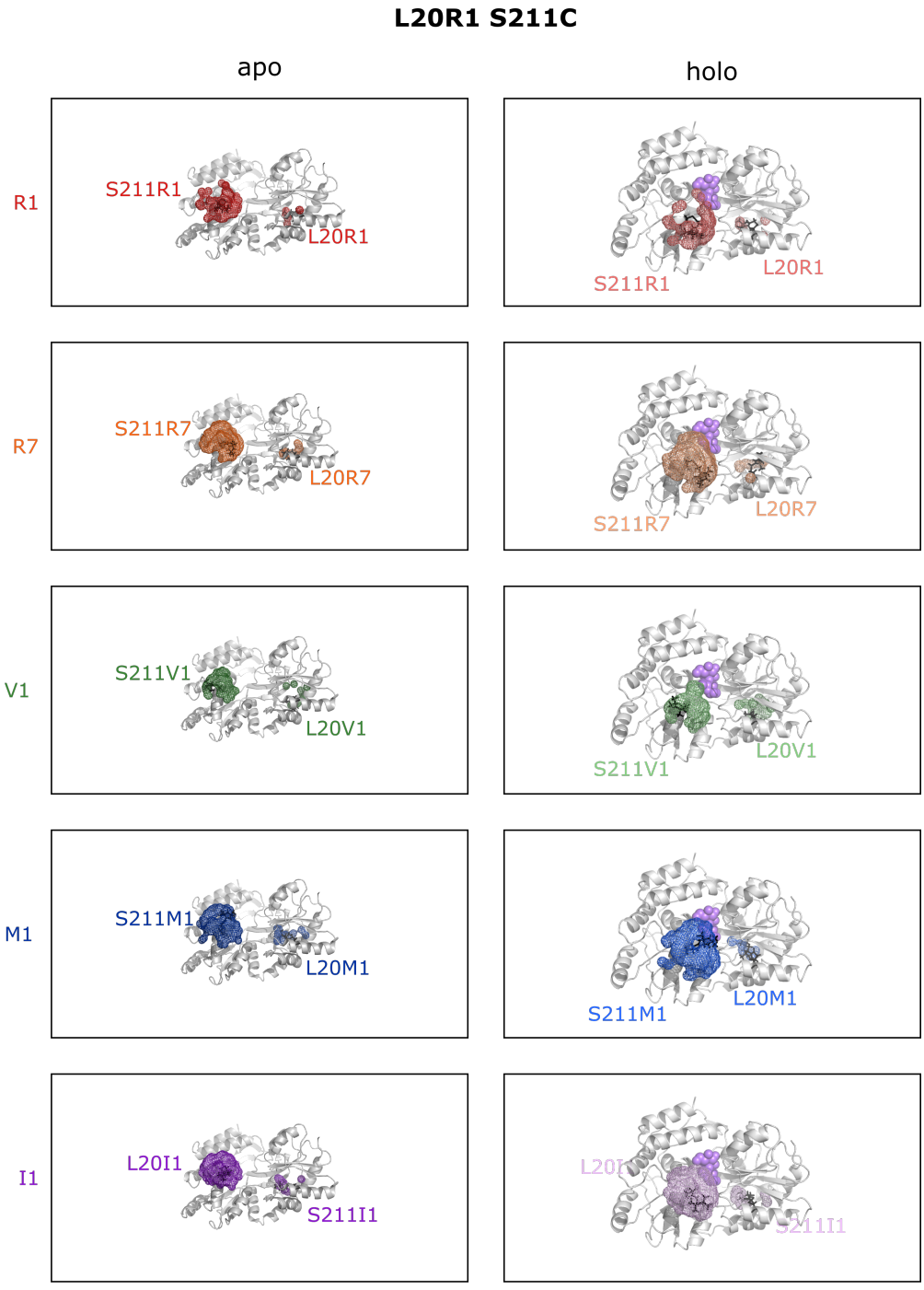

Figure 6.1: ProEPR-generated rotamer densities for apo (PDB ID: 1OMP) and holo (PDB ID: 1ANF) L20C L211C MBP.

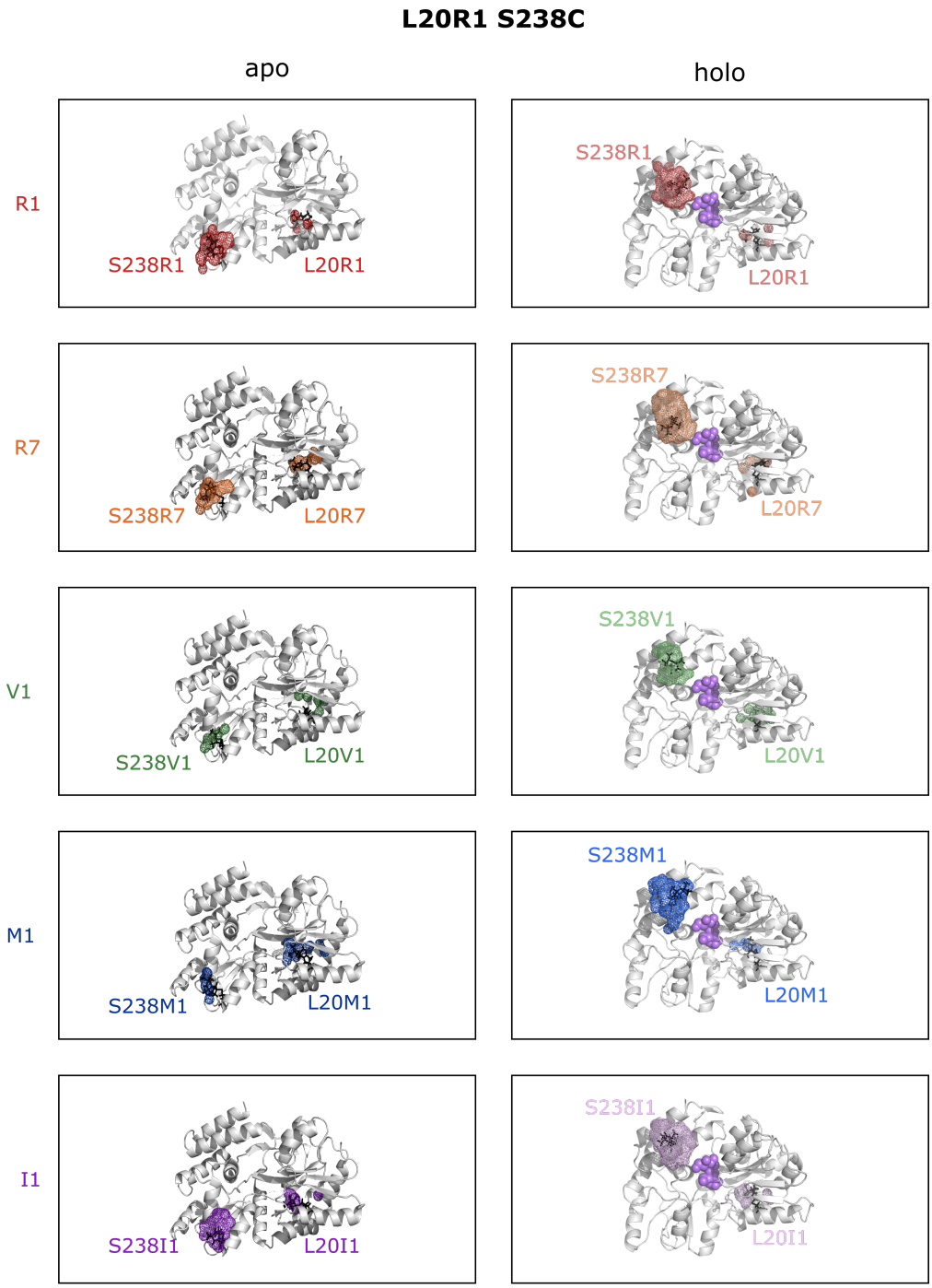

Figure 6.2: ProEPR-generated rotamer densities for apo (PDB ID: 1OMP) and holo (PDB ID: 1ANF) L20C S238C MBP.

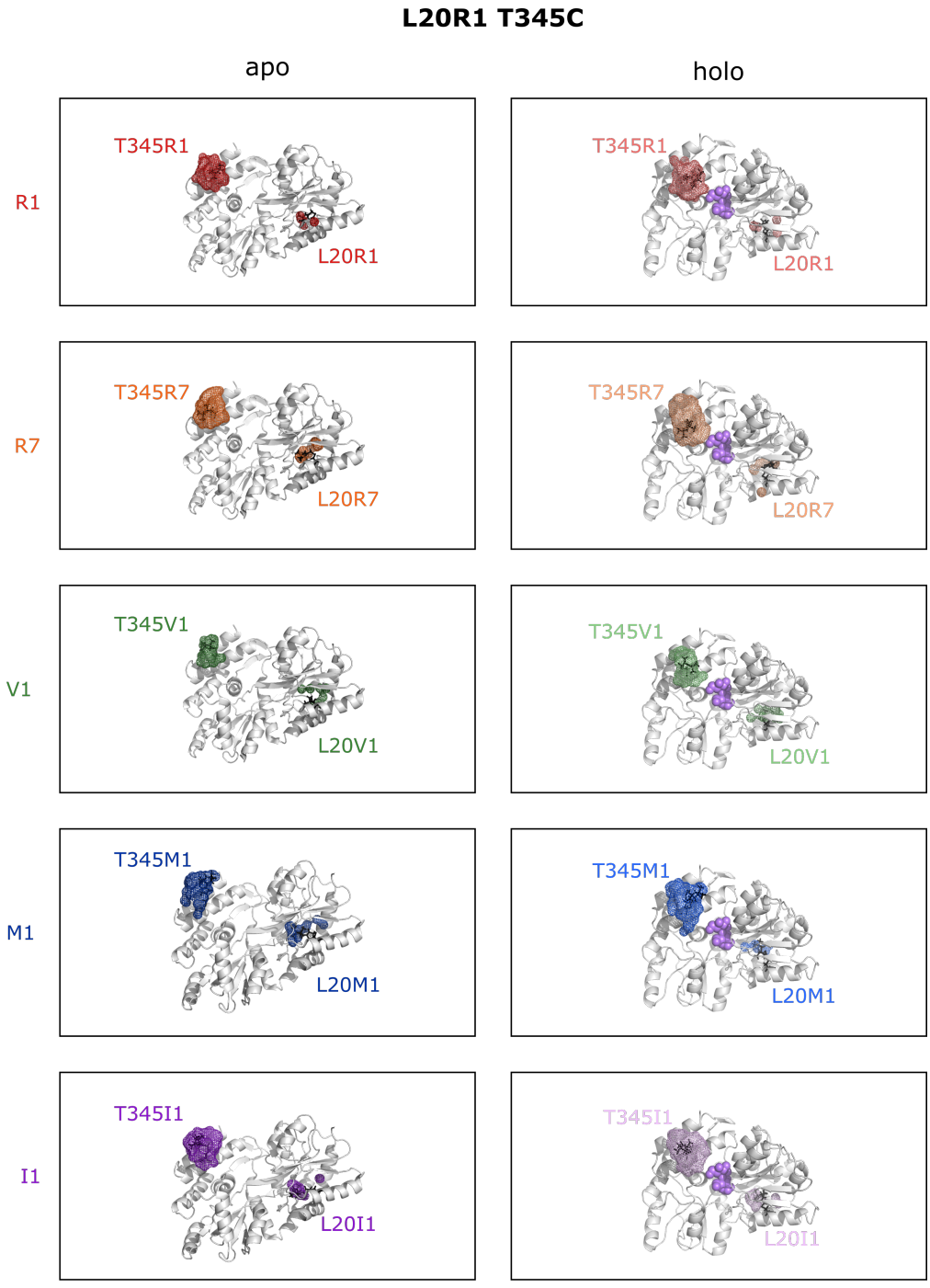

Figure 6.3: ProEPR-generated rotamer densities for apo (PDB ID: 1OMP) and holo (PDB ID: 1ANF) L20C T345C MBP.

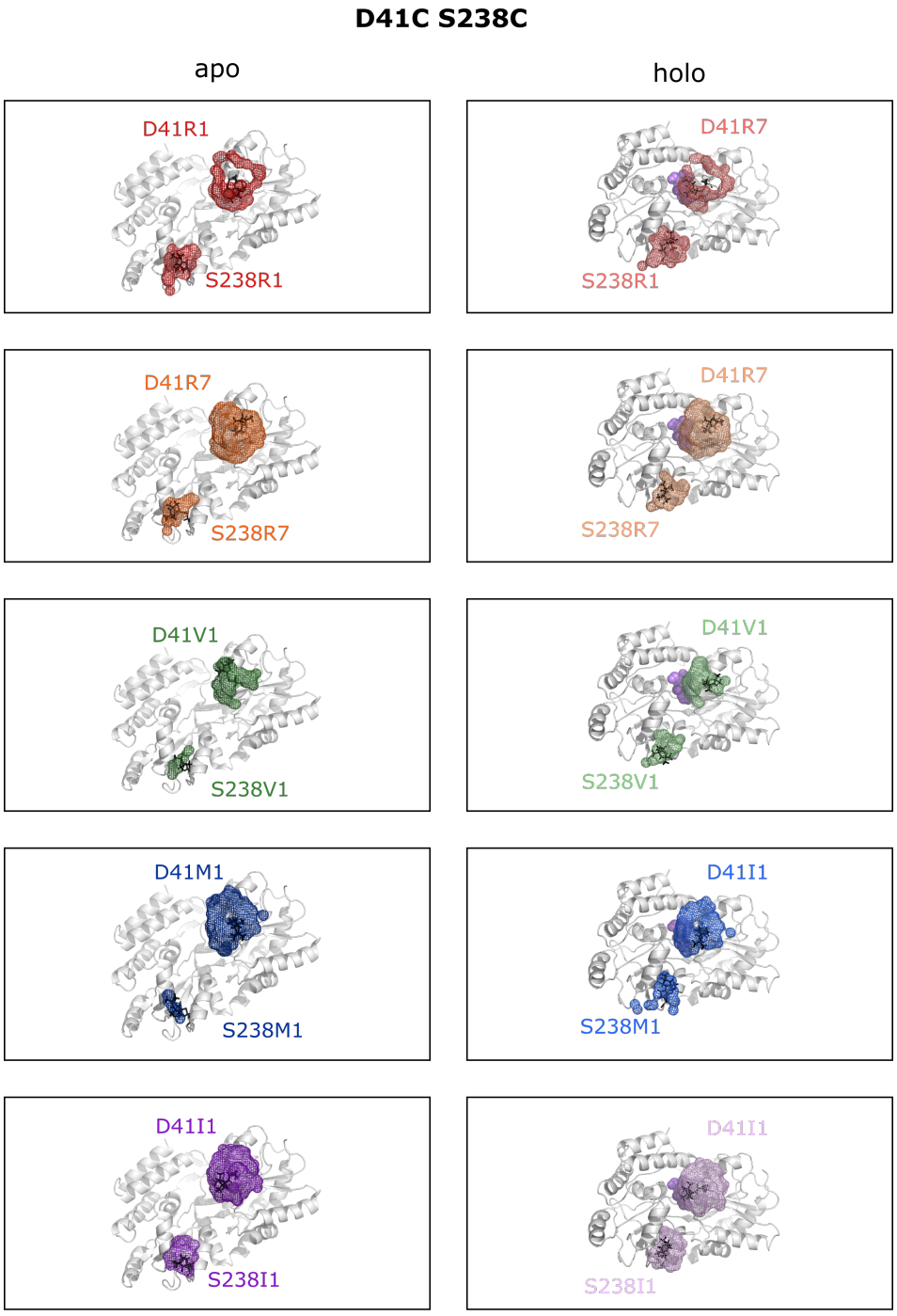

Figure 6.4: ProEPR-generated rotamer densities for apo (PDB ID: 1OMP) and holo (PDB ID: 1ANF) D41C S238C MBP.

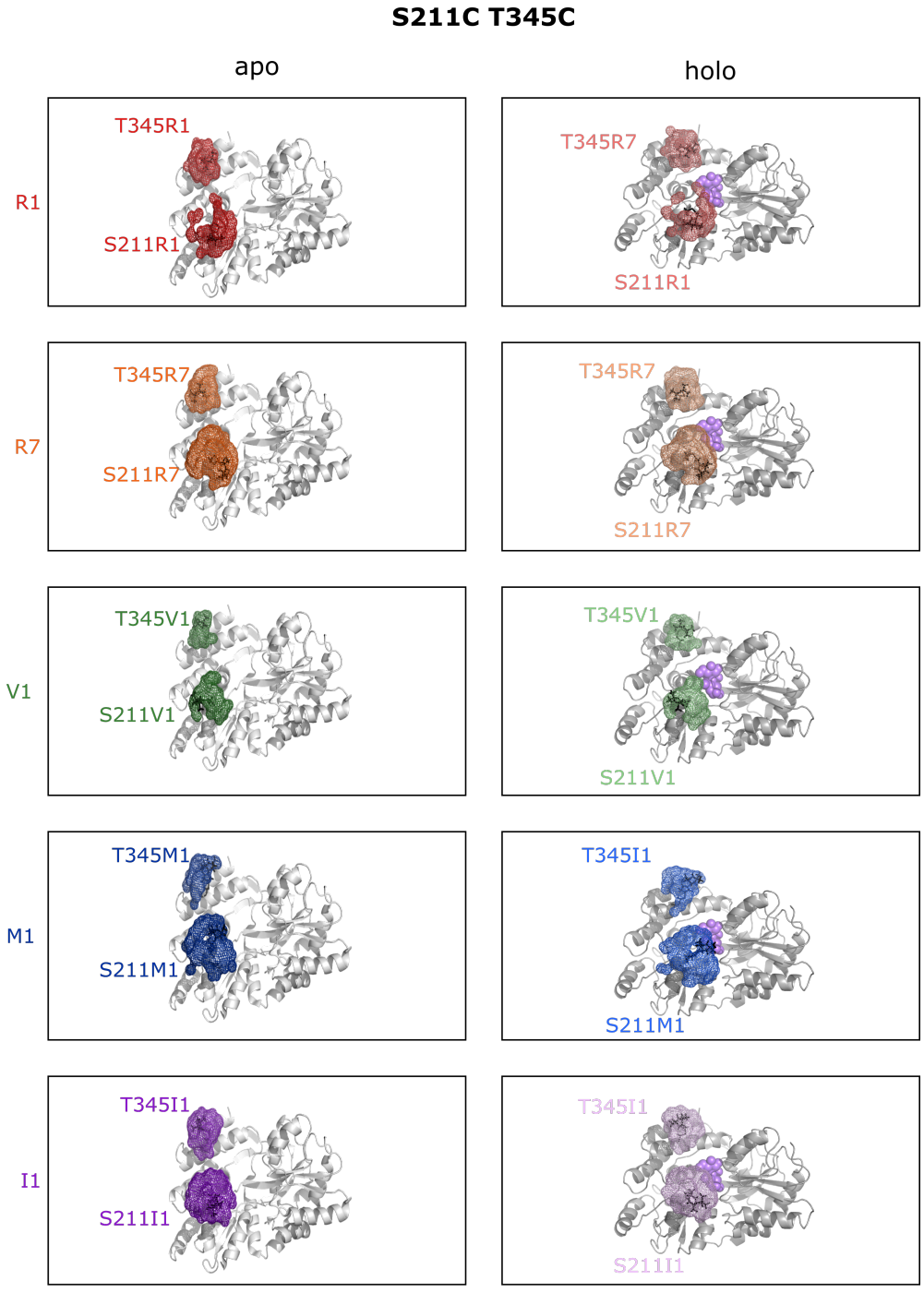

Figure 6.5: ProEPR-generated rotamer densities for apo (PDB ID: 1OMP) and holo (PDB ID: 1ANF) S211C T345C MBP.

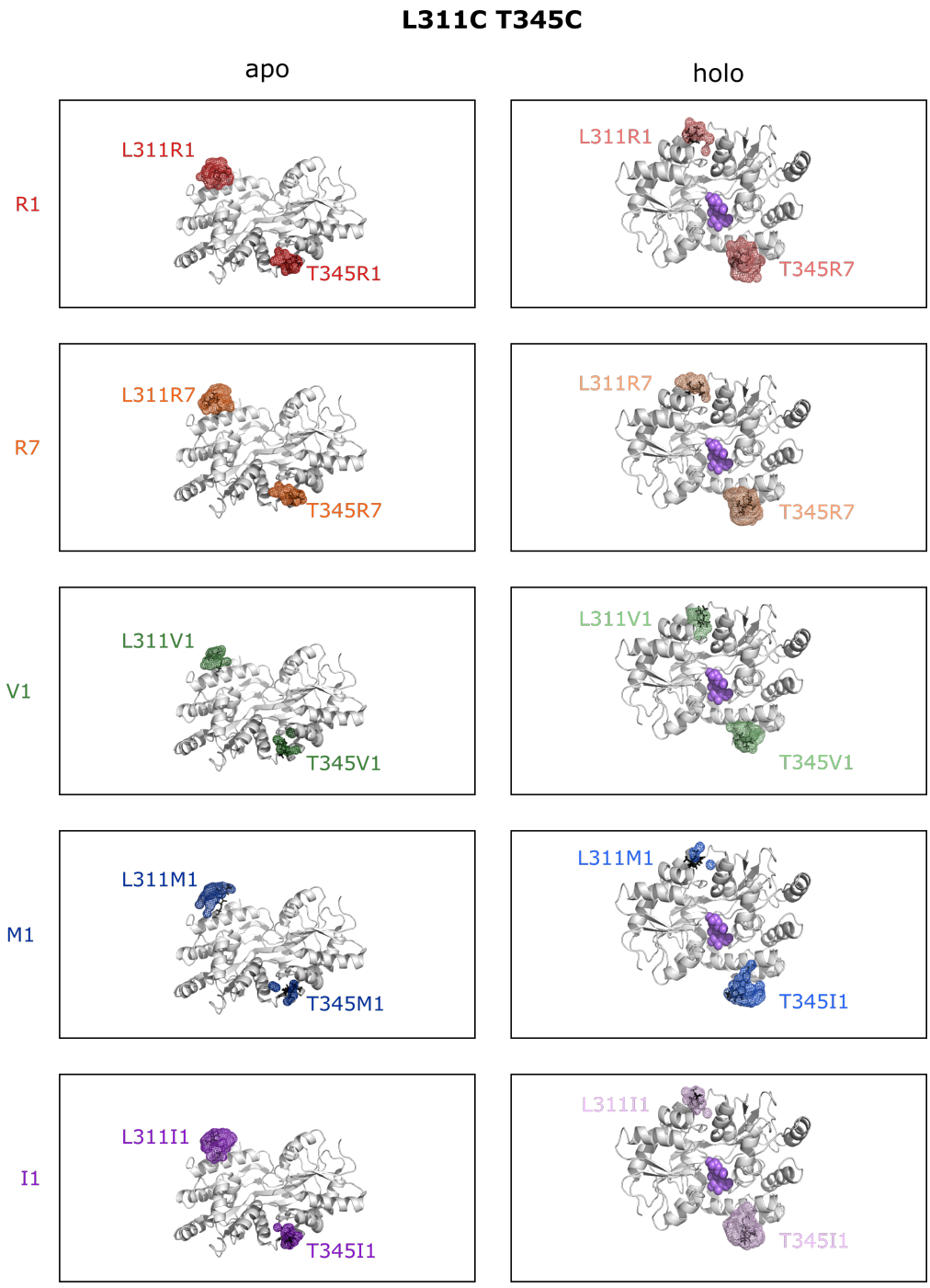

Figure 6.6: ProEPR-generated rotamer densities for apo (PDB ID: 1OMP) and holo (PDB ID: 1ANF) L311C T345C MBP.

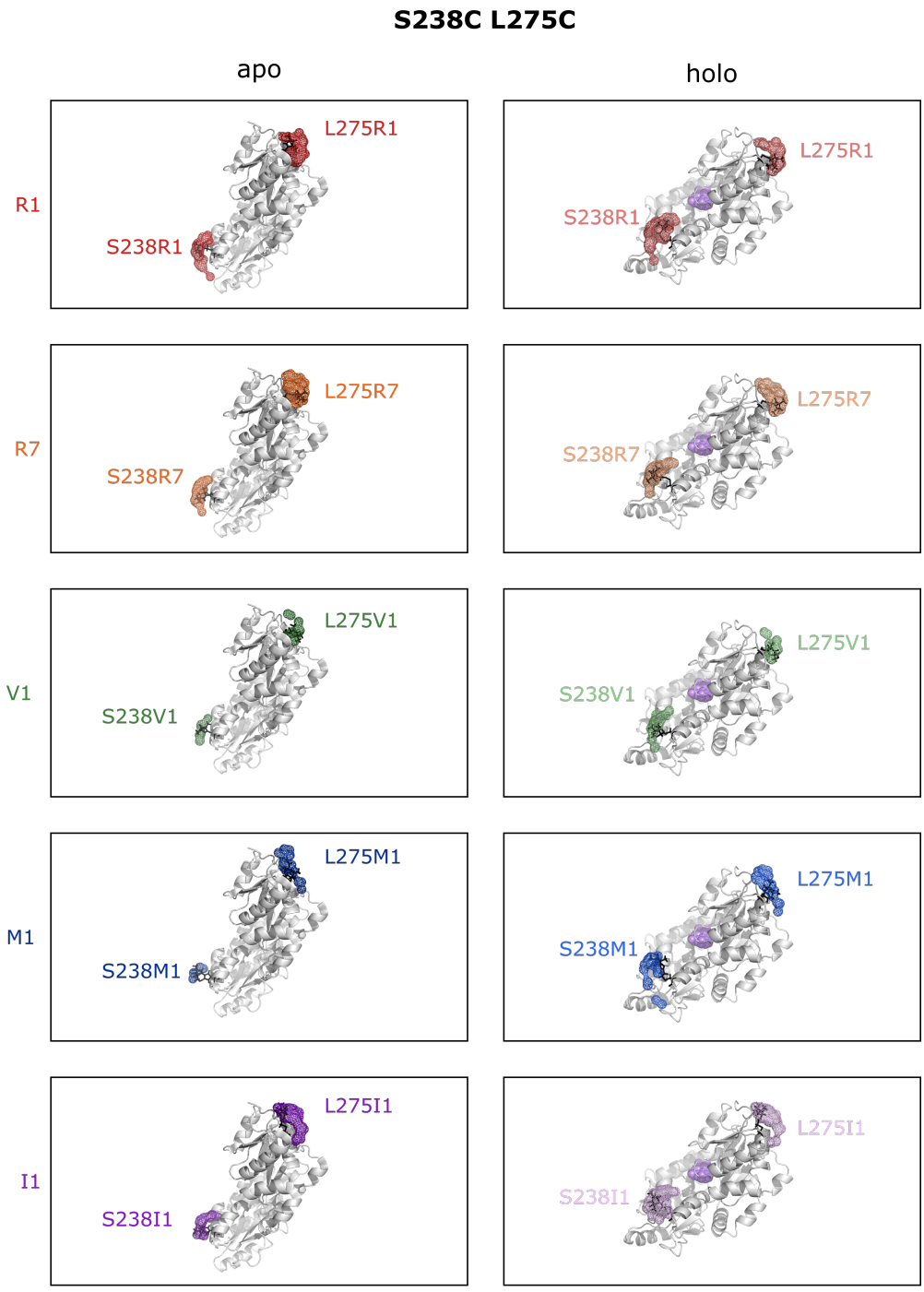

Figure 6.7: ProEPR-generated rotamer densities for apo (PDB ID: 1OMP) and holo (PDB ID: 1ANF) S238C L275 MBP.

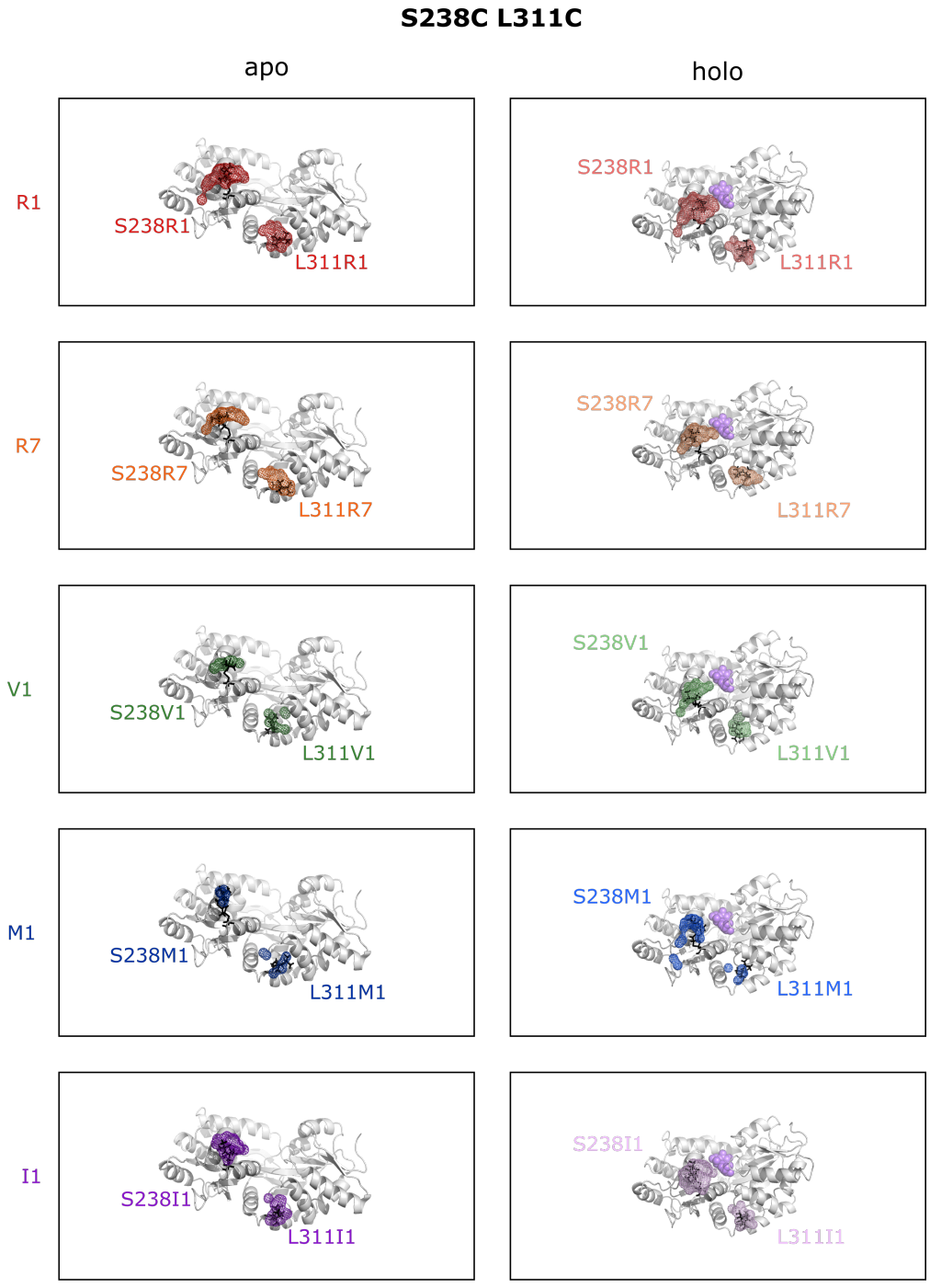

Figure 6.8: ProEPR-generated rotamer densities for apo (PDB ID: 1OMP) and holo (PDB ID: 1ANF) S238C L311C MBP.

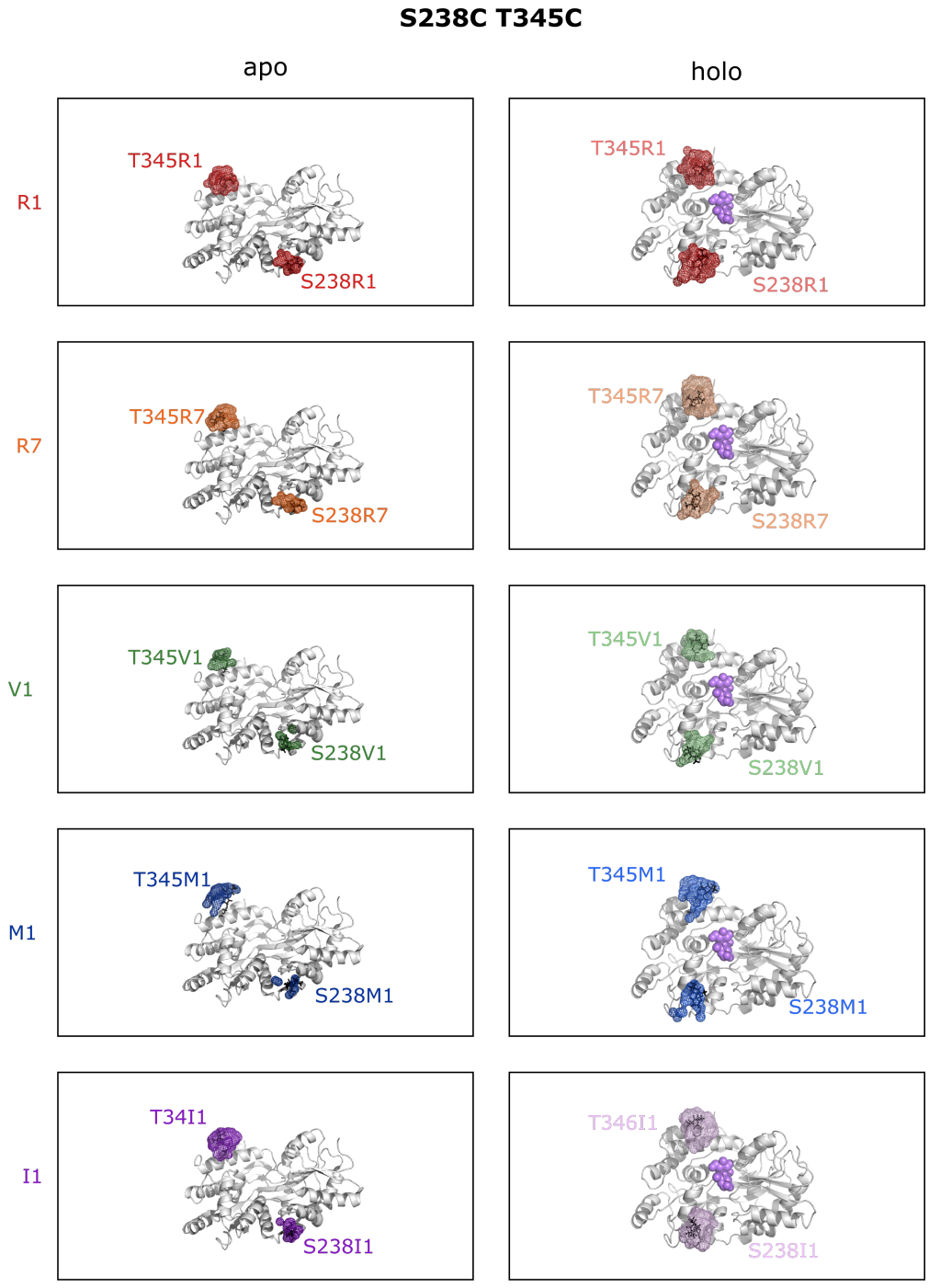

Figure 6.9: ProEPR-generated rotamer densities for apo (PDB ID: 1OMP) and holo (PDB ID: 1ANF) S238C T345C MBP.

BIBLIOGRAPHY

[1] Charles E. Dutoit, Laurent Binet, Hitomi Fujii, Agnes Lattuati-Derieux, and Didier Gourier. Nondestructive Analysis of Mummification Balms in Ancient Egypt Based on EPR of Vanadyl and Organic Radical Markers of Bitumen. *Analytical Chemistry*, 92(23):15445–15453, 2020.

[2] Arthur Schweiger and Gunnar Jeschke. *Principles of pulse electron paramagnetic resonance*. Oxford University Press, New York, NY, 1st edition, 2001.

[3] John A. Weil and James R. Bolton. *Electron Paramagnetic Resonance: Elementary Theory and Practical Applications*. Wiley-Interscience, Hoboken, NJ, 2nd edition, 2007.

[4] Gareth R. Eaton, Sandra S. Eaton, David P. Barr, and Ralph T. Weber. *Quantitative EPR*. Springer, Vienna, Vienna, 1st edition, 2010.

[5] Daniella Goldfarb and Stefan Stoll, editors. *EPR Spectroscopy: Fundamentals and Methods*. Wiley, Chichester, West Sussex, 2018.

[6] Victor Chechik, Emma Carter, and Damien Murphy. *Electron Paramagnetic Resonance*. Oxford University Press, New York, NY, 1st edition, 2016.

[7] Jing Liu, Saumen Chakraborty, Parisa Hosseinzadeh, Yang Yu, Shiliang Tian, Igor Petrik, Ambika Bhagi, and Yi Lu. Metalloproteins containing cytochrome, iron-sulfur, or copper redox centers. *Chemical Reviews*, 114:4366–4369, 2014.

[8] Kelly L. Adams, Maja Puchades, and Andrew G. Ewing. In Vitro Electrochemistry of Biological Systems. *Annual Review of Analytical Chemistry*, 1:329–55, 2008.

[9] Bijan Ranjbar and Pooria Gill. Circular dichroism techniques: Biomolecular and nanostructural analyses – A review. *Chemical Biology and Drug Design*, 74:101–120, 2009.

[10] M. Buchner, K. Höfler, B. Henne, V. Ney, and A. Ney. Tutorial: Basic principles, limits of detection, and pitfalls of highly sensitive SQUID magnetometry for nanomagnetism and spintronics. *Journal of Applied Physics*, 124:161101–161113, 2018.

[11] Alexander A. Kamnev and Anna V. Tugarova. Sample treatment in Mössbauer spectroscopy for protein-related analyses: Nondestructive possibilities to look inside metal-containing biosystems. *Talanta*, 174:819–837, 2017.

[12] Peter Gast and Edgar J.J. Groenen. EPR Interactions – g-Anisotropy. *eMagRes*, 5:1435–1444, 2016.

[13] P.G. Kruger. Nuclear Shells: Angular and Magnetic Momenta of Nuclei. *Physical Review*, 47:605–610, 1935.

[14] P. Kusch and H.M. Foley. The magnetic moment of the electron. *Physical Review*, 74:250–263, 1948.

[15] Frank Neese. Quantum Chemistry and EPR Parameters. *eMagRes*, 6:1–22, 2017.

[16] Patrick Bertrand, Bruno Guigliarelli, Jean-Pierre Gayda, Peter Beardwood, and John F. Gibson. A ligand-field model to describe a new class of 2Fe-2S clusters in proteins and their synthetic analogues. *Biochimica et Biophysica Acta*, 831:124–133, 1985.

[17] Antony R. Crofts, Vladimir P. Shinkarev, Sergei A. Dikanov, Rimma I. Samoilova, and Derrick Kolling. Interactions of quinone with the iron-sulfur protein of the bc1 complex: Is the mechanism spring-loaded? *Biochimica et Biophysica Acta–Bioenergetics*, 1555:48–53, 2002.

[18] A. A. Shubin and S. A. Dikanov. Variations of g-Tensor Principal Values in Reduced [2Fe-2S] Cluster of Iron-Sulfur Proteins. *Applied Magnetic Resonance*, 30:399–416, 2006.

[19] Lizhi Tao, Troy A. Stich, Corey J. Fugate, Joseph T. Jarrett, and R. David Britt. EPR-Derived Structure of a Paramagnetic Intermediate Generated by Biotin Synthase BioB. *Journal of the American Chemical Society*, 140:12947–12963, 2018.

[20] Ellen C. Hayes, Yajun Jian, Lei Li, and Stefan Stoll. EPR Study of UV-Irradiated Thymidine Microcrystals Supports Radical Intermediates in Spore Photoproduct Formation. *The Journal of Physical Chemistry B*, 120:10923–10931, 2016.

[21] Marina Bennati. EPR Interactions – Hyperfine Couplings. *eMagRes*, 6:271–282, 2017.

[22] B. T. Allen and D. W. Nebert. Hyperfine Structure in the EPR Spectrum of the Manganous Ion in Frozen Solutions. *The Journal of Chemical Physics*, 41:1983–1985, 1964.

[23] Gunnar Jeschke and Arthur Schweiger. Hyperfine-correlated electron nuclear double resonance spectroscopy. *Chemical Physics Letters*, 246:431–438, 1995.

[24] Thorsten Maly, Klaus Zwicker, Adrian Cernescu, Ulrich Brandt, and Thomas F. Prisner. New pulsed EPR methods and their application to characterize mitochondrial complex I. *Biochimica et Biophysica Acta–Bioenergetics*, 1787:584–592, 2009.

[25] Sabine Richert, Claudia E. Tait, and Christiane R. Timmel. Delocalisation of photoexcited triplet states probed by transient EPR and hyperfine spectroscopy. *Journal of Magnetic Resonance*, 280:103–116, 2017.

[26] Donald Mannikko and Stefan Stoll. Vanadyl Porphyrin Speciation Based on Submegahertz Ligand Proton Hyperfine Couplings. *Energy & Fuels*, 33:4237–4243, 2019.

[27] Sandra S. Eaton and Gareth R. Eaton. Relaxation Times of Organic Radicals and Transition Metal Ions. In Lawrence J. Berliner, Sandra S. Eaton, and Gareth R. Eaton, editors, *Biological Magnetic Resonance Volume 19: Distance Measurements in Biological Systems by EPR*, chapter Relaxation, pages 29–129. Kluwer Academic/Plenum Publishers, New York, NY, 2000.

[28] A. Zecevic, G. R. Eaton, S. S. Eaton, and M. Lindgren. Dephasing of electron spin echoes for nitroxyl radicals in glassy solvents by non-methyl and methyl protons. *Molecular Physics*, 95:1255–1263, 1998.

[29] Edward Reijerse and Anton Savitsky. Electron paramagnetic resonance instrumentation. *eMagRes*, 6:187–206, 2017.

[30] James S. Hyde, Robert A. Strangeway, and Jason W. Sidabras. Dispersion EPR: Considerations for Low-Frequency Experiments. *Applied Magnetic Resonance*, 2021.

[31] Art Van Der Est. Continuous-wave EPR. *eMagRes*, 5:1411–1422, 2016.

[32] G. Marius Clore and Junji Iwahara. Theory, Practice, and Applications of Paramagnetic Relaxation Enhancement for the Characterization of Transient Low-Population States of Biological Macromolecules and Their Complexes. *Chemical Review*, 109:4108–4139, 2009.

[33] Laura Galazzo, Gianmarco Meier, M. Hadi Timachi, Cedric A. J. Hutter, Markus A. Seeger, and Enrica Bordignon. Spin-labeled nanobodies as protein conformational reporters for electron paramagnetic resonance in cellular membranes. *Proceedings of the National Academy of Sciences*, 117(5):2441–2448, 2020.

[34] Sandra S. Eaton and Gareth R. Eaton. Distance Measurements by CW and Pulsed EPR. In Lawrence J. Berliner, Sandra S. Eaton, and Gareth R. Eaton, editors, *Biological Magnetic Resonance Volume 19: Distance Measurements in Biological Systems by EPR*, chapter 1, pages 1–28. Springer, Boston, MA, 1st edition, 2002.

[35] Sabine Van Doorslaer. Hyperfine spectroscopy: ESEEM. *eMagRes*, 6:51–70, 2017.

[36] Elizabeth R. Canarie, Samuel M. Jahn, and Stefan Stoll. Quantitative Structure-Based Prediction of Electron Spin Decoherence in Organic Radicals. *Journal of Physical Chemistry Letters*, 11:3396–3400, 2020.

[37] Sandra S. Eaton and Gareth R. Eaton. Relaxation mechanisms. *eMagRes*, 5:1543–1556, 2016.

[38] Gunnar Jeschke. Dipolar spectroscopy-double-resonance methods. *eMagRes*, 5:1459–1476, 2016.

[39] Ana Zecevic, Gareth R. Eaton, Sandra S. Eaton, and Mikael Lindgren. Dephasing of electron spin echoes for nitroxyl radicals in glassy solvents by non-methyl and methyl protons. *Molecular Physics*, 95:1255–1263, 1998.

[40] Michael J. Graham, Joseph M. Zadrozny, Muhandis Shiddiq, John S. Anderson, Majed S. Fataftah, Stephen Hill, and Danna E. Freedman. Influence of Electronic Spin and Spin-Orbit Coupling on Decoherence in Mononuclear Transition Metal Complexes. *Journal of the American Chemical Society*, 136:7623–7626, 2014.

[41] G. M. Zhidomirov and K. M. Salikhov. Contribution to the Theory of Spectral Diffusion in Magnetically Diluted Solids. *Soviet Physics Journal of Experimental and Theoretical Physics*, 29:1037–1040, 1969.

[42] A. D. Milov, K. M. Salikhov, and Yuri D. Tsvetkov. Phase relaxation of hydrogen atoms stabilized in an amorphous matrix. *Soviet Physics Solid State*, 15:802–806, 1973.

[43] P. Hu and S. R. Hartmann. Theory of spectral diffusion decay using an uncorrelated-sudden-jump model. *Physical Review B*, 9:9–13, 1974.

[44] W. M. Witzel and S. Das Sarma. Quantum theory for electron spin decoherence induced by nuclear spin dynamics in semiconductor quantum computer architectures: Spectral diffusion of localized electron spins in the nuclear solid-state environment. *Physical Review B – Condensed Matter and Materials Physics*, 74:1–24, 2006.

[45] S. Lenz, K. Bader, H. Bamberger, and J. Van Slageren. Quantitative prediction of nuclear-spin-diffusion- limited coherence times of molecular quantum bits based on copper(II). *ChemComm*, 53:4477–4480, 2017.

[46] Ilirian Dhimitruka, Andrey A. Bobko, Timothy D. Eubank, Denis A. Komarov, Valery V. Khramtsov, and Dorothy M. Davis. Phosphonated Trityl Probes for Concurrent in Vivo Tissue Oxygen and pH Monitoring Using Electron Paramagnetic Resonance-Based Techniques. *Journal of the American Chemical Society*, 135:5904–5910, 2013.

[47] J. R. Klauder and P. W. Anderson. Spectral Diffusion Decay in Spin Resonance Experiments. *Physical Review*, 125:912–932, 1962.

[48] K. M. Salikhov, S. A. Dzuba, and A. M. Raitsimring. The theory of electron spin-echo signal decay resulting from dipole-dipole interactions between paramagnetic centers in solids. *Journal of Magnetic Resonance*, 42:255–276, 1981.

[49] Vasily S. Oganesyan. A general approach for prediction of motional EPR spectra from Molecular Dynamics (MD) simulations: application to spin labelled protein. *Physical Chemistry Chemical Physics*, 13:4724–4737, 2011.

[50] Robert B. Best, Xiao Zhu, Jihyun Shim, Pedro E. M. Lopes, Jeetain Mittal, Michael

Feig, and Alexander D. Mackerell. Optimization of the Additive CHARMM All-Atom Protein Force Field Targeting Improved Sampling of the Backbone ϕ, ψ and Side-Chain χ_1 and χ_2 Dihedral Angles. *Journal of Chemical Theory and Computation*, 8:3257–3273, 2012.

[51] Glycerine Producers' Association, editor. *Physical Properties of Glycerine and its Solutions*. Glycerine Producers' Association, New York, NY, 1963.

[52] Adrien Lerbret and Frédéic Affouard. Molecular Packing, Hydrogen Bonding, and Fast Dynamics in Lysozyme/Trehalose/Glycerol and Trehalose/Glycerol Glasses at Low Hydration. *Journal of Physical Chemistry B*, 121:9437-9451, 2017.

[53] Rikard Owenius, Maria Engström, Mikael Lindgren, and Martina Huber. Influence of Solvent Polarity and Hydrogen Bonding on the EPR Parameters of a Nitroxide Spin Label Studied by 9-GHz and 95-GHz EPR Spectroscopy and DFT Calculations. *Journal of Physical Chemistry A*, 105:10967–10977, 2001.

[54] Marcos De Oliveira, Robert Knitsch, Muhammad Sajid, Annika Stute, Lisa-Maria Elmer, Gerald Kehr, Gerhard Erker, Claudio J. Magon, Gunnar Jeschke, and Hellmut Eckert. Aminoxyl Radicals of B/P Frustrated Lewis Pairs: Refinement of the Spin-Hamiltonian Parameters by Field-and Temperature-Dependent Pulsed EPR Spectroscopy. *PLoS ONE*, 11:e0157944, 2016.

[55] Wen Yang and Ren Bao Liu. Quantum many-body theory for qubit decoherence in a finite-size spin bath. *AIP Conference Proceedings*, 1074:68–71, 2008.

[56] Wen Yang and Ren-Bao Liu. Quantum many-body theory of qubit decoherence in a finite-size spin bath. II. Ensemble dynamics. *Physical Review B*, 79:1–22, 2009.

[57] Wen Long Ma, Gary Wolfowicz, Nan Zhao, Shu Shen Li, John J.L. Morton, and Ren Bao Liu. Uncovering many-body correlations in nanoscale nuclear spin baths by central spin decoherence. *Nature Communications*, 5:4822, 2014.

[58] Samuel M. Jahn, Elizabeth R. Canarie, and Stefan Stoll. Effect of matrix deuteration on electron spin decoherence. *In preparation*, 2021.

[59] Janne Soetbeer, Miriam Hü, Adelheid Godt, Yevhen Polyhach, and Gunnar Jeschke. Dynamical decoupling of nitroxides in o-terphenyl: a study of temperature, deuteration and concentration effects. *Physical Chemistry Chemical Physics*, 20:1615–1628, 2018.

[60] Dora Toledo Warshaviak, Valery V. Khramtsov, Duilio Cascio, Christian Altenbach, and Wayne L. Hubbell. Structure and dynamics of an imidazoline nitroxide side chain with strongly hindered internal motion in proteins. *Journal of Magnetic Resonance*, 232:53–61, 2013.

[61] Milov, A. D. and Salikhov, K. M. and Shchirov, M. D. Application of the double

resonance method to electron spin echo in a study of the spatial distribution of paramagnetic centers in solids. *Soviet Physics Solid State*, 23:975–982, 1981.

[62] A. D. Milov, A. B. Ponomarev, and Yu D. Tsvetkov. electron–electron double resonance in electron spin echo: Model biradical systems and the sensitized photolysis of decalin. *Chemical Physics Letters*, 110:67–72, 1984.

[63] Gunnar Jeschke. DEER Distance Measurements on Proteins. *Annual Review of Physical Chemistry*, 63:419–446, 2012.

[64] Yun Wei Chiang, Peter P. Borbat, and Jack H. Freed. Maximum entropy: A complement to Tikhonov regularization for determination of pair distance distributions by pulsed ESR. *Journal of Magnetic Resonance*, 177:184–196, 2005.

[65] Michael K. Bowman. Visualization of Distance Distribution from Pulsed Double electron–electron Resonance Data. *Applied Magnetic Resonance*, 26:23–39, 2004.

[66] Janin Glaenzer, Martin F. Peter, and Gregor Hagelueken. Studying structure and function of membrane proteins with PELDOR/DEER spectroscopy – A crystallographers' perspective. *Methods*, pages 63–175, 2018.

[67] Wayne L. Hubbell, Hassane S. Mchaourab, Christian Altenbach, and Michael A. Lietzow. Watching proteins move using site-directed spin labeling. *Structure*, 15:779–783, 1996.

[68] Wayne L. Hubbell, Carlos J. Ló, Christian Altenbach, Zhongyu Yang, Wah Chiu, and Gerhard Wagner. Technological advances in site-directed spin labeling of proteins. *Current Opinion in Structural Biology*, 23:725–733, 2013.

[69] Johann P. Klare and Heinz-Jürgen Steinhoff. Spin labeling EPR. *Photosynthesis Research*, 102:377–390, 2009.

[70] V. V. Khramtsov, V. I. Yelinova (Popova), L. M. Weiner, T. A. Berezina, V. V. Martin, and L. B. Volodarsky. Quantitative determination of SH groups in low- and high-molecular-weight compounds by an electron spin resonance method. *Analytical Biochemistry*, 182:58–63, 1989.

[71] Timothy J. Krieger and Henry M. Miziorko. Spinach leaf ribulose-5-phosphate kinase: Examination of sulfhydryls by chemical modification and spin-labeling. *Archives of Biochemistry and Biophysics*, 256:362–371, 1987.

[72] Nolwenn Le Breton, Marlène Martinho, Kuanysh Kabytaev, Jérémie Topin, Elisabetta Mileo, David Blocquel, Johnny Habchi, Sonia Longhi, Antal Rockenbauer, Jérôme Golebiowski, Bruno Guigliarelli, Sylvain R.A. Marque, and Valérie Belle. Diversification of EPR signatures in site directed spin labeling using a β-phosphorylated nitroxide. *Physical Chemistry Chemical Physics*, 16:4202–4209, 2014.

[73] Lawrence J. Berliner and H. Olga Hankovszky. A Novel Reversible Thiol-Specific Spin Label: Papain Active Site Labeling and Inhibition. *Analytical Biochemistry*, 119:450–455, 1982.

[74] Luca Garbuio, Kaspar Zimmermann, Daniel Häussinger, and Maxim Yulikov. Gd(III) complexes for electron–electron dipolar spectroscopy: Effects of deuteration, pH and zero field splitting. *Journal of Magnetic Resonance*, 259:163–173, 2015.

[75] Arina Dalaloyan, Mian Qi, Sharon Ruthstein, Shimon Vega, Adelheid Godt, Akiva Feintuch, and Daniella Goldfarb. Gd(III)–Gd(III) EPR distance measurements – the range of accessible distances and the impact of zero field splitting. *Physical Chemistry Chemical Physics*, 17:18464–18476, 2015.

[76] Shreya Ghosh, Matthew J. Lawless, Gordon S. Rule, and Sunil Saxena. The Cu^{2+}-nitrilotriacetic acid complex improves loading of α-helical double histidine site for precise distance measurements by pulsed ESR. *Journal of Magnetic Resonance*, 286:163–171, 2018.

[77] Yevhen Polyhach, Enrica Bordignon, and Gunnar Jeschke. Rotamer libraries of spin labelled cysteines for protein studies. *Physical Chemistry Chemical Physics*, 13:2356–2366, 2011.

[78] Gregor Hagelueken, Richard Ward, and James H. Naismith. MtsslWizard: In Silico Spin-Labeling and Generation of Distance Distributions in PyMOL. *Applied Magnetic Resonance*, 42:377–391, 2012.

[79] M. M. Hatmal, Yiyu Li, Balachandra G. Hegde, Prabhavati B. Hegde, Christine C. Jao, Ralf Langen, and Ian S. Haworth. Computer Modeling of Nitroxide Spin Labels on Proteins. *Biopolymers*, 97:35–44, 2011.

[80] Katrin Reichel, Lukas S. Stelzl, Jürgen Köfinger, and Gerhard Hummer. Precision DEER Distances from Spin-Label Ensemble Refinement. *The Journal of Physical Chemistry Letters*, 9:17, 2018.

[81] Diego del Alamo, Maxx Tessmer, Richard Stein, Jimmy B. Feix, and Jens Meiler. Protein fold prediction using simulated DEER distance distributions and decay traces. *bioRxiv*, 2019.

[82] Thomas H. Edwards and Stefan Stoll. A Bayesian approach to quantifying uncertainty from experimental noise in DEER spectroscopy. *Journal of Magnetic Resonance*, 270:87–97, 2016.

[83] Thomas H. Edwards and Stefan Stoll. Optimal Tikhonov regularization for DEER spectroscopy. *Journal of Magnetic Resonance*, 288:58–68, 2018.

[84] Luis Fábregas Ibáñez and Gunnar Jeschke. General regularization framework for DEER spectroscopy. *Journal of Magnetic Resonance*, 300:28–40, 2019.

[85] Sarah R. Sweger, Stephan Pribitzer, and Stefan Stoll. Bayesian Probabilistic Analysis of DEER Spectroscopy Data Using Parametric Distance Distribution Models. *The Journal of Physical Chemistry A*, 124:6193–6202, 2020.

[86] Rainer E. Martin, Matthias Pannier, François Diederich, Volker Gramlich, Michael Hubrich, and Hans W. Spiess. Determination of End-to-End Distances in a Series of TEMPO Diradicals of up to 2.8 nm Length with a New Four-Pulse Double Electron Electron Resonance Experiment. *Angewandte Chemie - International Edition*, 37:2833–2837, 1998.

[87] Matthias Pannier, Stephan Veit, Adelheid Godt, Gunnar Jeschke, and Hans W. Spiess. Dead-Time Free Measurement of Dipole–Dipole Interactions between Electron Spins. *Journal of Magnetic Resonance*, 142:331–340, 2000.

[88] Stefan Stoll. Pulse EPR. *eMagRes*, 112:1–46, 2013.

[89] Russell G. Larsen and David J. Singel. Double electron–electron resonance spin–echo modulation: Spectroscopic measurement of electron spin pair separations in orientationally disordered solids. *The Journal of Chemical Physics*, 98:5134–5146, 1993.

[90] G. Jeschke, V. Chechik, P. Ionita, A. Godt, H. Zimmermann, J. Banham, C. R. Timmel, D. Hilger, and H. Jung. DeerAnalysis2006—a comprehensive software package for analyzing pulsed ELDOR data. *Applied Magnetic Resonance*, 30:473–498, 2006.

[91] Sarah R. Sweger, Vasyl P. Denysenkov, Lutz Maibaum, Thomas F. Prisner, and Stefan Stoll. The effect of spin polarization in deer spectroscopy. *In preparation*, 2021.

[92] Kenji Okamoto and Yasushi Sako. Recent advances in FRET for the study of protein interactions and dynamics. *Current Opinion in Structural Biology*, 46:16–23, 2017.

[93] Philipp Honegger and Othmar Steinhauser. The protein–water nuclear Overhauser effect (NOE) as an indirect microscope for molecular surface mapping of interaction patterns. *Physical Chemistry Chemical Physics*, 22:212–222, 2020.

[94] Luis Fábregas Ibáñez, Gunnar Jeschke, and Stefan Stoll. DeerLab: a comprehensive software package for analyzing dipolar electron paramagnetic resonance spectroscopy data. *Magnetic Resonance*, 1:209–224, 2020.

[95] Joseph C. McNulty and Glenn L. Millhauser. TOAC – The Rigid Nitroxide Sidechain. In Lawrence J. Berliner, Sandra S. Eaton, and Gareth R. Eaton, editors, *Biological Magnetic Resonance Volume 19: Distance Measurements in Biological Systems by EPR*, chapter 6, pages 277–307. Springer, Boston, MA, 19 edition, 2002.

[96] M. J. Schmidt, A. Fedoseev, D. Summerer, and M. Drescher. Genetically Encoded Spin Labels for in Vitro and In-Cell EPR Studies of Native Proteins. *Methods in Enzymology*, 563:483–502, 2015.

[97] Theresa Braun, Malte Drescher, and Daniel Summerer. Expanding the Genetic Code for Site-Directed Spin-Labeling. *International Journal of Molecular Sciences*, 20:373, 2018.

[98] Gunnar Jeschke and Yevhen Polyhach. Distance measurements on spin-labelled biomacromolecules by pulsed electron paramagnetic resonance. *Physical Chemistry Chemical Physics*, 9:1895–1910, 2007.

[99] Thomas Schmidt, Rodolfo Ghirlando, James Baber, and G. Marius Clore. Quantitative resolution of monomer-dimer populations by inversion modulated deer epr spectroscopy. *ChemPhysChem*, 17:2987–2991, 2016.

[100] Yevhen Polyhach and Gunnar Jeschke. Prediction of favourable sites for spin labelling of proteins. *Spectroscopy*, 24:651–659, 2010.

[101] Maxx Tessmer, Elizabeth R. Canarie, and Stefan Stoll. Spin label rotamer contributions on the DEER $P(r)$. *In preparation*, 2021.

[102] Shriyaa Mittal and Diwakar Shukla. Predicting Optimal DEER Label Positions to Study Protein Conformational Heterogeneity. *The Journal of Physical Chemistry B*, 121:9761–9770, 2017.

[103] David Kramer. Helium users are at the mercy of suppliers. *Physics Today*, 72:26–29, 2019.

[104] Philipp E. Spindler, Philipp Schöps, Alice M. Bowen, Burkhard Endeward, and Thomas F. Prisner. Shaped pulses in EPR. *eMagRes*, 5:1477–1492, 2016.

[105] Claire L. Motion, Scott L. Cassidy, Paul A.S. Cruickshank, Robert I. Hunter, David R. Bolton, Hassane El Mkami, Sabine Van Doorslaer, Janet E. Lovett, and Graham M. Smith. The use of composite pulses for improving DEER signal at 94 GHz. *Journal of Magnetic Resonance*, 278:122–133, 2017.

[106] Markus Teucher and Enrica Bordignon. Improved signal fidelity in 4-pulse DEER with Gaussian pulses. *Journal of Magnetic Resonance*, 296:103–111, 2018.

[107] Jue Chen, Susan Sharma, Florante A. Quiocho, and Amy L. Davidson. Trapping the transition state of an ATP-binding cassette transporter: Evidence for a concerted mechanism of maltose transport. *Proceedings of the National Academy of Sciences*, 98:1525–1530, 2001.

[108] J. C. Spurlino, G. Y. Lu, and F. A. Quiocho. The 2.3 Å resolution structure of the maltose- or maltodextrin-binding protein, a primary receptor of bacterial active transport and chemotaxis. *Journal of Biological Chemistry*, 266:5202–5219, 1991.

[109] Andrew J. Sharff, Lynn E. Rodseth, John C. Spurlino, and Florante A. Quiocho. Crystallographic Evidence of a Large Ligand-Induced Hinge-Twist Motion between

the Two Domains of the Maltodextrin Binding Protein Involved in Active Transport. *Biochemistry*, 31:10657–10663, 1992.

[110] Florante A. Quiocho, W. E. Meador, and J. W. Pflugrath. Preliminary Crystallographic Data of Receptors for Transport and Chemotaxis in Escherichia coli: D-Galactose and Maltose-binding Proteins. *Journal of Molecular Biology*, 133:181–184, 1979.

[111] Jason A. Hall, Thorgeir E. Thorgeirsson, Jun Liu, Yeon-Kyun Shin, and Hiroshi Nikaido. Two Modes of Ligand Binding in Maltose-binding Protein of Escherichia coli - Electron Paramagnetic Resonance Study of Ligand-Induced Global Conformational Changes by Site-Directed Spin Labeling. *Journal of Biological Chemistry*, 272:17610–17614, 1997.

[112] Jason A. Hall, Kalle Gehring, and Hiroshi Nikaido. Two Modes of Ligand Binding in Maltose-binding Protein of Escherichia coli Correlation with the Structure of Ligands and the Structure of Binding Protein. *Journal of Biological Chemistry*, 272:17605–17609, 1997.

[113] Jason A. Hall, Anand K. Ganesan, James Chen, and Hiroshi Nikaido. Two Modes of Ligand Binding in Maltose-binding Protein of Escherichia coli: Functional Significance in Active Transport. *Journal of Biological Chemistry*, 272:17615–17622, 1997.

[114] Kalle Gehring, Philip G. Williams, Jeffrey G. Pelton, Hiromi Morimoto, and David E. Wemmer. Tritium NMR Spectroscopy of Ligand Binding to Maltose-Binding Protein. *Biochemistry*, 30:5524–5531, 1991.

[115] Kevin H. Gardner, Xiaochen Zhang, Kalle Gehring, and Lewis E. Kay. Solution NMR Studies of a 42 KDa Escherichia Coli Maltose Binding Protein/-Cyclodextrin Complex: Chemical Shift Assignments and Analysis. *Journal of the American Chemical Society*, 120:11738–11748, 1998.

[116] M. R. Fleissner, M. D. Bridges, E. K. Brooks, D. Cascio, T. Kalai, K. Hideg, and W. L. Hubbell. Structure and dynamics of a conformationally constrained nitroxide side chain and applications in EPR spectroscopy. *Proceedings of the National Academy of Sciences*, 108:16241–16246, 2011.

[117] Huanting Liu and James H. Naismith. An efficient one-step site-directed deletion, insertion, single and multiple-site plasmid mutagenesis protocol. *BMC Biotechnology*, 8:91–101, 2008.

[118] Anne Spriestersbach, Jan Kubicek, Frank Schäfer, Helena Block, and Barbara Maertens. Purification of His-Tagged Proteins. *Methods in Enzymology*, 559:1–15, 2015.

[119] Aidin R. Balo, Hannes Feyrer, and Oliver P. Ernst. Toward Precise Interpretation of

DEER-Based Distance Distributions: Insights from Structural Characterization of V1 Spin-Labeled Side Chains. *Biochemistry*, 55:5256–5263, 2016.

[120] Hui Wang, Hui Shi, Malini Rajan, Elizabeth R. Canarie, Seoyeon Hong, Daniele Simoneschi, Michele Pagano, Matthew F. Bush, Stefan Stoll, Elizabeth A. Leibold, and Ning Zheng. FBXL5 Regulates IRP2 Stability in Iron Homeostasis via an Oxygen-Responsive [2Fe2S] Cluster Article FBXL5 Regulates IRP2 Stability in Iron Homeostasis via an Oxygen-Responsive [2Fe2S] Cluster. *Molecular Cell*, 78:31–41, 2020.

[121] Tracey A. Rouault. Iron-sulfur proteins hiding in plain sight. *Nature Chemical Biology*, 11:442–445, 2015.

[122] Lukas C. Kühn. Iron regulatory proteins and their role in controlling iron metabolism. *Metallomics*, 7:232–243, 2015.

[123] Tracey A. Rouault. The role of iron regulatory proteins in mammalian iron homeostasis and disease. *Nature Chemical Biology*, 2:406–414, 2006.

[124] Cole P. Anderson, Macy Shen, Richard S. Eisenstein, and Elizabeth A. Leibold. Mammalian iron metabolism and its control by iron regulatory proteins. *Biochimica et Biophysica Acta - Molecular Cell Research*, 1823:1468–1483, 2012.

[125] M. Claire Kennedy, William E. Antholine, and Helmut Beinert. An EPR Investigation of the Products of the Reaction of Cytosolic and Mitochondrial Aconitases with Nitric Oxide. *The Journal of Biological Chemistry*, 272:20340–20347, 1997.

[126] David J. Haile, Tracey A. Rouault, Joe B. Harford, Mary Claire Kennedy, George A. Blondin, Helmut Beinert, and Richard D. Klausner. Cellular regulation of the iron-responsive element binding protein: Disassembly of the cubane iron-sulfur cluster results in high-affinity RNA binding. *Biochemistry*, 89:11735–11739, 1992.

[127] B. Guo, J. D. Phillips, Y. Yu, and E. A. Leibold. Iron regulates the intracellular degradation of iron regulatory protein 2 by the proteasome. *Journal of Biological Chemistry*, 270:21645–21651, 1995.

[128] Eric S. Hanson, Laura M. Foot, and Elizabeth A. Leibold. Hypoxia post-translationally activates iron-regulatory protein 2. *Journal of Biological Chemistry*, 274:5047–5052, 1999.

[129] Ajay A. Vashisht, Kimberly B. Zumbrennen, Xinhua Huang, David N. Powers, Armando Durazo, Dahui Sun, Nimesh Bhaskaran, Anja Persson, Mathias Uhlen, Olle Sangfelt, Charles Spruck, Elizabeth A. Leibold, and James A. Wohlschlegel. Control of Iron Homeostasis by an Iron-Regulated Ubiquitin Ligase. *Science*, 326:718–721, 2009.

[130] Ameen A. Salahudeen, Joel W. Thompson, Julio C. Ruiz, He-Wen Ma, Lisa N. Kinch, Qiming Li, Nick V. Grishin, and Richard K. Bruick. An E3 Ligase Possessing an

Iron-Responsive Hemerythrin Domain Is a Regulator of Iron Homeostasis. *Science*, 326:722–726, 2009.

[131] Chang Shu, Min Woo Sung, Mikaela D. Stewart, Tatyana I. Igumenova, Xiangshi Tan, and Pingwei Li. The Structural Basis of Iron Sensing by the Human F-box Protein FBXL5. *ChemBioChem*, 13:788–791, 2012.

[132] Julio C. Ruiz. *FBXL5 is Required for the Mantainance of Cellular and Systemic Iron Homeostasis*. PhD thesis, University of Texas Southwestern Medical Center, 2012.

[133] Sven Andreas Freibert, Benjamin D. Weiler, Eckhard Bill, Antonio J. Pierik, Ulrich Mühlenhoff, and Roland Lill. Biochemical Reconstitution and Spectroscopic Analysis of Iron-Sulfur Proteins. *Methods in Enzymology*, pages 197–226, 2018.

[134] Stefan Stoll and Arthur Schweiger. EasySpin, a comprehensive software package for spectral simulation and analysis in EPR. *Journal of Magnetic Resonance*, 178:42–55, 2006.

[135] Helmut Beinert, Richard H. Holm, and Eckard Münck. Iron-Sulfur Clusters: Nature's Modular, Multipurpose Structures. *Science*, 277(5326):653–659, 1997.

[136] Frank Neese, Frank Wennmohs, Ute Becker, and Christoph Riplinger. The ORCA quantum chemistry program package. *Journal of Chemical Physics*, 152:224108, 2020.